INVESTIGATION OF DATA QUALITY FOR WIND TUNNEL INTERNAL BALANCE TESTING

A Thesis

by

JOHN PRESTON HIDORE

Submitted to the Office of Graduate Studies of
Texas A&M University
in partial fulfillment of the requirements for the degree of

MASTER OF SCIENCE

Approved by:

Chair of Committee,	Edward White
Committee Members,	Othon Rediniotis
	Bryan Rasmussen
Head of Department,	Rodney Bowersox

May 2013

Major Subject: Aerospace Engineering

ABSTRACT

Achieving high quality, consistency, and testing efficiency in wind tunnel tests using internal balances is accomplished through the use of new testing methods, analysis of data output, and standardized documentation of test procedures at the Texas A&M Low Speed Wind Tunnel. The wind tunnel is capable of performing internal balance testing on models that experience less than 500 pounds of normal force. Testing has shown less than a 3% mean flow variation with the sting mount installed and a turbulence intensity of less than 0.25%. Documentation of procedures and checklists for installation of internal balance testing equipment and test execution provide higher efficiency and consistency during a test. A step-by-step examination of the data analysis routines and associated uncertainty equations show uncertainty in the force and moment coefficients for the Mark XIII internal balance to be approximately ± 0.05 and ± 0.02, respectively. Quantifying the uncertainty of the primary output parameters and showing repeatability of the data within the defined uncertainty limits achieved higher quality results.

For my wonderful parents, the family, and my lovely wife.

ACKNOWLEDGEMENTS

I would first and foremost like to thank my advisor, Dr. White. His teaching, reassurance, and guidance throughout the past few years are what have made this thesis possible. Also, thank you to my committee members, Dr. Rediniotis and Dr. Rasmussen, for their assistance in piecing this work together. A special thank you to the staff of the Texas A&M Oran W. Nicks Low Speed Wind Tunnel. Their patience and support have been limitless and valuable during this process. Thank you to fellow student workers Doug Kutz and Tanner Black for their dedicated help in conducting this research, even through the difficult times. Lastly, thank you to my family and my beautiful wife who have provided the endless encouragement and prayers that made this work a reality.

TABLE OF CONTENTS

Page

LIST OF FIGURES

LIST OF TABLES

CHAPTER I

INTRODUCTION TO WIND TUNNEL TESTING

Many capability enhancements have been recently instituted at the Texas A&M Low-Speed Wind Tunnel (LSWT). Thus, it is essential to develop and execute different routines that will fully utilize the new capabilities of the facility. If there is an understanding of how to properly use these assets, these updates will help tunnel operations become more efficient and improve the quality of the data output.

Wind tunnel operations provide a variety of unique challenges that must be addressed to complete a test. Tests utilizing an internal balance are frequently performed at the LSWT and many of these have a number of underlying similarities. Therefore, it is vital to create standardized procedures that reduce testing error and produce documentation of an internal balance test at the LSWT. A standardized checklist of the common and critical tasks would improve the setup and execution of a test. Standardizing the test procedures, increasing efficiency, and reducing error through new testing methods for a single internal balance test will cascade to the numerous similar tests performed at the LSWT.

The goal in performing any wind tunnel test is to efficiently achieve high quality data. A systematic, documented testing procedure will increase the comprehension of the accuracy and limitations of the data collected during a test. Once this is complete, a thorough uncertainty analysis can be performed that takes into account both data acquisition and data analysis. This will help the LSWT staff provide improved support to users in understanding how to properly interpret data and how to potentially design a test to obtain more relevant results in the future.

New facility management has introduced many changes in the daily operations

of the LSWT facilities. Documentation of an internal balance test will encourage better communication between test designers, operators, and managers about how a test is executed and the best way to approach typical concerns. With a smaller full-time workforce, recording the procedures of an internal balance test has become key. This documentation would furnish students and other employees with a guideline to reference during an internal balance test.

The goal of this thesis is to provide: improved efficiency and consistency in internal balance setup and testing, a record of data uncertainty and limitations, and higher quality results. The objectives for higher quality data are quantification of the uncertainty for all primary output variables and repeatability of data within the defined uncertainty limits. This will be attained through the use of new testing methods, analysis of data output, and standardized documentation of test procedures for an internal balance test at the Texas A&M Low-Speed Wind Tunnel.

The first task is to produce standardized documentation for an internal balance test at the LSWT. This is accomplished by recording all pertinent information about the tunnel facilities and equipment. In order to properly design a test, it is crucial to understand and document the capabilities and limitations of the internal balance and the HARS mount system as well as the test section flow uniformity and turbulence intensity.

The second task is to become more accurate and efficient in running internal balance tests. Establishing a checklist or guideline that clearly explains how to properly perform a test at the LSWT can complete this task. This documentation should include a clear task list with acceptable outcomes to each task before moving on to the next step. New testing methods that increase efficiency and output quality should be defined in this documentation. The objectives for new testing methods are to decrease set-up time by one hour and the uncertainty of pre-testing measurements.

The third task is to fully reduce the tunnel output data and perform an uncertainty analysis on the reduction routine. This implies a need for data reduction procedures that include a listing of reduction methods with key equations. Also, to better understand the data, a step-by-step uncertainty analysis should be included to define where improvements might be made to obtain more accurate results during a test. Once these areas are identified, the improvements can be implemented in order to increase efficiency and quality.

The first topic to be covered in Chapter II is the history and facility specifications of the LSWT. This chapter includes information regarding the wind tunnel layout, test section dimensions, and specifications of the internal balances and other testing equipment. Chapter III reports recent testing performed at the LSWT to define the flow uniformity and turbulence intensity in the test section. This includes information regarding the testing procedure as well as the results. Chapter IV is a record of documentation and standardized testing practices at the LSWT. This chapter details the testing procedure and references the checklists in Appendix E. Chapter V describes the data analysis routines and the associated uncertainty analysis. Data from a recent test at the LSWT is used to determine the uncertainty introduced at each step in the data analysis process. Finally, Chapter VI sums up the scope and goal of this work and draws relevant conclusions from the results of the previous chapters.

CHAPTER II

LOW SPEED WIND TUNNEL FACILITY DETAILS

A. History of the Oran W. Nicks Low Speed Wind Tunnel

The history of the Texas A&M Low Speed Wind Tunnel (LSWT) began when Gibb Gilchrist was hired as the dean of the Texas AMC School of Engineering in 1937. He had a vision for a flight training school and associated facilities located at Texas A&M University. These ideas led to the establishment of the Department of Aerospace Engineering, which opened as the second largest department of its kind in the nation in September of 1940 [1]. The establishment of the department was followed by the construction of Easterwood Airport, two miles west of campus [2].

The idea for the Texas A&M LSWT was first conceived in June of 1940. Gilchrist submitted the original proposal for the wind tunnel in May of 1941, and estimated the cost to be $80,000. However, he was awarded the office of college president in May of 1944 [3], two months before official approval to construct the wind tunnel was granted. The construction process began shortly thereafter under the guidance of the new Aerospace Department Head, Robert Pinkerton, but was not completed in its current form until 1958. The final construction cost of the LSWT was a little over $200,000, with $90,000 of that cost contributed by Texas Engineering & Manufacturing Company (TEMCO Aircraft).

The first trial run of the LSWT was performed on November 21, 1958. Under the supervision of the original director, Mr. Frederick Hall, preliminary testing of the facility was completed and the first test was conducted for TEMCO on May 3, 1960. In April of 2000, the facility was renamed the Texas A&M Oran W. Nicks Low

Speed Wind Tunnel, after the former wind tunnel director and renowned aerospace pioneer. Nicks was an avid aviator who first piloted an aircraft in 1941. He served as program-center director at NASA for 20 years, where he was responsible for more than 30 missions to the moon and Mars. After, Nicks was hired by Texas A&M University in 1980 as a research engineer and director of the LSWT. He would spend the next 16 years leading the wind tunnel facilities and directing advanced research at Texas A&M [4]. Oran Nicks' was responsible for turning the Texas A&M LSWT into one of the leading research facilities of its kind in the nation.

Since opening in 1960, the LSWT has been committed to the advancement of air and space technology. Research has been conducted at the LSWT on everything from bicycles, golf clubs, and light pole fixtures, to missiles, airplanes, and space re-entry vehicles. The LSWT has performed tests for companies such as Cessna, Bell Helicopter, and the National Aeronautics and Space Administration (NASA). One notable recent test occurred while aiding NASA with an emergency project for the shuttle Atlantis. During STS-117 in 2006, testing had to be performed at the LSWT to verify that a repair made to the thermal blanket, which was damaged during launch, would survive re-entry.

B. General Facility Specifications

The Texas A&M Oran W. Nicks Low Speed Wind Tunnel is a large-scale, closed-circuit wind tunnel located at Easterwood Airport in College Station, Texas. A schematic of the facility can be seen in Figure 4. The circuit length at the centerline is 398 feet. The cross section is circular from the fan to the entrance of the contraction section with a maximum diameter of 30 feet occurring in the settling chamber. Each turn in the circuit contains a set of turning vanes to help guide the flow. A double

screen is located between the settling chamber and contraction section to minimize turbulence and provide uniform flow into the test section. A 30-foot long contraction segment then changes the cross section from circular to rectangular with a 10.4 contraction ratio.

The rectangular test section is 7 feet tall, 10 feet wide, and 12 feet in length. The test section contains one-foot chamfers in all four corners which reduce the overall cross sectional area to 68 square feet. The walls diverge two inches in the horizontal direction over the length of the test section to account for boundary layer growth and minimize stream-wise buoyancy. Two vertical vent slots allow the tunnel to maintain a static pressure in the test section near ambient. These vents mark the end of the test section.

A 46-foot-long diffuser, located downstream of the test section, changes the cross sectional shape from rectangular, back to circular at the fan. The horizontal and vertical angles of the diffuser are 1.43 and 3.38 degrees, respectively. The fan is a Curtiss Electric four-blade, B-29 propeller with a diameter of 12.5 feet. Each blade is cut 18 inches from the tip in order to properly fit them to the diameter of the tunnel. The blade tips are inset into the tunnel wall to minimize tip effects. A 24-volt direct current motor and planetary gear system, housed in the propeller assembly, allow for the variable pitch capabilities.

The motor is a 3,000 horsepower, induction motor that was recently built by TECO-Westinghouse and installed at the LSWT in May of 2012. The induction motor combined with a variable frequency drive allows for adjustable revolutions per minute (RPM) capabilities. The maximum setting is 1,200 RPM. However, the motor can force the tunnel to reach the current top allowable wind speed of 200 miles per hour (MPH) at 60 percent of this power, 720 RPM.

The test section can be outfitted with a three axis traversing mechanism. This

can be used to position hotwires or pressure probes with repeatability accuracy of 0.01 inches. The traverse moves in the plane normal to the flow, while the probes are mounted to an extension arm that is set manually.

C. Tunnel Operation

The tunnel is controlled using the calculated dynamic pressure of the airflow at the center of the test section. Two static pressure rings, consisting of four ports each, are used to measure the average static pressure in the tunnel at the end of the settling chamber and five feet in front of the test section. The difference of these static pressure measurements is a pseudo dynamic pressure called q_{set}. The measurement of q_{set} is used to calibrate the actual dynamic pressure in the center of the empty test section, q_a, with the use of a Pitot tube. A calibration curve is created and used to calculate q_a from q_{set} when the Pitot tube is not installed in the test section. While the tunnel is in operation, q_{set} is constantly measured and used to calculate q_a.

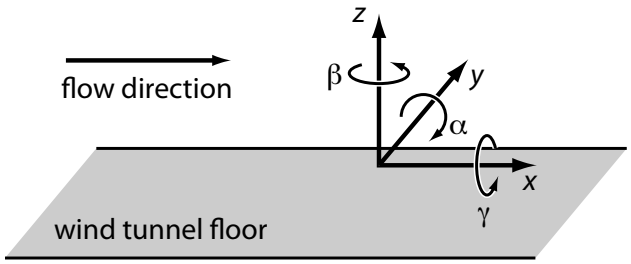

Fig. 1: External balance measurement coordinate system.

The temperature inside the tunnel is measured with a thermocouple that is located on the wall at the beginning of the test section. The barometric pressure is recorded in the balance room, beneath the test section. These measurements allow the velocity in the test section, based on tunnel conditions, to be calculated in real-

time. The total and static pressure in the tunnel are also measured during a test, with use with a Pitot tube located on the far wall.

The LSWT is equipped with a six component, pyramidal electromechanical, external balance system located beneath the test section. The external balance measures three force components and three moments in a wind-oriented coordinate system shown in Figure 1.

Table 1: External Balance Force and Moment Limitations

Load	Minimum	Maximum
Lift	-1000 lbf	+3000 lbf
Drag/Side	-1000 lbf	+1000 lbf
Pitch/Roll	-2000 ft-lbf	+2000 ft-lbf
Yaw	-1000 ft-lbf	+1000 ft-lbf

The origin of the coordinate system is the geometric center of the test section, 42 inches above the floor. The measurements are sent to the data acquisition system using optical encoders. The force and moment limits of the external balance are listed in Table 1. The external balance is isolated from the upper turntable. The turntable can rotate to any position within -120 to +190 degrees.

D. Data Acquisition Capabilities

The LSWT is equipped to read pressure data with a Measurement Specialties System 8400. The system can read up to 16 64-port pressure scanners. The facility is currently outfitted with 10 inH_20 and 20 inH_20 scanners, as well as one-psi and five-psi scanners. One 10 inH_20 and one 1-psi scanner are equipped with digital temperature correction (DTC) capabilities. The current LSWT scanner inventory is

given in Table 2. The System 8400 is capable of scanning the pressure measurements at a maximum 40 Hz. Standard procedure is to recalibrate the scanners, via the on board calibration unit, every two hours.

Table 2: Pressure Scanner Capabilities

Unit	Ports	Range	DTC	Quantity
Scanner 1	32	10 inH_2O	No	1
Scanner 2	32	10 inH_2O	Yes	1
Scanner 3	32	20 inH_2O	No	1
Scanner 4	32	1 psi	No	2
Scanner 5	32	1 psi	Yes	1
Scanner 6	32	5 psi	No	4

The data acquisition system is housed within the Signal Conditioning Extensible Interface (SCXI) unit built by National Instruments. SCXI contains an internal multiplexer that is connected to an M-series PCI 6289, 18-bit analog to digital board with signal conditioning capabilities. The unit has a maximum aggregate sampling rate of 300 kHz. The SCXI unit can be used in conjunction with up to 24 different voltage channels at one time. Examples of devices commonly used in conjunction with SCXI include hotwires, strain gauges, thermocouples, and internal balances.

E. Internal Balance Testing Equipment

This thesis focuses on investigating the data quality for internal balance testing. Therefore, this section contains more detail than the previous sections in order to properly introduce internal balance testing procedures. The LSWT owns three internal balances: the Mark X, Mark XIII, and 7-11A.

The 7-11A is slightly larger than the other two balances. Since it is a three force

and three moment balance, it directly measures all of the loads on the model. This balance was last calibrated in 1998. It differs from the Mark XIII internal balance by allowing a significantly larger maximum axial force and pitching moment.

The Mark X has lower maximum allowable loads than the Mark XIII, which is shown in Figure 5. The exact values of maximum allowable loading for all gages are displayed in Table 3. Both of these balances are five force and one moment internal balances. The gages are set up to measure two normal force loads, two side force loads, an axial force load, and a rolling moment. Subsequently, the pitching moment and yawing moment can be calculated from the respective forces and known distance between the gages. It is important to note that the factor of safety for these internal balances is small, approximately 1.25. Due to this, it is imperative to not overload the balance or one of the internal gages will likely fail.

Table 3: Internal Balance Force and Moment Limitations

Load Type	Symbol	Mark X	Mark XIII	7-11A
Normal Force Forward	$N1$	100 lbf	500 lbf	500 lbf
Normal Force Aft	$N2$	100 lbf	500 lbf	NA
Side Force Forward	$S1$	50 lbf	500 lbf	350 lbf
Side Force Aft	$S2$	50 lbf	500 lbf	NA
Rolling Moment	RM	120 in-lbf	800 in-lbf	720 in-lbf
Axial Force	AX	60 lbf	150 lbf	500 lbf
Pitching Moment	PM	425 in-lbf	2625 in-lbf	4200 in-lbf
Yawing Moment	YM	262 in-lbf	2125 in-lbf	2100 in-lbf

Force Measurement Systems last calibrated the Mark X and Mark XIII internal balances in 2008. The calibration results in a standard [5] 6 x 96 matrix that is used to iterate and calculate the force on the balance from the voltage output of the strain

gages. The calibration method and accuracy will be discussed in detail in Chapter V.

Both balances are attached to the end of a sting using a simple taper and setscrew mechanism. In order to mount a model to the balance, a balance block must be designed and machined. This piece will securely attach the internal balance to a structurally sound location inside the model. The key dimensions of both balances are listed in Table 4.

Table 4: Important Internal Balance Dimensions

Dimension	Symbol	Mark X	Mark XIII	7-11A
Outer Diameter	$\varnothing_o$	1.250 in	1.250 in	1.750 in
Total Length	L_o	8.250 in	8.250 in	8.700 in
Aft Face to BMC	x_a	3.025 in	3.025 in	0.900 in
NF1 to BMC	x_1	2.125 in	2.625 in	NA
NF2 to BMC	x_2	2.125 in	2.625 in	NA
SF1 to BMC	x_3	2.625 in	2.125 in	NA
SF2 to BMC	x_4	2.625 in	2.125 in	NA

For internal balance tests, the LSWT is equipped with a High Attitude Robotic Sting (HARS) mount system, seen in Figure 6. The internal balance is installed on the end of the sting and a model is built around the balance. The HARS system provides pitch control of the model while keeping the model in the center of the test section. Depending on the model, the system can be moved to a maximum yaw angle of approximately 45 degrees using the turntable.

The HARS system is comprised of four main parts: the front and rear struts, bullet, and sting. Two separate pivot blocks can be used to attach the front strut to the bullet. The normal block is a straight attachment between the front strut and the forward most pivot pin location on the bullet. This block allows the HARS unit

to pitch between -15 and +66 degrees. The second block, or "90° block", attaches the front strut to the rear pin on the bullet in a curved manner. This block allows the HARS system to pitch between 0 and 105 degrees.

The front and rear strut simultaneously telescope to reach the desired pitch angle while maintaining the model close to the vertical center of the tunnel. At the center of each strut is a 1.5-5 ACME screw, driven by a Baldor motor. The motor is connected to a Carson Manufacturing gearbox that provides a 22:1 torque multiplication ratio. The gear system between the gearbox and ACME screw is simply a 1:1 torque multiplication ratio.

The telescoping piece of each strut is bolted to the ACME screw through a 1.5-5 ACME nut. Four longitudinal keys that are attached to the inner strut lock the ACME nut. The telescoping struts move in a bronze keyway that is attached to the outer casing of each strut. The front and rear struts are each connected to the bullet with a one inch, 17-4 stainless steel pin that is kept in place by end caps and set screws. The pins rotate in bronze bushings. This degree of freedom allows the system to pitch. The bullet houses the roll motor, as well as the associated gearbox and cooling fan. The shaft from the roll motor rotates in internal bearings. The bullet cover also contains one, 32-port pressure scanner for use with sting-mounted models.

The sting is attached to the bullet with a wedge system. The sting is inserted into a large screw that at attached to two cylindrical blocks. This is then screwed onto the front of the bullet while the blocks wedge into the slight taper inside the bullet, thus clamping the sting into place. The internal balance mounts to the end of the sting using setscrews to wedge the balance into a taper in the sting.

CHAPTER III

LOW SPEED WIND TUNNEL FLOW CHARACTERIZATION

A. Introduction and Experimental Setup

To ensure data accuracy, it is important to regularly define the flow quality inside the wind tunnel test section. Flow quality is measured by flow uniformity, flow angularity, and turbulence intensity. This thesis will focus on flow uniformity and turbulence intensity, but will not address flow angularity in this chapter. The effective flow angularity will be addressed in Chapter V when correcting for an internal balance test. The objective was to show uniformity of the airflow throughout the geometric plane in which testing occurs. At times, the results of the testing will reveal imperfections in the flow that can be improved by repairing or adjusting different components of the wind tunnel.

The three goals for the flow uniformity testing were to document the results in the testing plane with HARS installed in the test section as well as with an empty test section at normal and low dynamic pressure values. Other measurements of interest were the turbulence intensity, motor performance, and associated tunnel limitations.

To collect the proper measurements, both a Pitot tube and a hotwire were employed during the experiment. The traversing mechanism was installed in the test section downstream of the mid-plane. An extension arm was then connected as shown in Figure 11. The two probes were mounted side by side, 4 inches apart at the end of the extension. The hotwire was on the right when looking downstream and oriented such that the wire was parallel to the floor of the test section, as shown in Figure 12.

The tunnel coordinate system used in these experiments is a right-handed system

that defines the x and z-axes as positive downstream and up, respectively. The origin of this coordinate system is located in the geometric center of the test section. The two probes were installed at a fixed position, 69 inches downstream of the beginning of the test section, x equal to -3 inches. The in-plane location of the measurements was determined by zeroing the Pitot tube at the origin of the coordinate system. The location of the middle of the test section is measured as 42 inches from the floor and 60.75 inches from each wall. The 60.75 inch location is the center of the testing plane in the y-direction due to the angularity of the walls to account for boundary layer growth. The traversing mechanism allowed the probes to move from -32 inches to +36 inches along the y-axis and -16 inches to +24 inches along the z-axis. A thermocouple located along the near wall was used to measure the test section temperature, as shown in Figure 13.

When HARS was installed in the tunnel, the setup of the probes was not altered. A 37-inch sting was attached to the HARS mount system. An aluminum piece was then fit into the end of the sting in order to prevent flow from entering the sting as shown in Figure 14. Aluminum tape was used to cover any remaining holes in the sting and HARS mount to ensure smooth flow around the system.

B. Probe Calibration and Data Analysis Method

The Pitot tube was calibrated using the System 8400 on-board unit every two hours throughout the day. Since the temperature could fluctuate as much as 30° F during a test day, a temperature compensating calibration was employed for the hotwire. In order to accomplish this, three calibration runs were performed at different times during the day. These were completed at the beginning of the day while the test section was still cool, in the middle of the day, and at the end of the day when

the test section was at its peak temperature.

The process of calibrating the constant temperature hotwire anemometer began with recording the hotwire voltage, tunnel velocity, and temperature at the center of the test section. This was completed for a range of velocities at a hot and cold temperature value. The hotwire voltage was plotted against the velocity calculated from the Pitot tube at both the hot and cold calibration temperatures as shown in Figure 17. The heat-transfer relationship shown in Equation 3.1, King's Law, was used to fit the data. This curve fit provides values for the initial coefficients A_{oi} and B_{oi} for both sets of data.

$$U_i(E_i) = \left(A_{oi} + B_{oi} \cdot {E_i}^2\right)^2 \tag{3.1}$$

The data must be adjusted since the velocities at which the cold and hot calibration data points were collected do not match. This is accomplished using a first order Taylor series to correct the cold hotwire voltages to the hot Pitot tube velocities as shown in Equation 3.2. The derivative of the cold hotwire voltage with respect to the cold velocity measurements is approximated using backward differencing.

$$E_{ci} = E_{ci} + \left.\frac{\partial E_c}{\partial U_c}\right|_i (U_{hi} - U_{ci}) \tag{3.2}$$

In order to correct for temperature drift, a temperature compensation-coefficient can be created to adjust the hotwire voltage to a defined standard temperature. This concept is thoroughly explored in a doctoral dissertation by White [6]. The temperature compensation-coefficient is calculated using:

$$C_t(U) = \frac{{E_h}^2 - {E_c}^2}{T_h - T_c} \tag{3.3}$$

After, the temperature-compensation coefficient is fit with Equation 3.4 to determine the coefficients C_o and D_o as seen in Figure 18. The temperature-compensation

coefficient is a function of the test-section velocity, which is generally the unknown value. During calibration, the Pitot tube allows for the direct calculation of the temperature-compensation coefficient. However, during a data collection run, calculating the velocity from the hotwire voltage will involve an iterative process to determine the temperature-compensation coefficient. The fit of the compensation coefficient allows for its calculation at a wide range of velocities.

$$C_t(U) = -C_o - D_o \cdot U^{\frac{1}{2}} \tag{3.4}$$

To complete the calibration, the cold and hot voltage values are processed using Equation 3.5. The value for the compensated temperature (T_{comp}) should be chosen to be in the range of the hot and cold calibration temperatures.

$$\left(E_i\right)_{new}{}^2 = {E_i}^2 + C_t(U)\left(T_{comp} - T\right) \tag{3.5}$$

Next, the data is again fit with King's Law to determine the compensated coefficients A_c, B_c, and n_c as shown in Equation 3.6. The sample result for this test is shown in Figure 19. The coefficients are used in conjunction with an iterative method for solving the temperature-compensation coefficient to determine the velocity from the hotwire voltage.

$$U(E) = \left(A_c + B_c \cdot E^2\right)^{n_c} \tag{3.6}$$

Once the calibration is finished, the flow uniformity runs can be completed. The voltage read by the hotwire at each data point can be turned into a velocity using an iterative method for temperature compensation. With the use of the Newton-Raphson method, convergence is usually achieved within five to ten iterations. It is good practice to run the calibration data through the iterative method code to check the output. As shown in Figure 20, the hot and cold calibration data should align.

The flow uniformity runs were conducted at multiple test section dynamic pressures associated with various motor RPM values. The dynamic pressure from the

Pitot tube attached to the traversing mechanism divided by its mean value over the flow field provided a unit-less measure for each data point. These measurements for each data point represent a percent deviation from the mean and are calculated using:

$$q_{dev.}[\%] = \left[\left(\frac{q_i}{q_{mean}}\right) - 1\right] \cdot 100 \tag{3.7}$$

Theoretically, this value would be zero for completely uniform flow. This equation yields a non-dimensional measure of the flow uniformity as a percent deviation from the spatial mean. In order to be certain that the mean test section velocity was close to the supposed value, the tunnel was re-calibrated as described later in this chapter.

C. Flow Uniformity

The first goal of the testing was to characterize the uniformity of the flow around the HARS mount. The baseline case considered in this section was with HARS located at an alpha and beta value of 0° and a test section dynamic pressure of 50 psf. This condition corresponds to Run 8 as seen in Figure 23. Measurements of the dynamic pressure were taken in 6 inch increments for y-values ranging from -32 to +36 inches and -16 to 24 inches in the z-direction. The corners of the plots in Appendix C are blocked out in gray to represent the 1-foot by 1-foot chamfers in each corner of the test section.

The percent deviation of the dynamic pressure from the mean flow in Figure 23 exhibits a discernable pattern around the HARS mount. The plot shows a 1% to 3% drop in the dynamic pressure directly around the HARS mount. This drop increases in severity closer to the floor and diminishes moving away from HARS in the y-direction. Due to the off-center location of the Pitot Tube in relation to the extension arm, the measurements around HARS are non-symmetric. The flow decrease is also non-symmetric with a slightly larger decrease in the negative y-direction. An increase

of 1% to 2% in the dynamic pressure away from the HARS mount in the top corners of the data field can be seen in Figure 23.

The data points taken around the origin are within 1 to 3 inches of the end of the sting. Figure 23 displays that the flow directly around the end of the sting is within 1% of the mean dynamic pressure.

Figures 21, 22, and 24 show a comparison of the flow uniformity for the HARS mount at 0° alpha and beta at different dynamic pressures. The same flow pattern that is described in the previous paragraphs holds true at the different dynamic pressures. The flow uniformity is consistently unchanging across a wide range of dynamic pressures.

Figures 21 through 24 can be compared to Figures 25 through 28 to see the consquence of running the motor at different RPM values on the flow uniformity. The motor RPM has little effect on the flow uniformity, especially at the higher dynamic pressures. There is a noticeable improvement in the flow uniformity at the lower dynamic pressures when the motor RPM is significantly increased. Figures 21 and 25 show runs at 5 psf with corresponding motor RPM values of 240 and 600. In Figure 25 the deviation from the mean flow in the top corners of the measurement field is closer to zero than in Figure 21. However, the flow field near the origin, where the model would be mounted, is almost identical in both cases.

Figures 29 through 62 contain the rest of the flow uniformity data with HARS installed in the test section. Figure 62 displays a repeat run that corresponds to Figure 23. This run was performed on a separate day from the initial run and proves that the data were repeatable. Figure 61 shows an identical run to Figure 23, except that the traversing mechanism was moved so that measurements were recorded in the reverse order. The temperature change during a single run did not affect the outcome of the data as exhibited in these figures.

When the HARS unit was moved in beta as shown in Figures 39 and 43, the flow uniformity began to degrade throughout the test section. The dynamic pressure deviation shows a pressure drop toward the side of the test section which HARS rotates into and a pressure increase on the opposite side. The pressure deviation is acceptable around the origin, but quickly worsens in both directions along the y-axis. Figure 41 contains the data with HARS located at 0° in alpha and 30° in beta at a dynamic pressure of 5 psf. This plot showcases the worst instance of flow uniformity with HARS installed in the test section.

The flow uniformity was significantly better when the HARS mount was moved in alpha as shown in Figures 31 and 35. The dynamic pressure decrease directly around the HARS mount became less drastic at higher angles of attack. At the same time, the pressure increase at the edges of the measurement field dwindled to produce a more uniform flow field near the center of the test section.

Finally, moving the HARS mount in alpha while at a designated value of beta consistently improved the flow uniformity. Figures 43 and 59 display the results with HARS at 30° in beta, while at 0° and 60° in alpha, respectively. When pitched, the low pressure became concentrated to the lower right hand corner of the measurement field. The high pressure on the left side of the measurement field decreased and spread more evenly around the HARS mount. The result was a more uniform flow field in the center of the test section.

The second goal of the testing was to document the flow uniformity with an empty test section. Data was collected in the testing plane with the same measurement limitations. The baseline plot is Figure 65, which contains data from Run 66. This plot shows the deviation from the mean flow at a dynamic pressure of 50 psf. The result was less than half of a percent deviation from the mean dynamic pressure throughout the measurement field. Not only is this true at 50 psf, but Figures 63, 64,

and 66 display that this is also true for a wide range of test section dynamic pressures. Figures 67 through 69 showcase the effect of running the motor at different RPM values on the flow uniformity results of the empty test section. For most of the runs, there is little to no change in the data. Figures 70 proves that collecting data in the reverse order makes no difference in the final results.

Figures 71 through 76 are representative plots of the flow uniformity for an empty test section at small dynamic pressure values. The same approach laid out in Equation 3.7 was used to calculate the percent deviation from the mean dynamic pressure. However, the dynamic pressure at each point is calculated using hotwire velocities instead of the Pitot tube pressures. The reason for this change was the use of a 1 psi pressure scanner in conjunction with the Pitot tube. The lack of resolution of the pressure scanner at small pressure values made the calculation of the dynamic pressure at each point uncertain. The hotwire velocity was used in Bernoulli's equation to calculate the dynamic pressure at each point. The density in the test section was approximated using the following idea gas law relation:

$$\rho_i = \rho_o \left(\frac{P_i}{P_o}\right) \left(\frac{T_o}{T_i}\right) \tag{3.8}$$

The lowest dynamic pressure of 0.05 psf is shown in Figure 71. A high pressure exists on the right side of the test section and a low pressure appears on the opposite side. As the dynamic pressure is increased to 0.25 psf, the flow becomes more uniform, but the high and low pressure areas still appear on their respective sides of the measurement field. The low pressure area is more dominant in this case. As the dynamic pressure increases, the flow becomes more uniform throughout the test section. As seen previously, at a dynamic pressure of 5 psf, the flow is extremely uniform throughout the test section. This implies that data of any test run at a dynamic pressure less than 1 psf should be viewed with skepticism.

D. Turbulence Intensity

A constant temperature hotwire anemometry system, shown in Figure 15, was used to collect data to calculate the turbulence intensity in the empty test section. The system was setup in the same manner as the flow uniformity testing. Data were collected in the center of the test section with the use of a 2.5 millimeter diameter Dantec hotwire. The setup is described in detail in the "Hot-wire Checklist" that is located in Appendix E.

The hotwire was calibrated in the same manner as previously described in this chapter. The anemometer was set to a DC voltage range of ±10 volts with a gain of 7.0 dB. Voltage data were collected at 16.384 kHz in 2 second intervals. A 1-Hz to 15-kHz bandpass filter was applied to the voltage signal out of the anemometer. Voltage signal data can be seen in Figure 79, located in Appendix C.

The turbulence intensity was calculated as a percent value of the free stream velocity. This was accomplished by dividing the root-mean-square value of the velocity time signal by the free stream velocity as shown:

$$Tu\,[\%] = \left(\frac{u_{rms}}{U}\right) \cdot 100 \tag{3.9}$$

The key results of the turbulence intensity investigation are shown in Figures 77 and 78. Figure 77 displays the turbulence intensity at the center of the test section during the three hotwire calibration runs. The three runs are in reasonable agreement and show the turbulence intensity tends to plateau at a value of approximately 0.25% of the free stream velocity. Since the calibration runs cover a wide range of dynamic pressures, the motor RPM was altered during the run. The solid black lines in Figure 78 outline where the data was collected.

Figure 78 is a map of the turbulence intensity levels over a range of motor RPM values and test section dynamic pressures. The turbulence intensities are lowest at

motor RPM settings less than 25% of the maximum RPM. At higher RPM settings, the turbulence intensity is lower at higher dynamic pressures. At high RPM and low test section dynamic pressures, the turbulence intensity increases. This is most likely caused by the propeller blades getting close to stall. At 100% motor RPM and 10 psf dynamic pressure in the test section, the turbulence intensity increases to a maximum recorded value of 0.51% of the free stream velocity.

The points labeled one through four on the plot in Figure 78 refer to the results contained in Figures 79 through 86. The first figure in each set contains the high speed voltage signal, such as Figure 79. The second figure in each set shows the power spectral density of the voltage signal in the frequency domain, such as Figure 80. These sets of figures exhibit how the power increases in the low frequencies at points of higher turbulence, reflecting the pattern in the voltage signal.

E. Nominal Motor Operating Conditions

As described in Chapter II, the test section dynamic pressure is calculated from the pressure differential measurement made across the contraction section. In order to ensure the test section dynamic pressure is accurate, the tunnel is calibrated bi-annually. This is done by mounting a Pitot tube in the center of the test section as shown in Figure 16. Then, the tunnel is run at a wide range of speeds while recording the pressures from the Pitot tube, used to calculate q_a, and the pressure differential across the contraction section, called q_{set}. The data is fit using a third order polynomial as shown in Figure 87. Since the linear term is four orders of magnitude larger than any of the other terms, the low order terms can be ignored. This leaves the following result:

$$q_a = +1.04196758\ q_{set} \tag{3.10}$$

Considering just the linear term indicates that there is a 4.2% increase in the dynamic pressure from the measurement of q_{set} to the measurement of q_a. This percent difference is corrected for using Equation 3.10 when the pitot tube is not installed in the test section.

After the motor was installed in May of 2012, one goal was to measure the dynamic pressure limitations at a full range of values for percent motor RPM. To do this, the motor was set at a percent RPM and the variable pitch blades were used to increase the dynamic pressure in the test section until the blades stalled or the max dynamic pressure of 105 psf was attained. Data was recorded every two seconds during these runs in order to capture the maximum dynamic pressure. This process was repeated over the full range of motor RPM values and the result is shown in Figure 88. This figure shows the process was repeated during two different tests. The gray range was the calculated operating region during the first test. The green range is the additional operating range that was measured during the second test. The difference between the two tests is due to cleaning the double screen located just upstream of the contraction section.

Static pressure measurements were collected down the length of the tunnel in order to help characterize the flow into the test section and approximate the load placed on the double screens. The results of these runs are displayed in Figure 90. The decrease in static pressure between the first and second measurement indicates the pressure drop across the screen. The static pressure crosses 0 around 2 feet in front of the beginning of the test section. This is evidence that the static pressure vents in the test section are not large enough to keep the test section at ambient static pressure at high dynamic pressures.

The static pressure drop across the screens was used to approximate the force on the screens. Equation 3.11 shows how the drag force was computed. The static

pressure difference across the screens was multiplied by the area of the screen and a bypass ratio, σ_s, based on the screen mesh and wire size. The brass, 18 mesh screens were approximated to have a 35% bypass ratio. The radius of the screens is 15 feet.

$$F_{D_s} = \Delta P_s \cdot \left(\pi {r_s}^2\right) \cdot \sigma_s \tag{3.11}$$

Figure 89 exhibits the approximate drag force on the screens as a function of the test section dynamic pressure. Using the minimal bypass ratio, the drag force was found to be 650 lbf at a dynamic pressure of 110 psf in the test section. To approximate the load on a single screen per foot, the maximum drag force was divided by twice the circumference of a single screen. The result is a minimal approximation of 3.45 lbf per foot. However, the screens collect debris and dirt throughout testing cycles. When this occurs, a bypass ration of 35% is no longer accurate and the force on the screen could increase to a maximum of 10 lbf per foot. Figure 88 also displays the effect of increased screen drag force on the operating conditions in the test section.

Table 5 contains information regarding suggested operation ranges for the motor RPM at differing test section dynamic pressure ranges. This table takes into account the operating limitations, flow uniformity, and turbulence intensity results.

Table 5: Suggested Motor Operating Ranges

Dynamic Pressure	Motor Setting	Turbulence Intensity
$<$ 1 psf	8 %	0.10 %
1 - 5 psf	20 %	0.15 %
5 - 10 psf	25 %	0.20 %
10 - 20 psf	30 %	0.25 %
20 - 30 psf	40 %	0.25 %
30 - 50 psf	50 %	0.25 %
50 - 100 psf	80 %	0.20 %

CHAPTER IV

INTERNAL BALANCE TESTING PRINCIPLES

The goal of this chapter is to standardize and document the testing procedure at the LSWT using reliability principles set forth by Walker [7]. The first section introduces principles of reliability for research applications. A thorough understanding of these ideas help researchers predict and avoid problems during an experiment. The second section summarizes ideas concerning the application of reliability principles to experimentation. The rest of the chapter applies these principles specifically to the LSWT. This chapter also describes the testing sequence at the LSWT and shows where new documentation and standard checklists are used to apply the principles that are set forth.

A. Principles of Reliability

Reliability and consistency in research can be difficult to achieve. In this thesis, reliability is defined as the ability to execute and maintain function in routine situations as well as unanticipated circumstances. Consistency is the capability of the people and systems to repeatedly perform tasks in a satisfactory manner. When conducting a scientific experiment, there are a number of items that must work in unison to achieve the end product.

In his book, Walker [7] reports a study which argues the main cause of errors in research stem from human factors. Walker states the probability of introducing human error into an experiment can be as high as 10^{-2} per complex operation. Therefore, after the completion of only a small number of complex tasks, it is probable that human error has been introduced into the experiment. Walker reports that omission,

or the failure to complete a required task, is the cause of 43 percent of all human related errors. The same study concluded that 61 percent of human error in research is caused by deficient documentation or a simple lack of knowledge and training.

Considering ways to decrease reliance on human actions in research can help minimize the error introduced by avoidable mistakes. To this end, Walker offers five general principles of reliability in research: simplicity, modularity, conservatism, margin-of-safety, and redundancy.

Walker emphasizes that simplicity is key to making fewer mistakes in a research environment. Practicing simplicity is particularly important in a university research setting with a frequent rotation of student workers. Another common reason for loss of simplicity in experimentation is the desire to create a general-purpose tool. This often leads to an elaborate solution instead of tailoring a simpler tool to fit the specific task at hand. Even so, adding complexity by automating certain tasks that are prone to human error can lead to more consistent results. Discretion must be used to determine whether the added intricacy will benefit the overall operation. Another benefit of creating simpler tasks is the increased ease of troubleshooting errors.

An effective method of implementing simplicity is through the use of modularity. Walker defines modularity as the subdivision of tasks. Modularity helps decrease complexity by making tools more fitted to a precise task. Subdivision encourages the understanding of how each part operates, while uncovering irrelevant intricacies. Modularity can be used to build reliable, elaborate systems through the creation of consistently simple parts that are easy to diagnose and repair when issues arise. However, modularity introduces errors called "sneaks", the assumption that if the subparts perform independently, the system as a whole will work. Avoiding sneaks can be achieved by testing the system after each additional module is incorporated.

Conservatism can also help avoid problems with reliability. Walker suggests that

the use of conservative technology instead of first generation products can help increase reliability and production. Secondly, it is vital to understand the benefit of conservative development in research. Improvement is essential, but making rapid, large changes can destroy reliability through unanticipated difficulties. Making incremental enhancements to items such as infrastructure and computer programs will help personnel detect negative advancements and mitigate a cascade of complications.

Walker notes that it is also critical to consider the margins-of-safety associated with an experiment. This can refer to both physical safety requirements and non-physical parameters. Whether true to not, an increase in margin-of-safety is usually associated with a decrease in overall performance. Researchers must resist the enticement to reduce needed margin-of-safety requirements in order to obtain better results. Directly related to margin-of-safety, redundancy is a another method of improving reliability. Methods of redundancy can range from having spare pieces of key experimental equipment to multiple computer analysis programs. However, because the application of redundancy methods often adds complexity, cost, and time, it should be applied only after other techniques of improving reliability have failed.

B. Application of Reliability Principles in Research

The Texas A&M Low Speed Wind Tunnel is a unique academic and commercial research laboratory. Reliability and consistency are imperative, but can be difficult to achieve when conducting diverse educational and commercial research. For this reason, it is not only central to understand what might degrade reliability, but also what steps can be taken at the LSWT to consistently improve the results.

Human omission is the most common research error according to Walker [7]. Planning and preparation is the first way to defend against these types of oversights.

To ensure that a plan is properly detailed, multiple people with different specialties should review it. When creating a plan, consider the design of the hardware and software systems involved. Walker lists a thorough set of arguments to help minimize human error through system design. These points include: the users understanding of the goal, minimizing mental processes, arrangement that leads to intuitive outcomes, and the use of natural constraints to guide the users decision making.

Walker argues that fatigue is the most significant influence in human error. A fatigued worker will be prone to mistakes due to memory-lapses and a shortened attention span. Regrettably, a fatigued worker is rarely conscious of the extent to which their abilities have declined. Shifts should be implemented so that personnel do not work at least 11 hours between shifts and more than three night shifts in a row. Automation of tasks can help avoid error, even with a fatigued worker.

Walker suggests that communication is the key to avoiding oversights and it begins with the division of labor, which gives every worker a purpose. Walker states that over dependence on memory is the most frequent psychological cause of error in research [7]. Immediately take detailed notes, measurements, and informative reminders for other workers in a designated location. Walker encourages the use of checklists for common tasks as one of the best practices for avoiding omission errors.

Manuals and other documentation should be created to detail significant aspects of research that pertain to a particular facility. These types of documents should include relevant tables, charts, and pictures to help the reader understand the details of a specific system. Keep read-only, digital copies of all documentation and checklists in a place that is accessible to all staff members.

In summary, the LSWT should have a routine process when creating testing plans so that multiple, key personnel have a chance to influence the preparation. This should include standard paperwork and checklists for each major type of test

performed at the facility. Documentation should consist of pre-planning questions for customers as well as design, installation, and test execution checklists. A place to record key information should be kept with each checklist. For larger tests, a plan must be created before the test date for shifts and work rotation in order to keep employees fresh and engaged.

C. Internal Balance Pre-Test Considerations

When planning an internal balance test at the LSWT, multiple issues should be resolved before the test to increase productivity. First, the customer and test engineer need to understand time limitations. These include: overall test length, restraints imposed by non-testing activities, and operational hours. The normal operating hours at the LSWT are 10-hour days Monday through Friday. However, 30 minutes in the morning and evening are reserved for start-up and shutdown procedures. Other non-testing activities include set-up, teardown, model changes, and regular checks of testing equipment.

An initial test matrix must be constructed that lists the data acquisition runs that the customer would like to complete during the test. Non-testing activities need to be considered along with the overall length of the test. For internal balance tests, a half-day should be reserved for installation and de-installation. The order of the data acquisition runs in the test matrix should be arranged to limit the number and complexity of required model changes.

Decreasing the test time through manipulation of the test matrix can be achieved by considering the sweep types and resolution. Sweep types refer to the variable to be altered during a data acquisition run. The LSWT can adjust the model location in pitch, yaw, and roll as well as the speed of the tunnel. Pitch sweeps tend to be the

most time efficient due to the agility of relocating the HARS mount. Yaw sweeps are commonly the least time efficient. Choosing the correct sweep type for the test can save a significant amount of time. It is also critical to properly define the resolution of these sweeps. The time it takes to sweep the model in pitch can be drastically changed by the choice of angle increment. The customer and test engineer must decide what the time versus resolution trade off should be for a specific test or run.

The customer should clearly define the desired data format and output. Final data can be provided more quickly if the test engineer knows what test considerations are of concern to the customer and how the data files should be structured when delivered. For complex tests, customers should not expect final data on the first day of their test if they do not define the data output before the test begins.

D. Test Setup Procedures

To begin an internal balance test, several setup procedures must be followed. Approximately half of a day should be reserved for installation and setup activities.

The first major step to begin an internal balance test is the installation of the HARS mounting system. The "HARS Installation Checklist" that details each step can be found in Appendix E. The process begins by zeroing out the external balance. This is a precautionary measure to ensure that the model and HARS mount do not overload the external balance. The test section roof and floor plate are removed to allow access to the clamps under the floor. Once the clamps are appropriately located, two small struts are set into the clamps. The cradle-halves that mount HARS to the external balance are bolted to the flange on the top of each strut. With the cradle-halves in place, the alignment block is used to space the clamps before tightening them into place. The upper and lower turntables are aligned with their long axes

oriented down the length of the test section before the alignment block is removed.

The HARS mount is unbolted and hoisted from its stand and into the test section via the overhead crane. Before setting HARS into place, the four HARS motor cables and three roll motor cables are passed through the floor and into the balance room. After, HARS can be set into the cradle-halves and bolted into place. To finish the installation, tighten the clamps to set the position of the struts and the HARS mount. With HARS in place, the cables are connected and the HARS program started as described on the checklist. With the connection made, the HARS mount is brought out of storage to a testing position, centered in the test section.

Once the HARS mount is in place and an appropriate sting is selected and attached, the internal balance can be installed. The "Internal Balance Installation Checklist" can also be found in Appendix E. The internal balance cables are passed through the internal bore of the sting, the HARS cable tubing, and into the balance room. This must be done gently to ensure the cables are not damaged. Next, the internal balance is set into the end of the sting and located by gently setting the anti-rotation pin. Push-on bolts are used in the setscrew holes to firmly push the balance into the sting. After, the anti-rotation pin is firmly set into place. Last, the push-on bolts are removed and opposing setscrews are placed to secure the balance.

With the internal balance installed, the wires are hooked up to the SCXI block in the balance room. There are 24 connections that must be made in the order described by the checklist. With these connections made, the internal balance is zeroed in roll and pitch with the use of the "cal-body block" and "bubble inclinometer." Next, the internal balance program is started as described in the checklist. Note the force and moment readings as they should be small, but not necessarily zero. If a reading is much larger than the others, it is likely that a connection was not made properly. If all readings are reasonable, the balance null offset is performed. After, all of the

loads should be reading approximately zero.

The next step is to perform sting deflections, which allow the calculation of an angle deflection per pound force of loading. These are used to correct the model position readings after a data run is performed. The "Sting Deflections Checklist" exists in Appendix E. The sting deflections must be completed in the vertical direction to correct the pitch angle, α. They must also be carried out in the horizontal direction to correct the yaw and roll angles, β and γ respectively. The roll angle correction is only applied when the "blade mount" is in use.

To begin the horizontal deflections, the deflection stand is setup and screwed to the floor to prevent movement. The cal-body block is installed onto the internal balance and set with a pin. The "trapeze" is a cable system with a plate that is used to hold the hanging weights. It is attached to the cal-body block and suspended from the deflection stand. A plum bob is dropped from the end of the cal-body block to the floor of the test section where a ruler is taped into place. For the vertical deflections, the deflection stand is not needed as the trapeze can be suspended directly from the cal-body block. In both cases, the bubble inclinometer is mounted to the top of the cal-body block to read the angle deflections. The last step is to preload the internal balance by placing an appropriate amount of weight on the trapeze for 1 minute and then unload the weights.

To perform the sting deflections, weights are sequentially added to load the internal balance. For the horizontal deflections, the trapeze wire is leveled after each weight is added. Any motion of the trapeze is stilled so as to not corrupt the readings. After adding each weight, the deflection data is recorded. This includes an angle deflection, a distance deflection, and recording the balance load readings on the "DAQ computer." This process must be repeated for each weight and the data recorded in the space provided on the checklist.

E. Internal Balance Testing Methodology

There are a variety of concerns that are examined when carrying out an internal balance test. A test engineer and customer must understand that additional runs may be necessary to accomplish the test goals and provide precise and accurate data. A listing of these items can be found in the "Internal Balance Testing Checklist" in Appendix E. These considerations include pre-test items such as sting deflections, pressure readings, and a foul circuit. The foul circuit allows a test operator to recognize and fix a problem as well as re-run the test to obtain uncorrupted data.

When performing an internal balance test, there are several considerations that should be taken into account at the beginning of a test. The first key decisions is the choice of dynamic pressure at which the tests are going to be completed. The customer often knows what the dynamic pressure needs to be, but a few data runs should be completed to check for Reynolds number dependency. These runs must continue until the test engineer and customer are satisfied with the results.

Another key component of wind tunnel testing is flow angularity. When the HARS mount and model are placed in the test section, the non-uniform blockage causes the flow through the test section to become slightly angled. If this angle is unaccounted for, it can lead to errors in the angle of attack of more than a degree. This occurrence can be easily corrected for if the appropriate data runs are completed. The model should be tested over a range of pitch angles in the same configuration and at the same dynamic pressure, both upright and inverted. The upright and inverted runs can be compared to determine the flow angularity and correct the data.

Lastly, it is necessary to consider the repeatability and sensitivity of a test. Use of the digital scale as described in the previous section to test the response of the internal balance at the beginning of every test day will show flaws in the balance readings

before faulty data is recorded. It is good testing practice to repeat an important run at least once during a test. This reiteration will help disclose a problem early and increase repeatability. Lastly, performing a few runs that are only slightly different from the baseline test case can be revealing. This is the lowest priority of all the suggestions in this section, but can be helpful in understanding unexpected results and indicating corrupt data.

CHAPTER V

DATA ANALYSIS AND UNCERTAINTY CONSIDERATIONS

The goal of this chapter is to outline the steps of a data analysis routine and estimate the uncertainty in the final data output through investigating the error introduced at each point in the process. The first section covers the techniques and concepts used to perform the uncertainty analysis in the later sections. The second section defines the uncertainty in the initial data set before introducing the analysis equations. The goal of the uncertainty analysis is to make realistic and systematic estimation of the errors associated with a given experiment. The last section contains data from an LSWT test with their respective uncertainty values calculated using the information outlined in this chapter.

A. Overview of Uncertainty Analysis Techniques

The true value of an experimental measurement is often unknown, forcing researchers to rely on approximations of the error. In this thesis, uncertainty is defined as the estimation of the error in a set of data. Bevington and Robinson [8] make several distinctions before addressing the application of uncertainty analysis principles. The first of these is accuracy versus precision. Accuracy is how close a measurement is to the true value while precision means how many digits can be confidently ascribed to a number. Another contrast presented by Bevington and Robinson is systematic versus random errors. They define systematic errors as those kinds of errors that result in "reproducible discrepancies." Errors of this kind are a result of experimental technique and cannot be accounted for with statistical analysis, but from knowledge of the equipment and test setup employed. On the other hand, random errors are the

results of fluctuations in the data that differ from experiment to experiment. These types of errors are more easily studied with statistical methods through the repetition of measurements.

Another distinction is made between instrumental and statistical uncertainty. Instrumental uncertainty is similar to the concept of precision as previously defined in this chapter. Examples of instrumental uncertainty are malfunctioning equipment, faulty test setup, and human error in observation. In comparison, statistical uncertainty parallels the definition of accuracy and arises due to statistical fluctuations in recorded measurements.

It is typical to assume the normal error or Gaussian distribution as the form of the parent distribution for random errors. The Gaussian distribution is a well tested probability density function characterized by its mean and standard deviation. Using the definition of the Gaussian distribution, Bevington and Robinson formulate the error propagation equation:

$$\sigma_x{}^2 = \sigma_u{}^2 \left(\frac{\partial x}{\partial u}\right)^2 + \sigma_v{}^2 \left(\frac{\partial x}{\partial v}\right)^2 + ... + 2 \cdot \sigma_{uv}{}^2 \left(\frac{\partial x}{\partial u}\right)\left(\frac{\partial x}{\partial v}\right) + ... \tag{5.1}$$

This propagates measured uncertainties σ_u, σ_v, and their covariance into the resulting uncertainty represented by σ_x. Often, the covariance terms, such as σ_{uv}, are uncorrelated or are small in relation to the other terms and can be ignored. This results in the simplest form of the error propagation formula:

$$\sigma_x{}^2 = \sum_i \sigma_{ui}{}^2 \left(\frac{\partial x}{\partial u_i}\right)^2 \tag{5.2}$$

Bevington and Robinson suggest making quick approximations of the uncertainty contributed by each term. They outline a rule to ignore terms that contribute less than 10% of the largest uncertainty term. Sometimes, the uncertainty of a term is inflated due to suspect, or outlying, data points. In that case, the authors suggest using

Chauvenet's criterion to establish an appropriate condition for removing or ignore such data points. This criterion states that a data point should only be discarded if the suspect measurement falls more than three standard deviations away from the mean of the data sample.

B. Examination of the Uncertainty in Measurements

To begin an uncertainty analysis of internal balance testing, the uncertainties of all measurement parameters, instrumental and statistical, must be defined. This includes data recorded to define the flow in the test section, the position of the model, and the force and moment readings from the internal balance. The uncertainty of the readings from the internal balance will be discussed first in this section.

The calibrations of the Mark X and Mark XIII internal balances by Force Measurement Systems in 2008 provided uncertainty calculations of the gages as a percent of the maximum allowable loads. The internal balances were calibrated according to the American Institute of Aeronautics and Astronautics standard for internal balances [5]. Each balance gage outputs a voltage signal. The 6 by 96 calibration matrix is then employed in order to obtain the force and moment readings from the six voltage measurements.

The first task is to validate the internal balance calibration using the data recorded while performing sting deflections. Validating the calibration will allow the utilization of the uncertainty values in Table 6. This data includes the internal balance force and moment outputs as a function of a known applied weight. Figures 97 through 100 in Appendix F contain the results including a linear fit of the data. The parameters with their associated uncertainties are printed in the top left corner of each plot. The dashed red line indicates the uncertainty in the result of the

fit equation. The Mark X has lower load limitations, so the resulting uncertainty in the fit appears larger than the Mark XIII.

The fit of the normal force is more accurate in both cases than the fit of the side force. This is due to errors in the experimental setup and not the readings from the balance. In order to test the side force gages, a stand with a pulley is set up and used to apply a force. There is not currently a way to properly align this stand with the balance and the result is less accuracy in the data output.

However, for both the Mark X and Mark XIII, the data show that the balances conform to their calibrations. As previously stated, this validates the use of the calibration data and associated uncertainties. Table 6 contains the maximum load values and reported uncertainties in each gage for both the Mark X and Mark XIII internal balances provided by Force Measurement Systems in 2008. These validated uncertainties are used for the analysis in this section.

Table 6: Uncertainty of the Internal Balance Gages

		Mark X		Mark XIII	
Measurement	Symbol	Max Load	Uncertainty	Max Load	Uncertainty
Normal Force Forward	$N1$	±100 lbf	±0.116 lbf	±500 lbf	±0.370 lbf
Normal Force Aft	$N2$	±100 lbf	±0.084 lbf	±500 lbf	±0.355 lbf
Side Force Forward	$S1$	±50 lbf	±0.059 lbf	±500 lbf	±0.470 lbf
Side Force Aft	$S2$	±50 lbf	±0.052 lbf	±500 lbf	±0.460 lbf
Rolling Moment	RM	±120 in-lbf	±0.437 in-lbf	±800 in-lbf	±1.728 in-lbf
Axial Force	AX	±60 lbf	±0.080 lbf	±150 lbf	±0.093 lbf

The next step is to define the uncertainty in the readings related to the model position and test section conditions. The model must be aligned in the three degrees of freedom that are used during testing: pitch (α), roll (γ), and yaw (β). The pitch

angle is fixed using the HARS mount described in Chapter II. Before a model is mounted, the HARS unit sent to 0° in pitch using the computer program. The digital inclinometer, accurate to 0.05°, is then used to check that the sting and bullet are level. The balance block for the model is designed so that the model angle of attack matches the HARS unit. Therefore, the uncertainty in the pitch is ±0.05°. A large portion of this uncertainty is related to the design of the balance block. The model roll is also fixed by the HARS mount. Again, the related factors are the computer program and the balance block. Subsequently, the uncertainty in the model roll angle is ±0.05°. Lastly, the model yaw is fixed using the large turntable beneath the test section. In order to align the model yaw angle, a transverse is set up in the center of the tunnel downstream of the test section. Two points on the model, forward and aft, are then located on the centerline of the tunnel. This process results in a model yaw angle uncertainty of ±0.05°.

The calculation of the dynamic pressure in the test section is described in Chapter II. The measurement of q_{set} has an uncertainty of ±0.02 psf. Then, the value for q_a is defined using a third order polynomial curve fit. The polynomial fits the data extremely well with a value of 0.999 for χ^2. Therefore, this curve fit adds little uncertainty to the effective test section dynamic pressure. The uncertainty values for the rest of the measurement were taken from documentation on the hardware used to record the data. The uncertainty for the pressure measurements is ±0.01 psf for the Measurement Systems 32-port scanners. The uncertainty for the test section temperature is ±0.10° F from the thermocouple mounted in the test section.

Table 7 shows a listing of parameters that are commonly recorded during an internal balance test at the LSWT. The table also gives approximations of the uncertainty associated with each parameter.

Table 7: Uncertainty of Measured Testing Parameters

Measurement	Symbol	Uncertainty
HARS Alpha	α	$\pm 0.05^\circ$
Turntable Beta	β	$\pm 0.05^\circ$
HARS Phi	ϕ	$\pm 0.05^\circ$
Test Section Dynamic Pressure	q_a	± 0.02 psf
Total Pressure	P_t	± 0.01 psf
Static Pressure	P_s	± 0.01 psf
Barometric Pressure	P_{baro}	± 0.01 psf
Test Section Temperature	T	$\pm 0.10^\circ$ F

C. Data Acquisition and Reference Frames

The first step after collecting data with the internal balance is to parse the 5-force and 1-moment gage readings into 3-force and 3-moment readings. This is accomplished using the system of formulas outlined in Equation 5.4. The uncertainty in the forces and moments is calculated using the respective uncertainty equation and data from Table 6. In order to make the equations simpler, the two normal force and two side force gages are assumed to have the same uncertainty as shown in Equation 5.3. This value is the maximum percentage of the two values found in Table 6.

$$\begin{aligned} \sigma_{N1} \approx \sigma_{N2} = \sigma_N = max\left(\sigma_{N_i}\right) \\ \sigma_{S1} \approx \sigma_{S2} = \sigma_S = max\left(\sigma_{S_i}\right) \end{aligned} \tag{5.3}$$

The balance pitch and yaw lengths, l_p and l_y respectively, are not included in the propagation equation of their respective moments since they are nominal values and are accounted for during the balance calibration. The values for these variables are

recorded in Table 4 and are different for the Mark X and Mark XIII balances.

$$\begin{array}{lcllcl} F_N & = & N1 + N2 & \sigma_{F_N} & = & \sigma_N\sqrt{2} \\ F_S & = & S1 + S2 & \sigma_{F_S} & = & \sigma_S\sqrt{2} \\ F_A & = & AX & \sigma_{F_A} & = & \sigma_{AX} \\ M_P & = & (N1 - N2)\, l_p & \sigma_{M_P} & = & l_p\sigma_N\sqrt{2} \\ M_R & = & RM & \sigma_{M_R} & = & \sigma_{RM} \\ M_Y & = & (S1 - S2)\, l_y & \sigma_{M_Y} & = & l_y\sigma_S\sqrt{2} \end{array} \tag{5.4}$$

The internal balance measures forces and moments in a body fixed reference frame. The axes of this frame align with the balance measurement axes for the three force components. This means the 1-axis points out the back of the model, the 3-axis points through the top of the model, and the 2-axis completes the right handed coordinate system out the side of the model. This reference frame, shown in Figure 2, moves with the model and is used for most of the data analysis in this chapter.

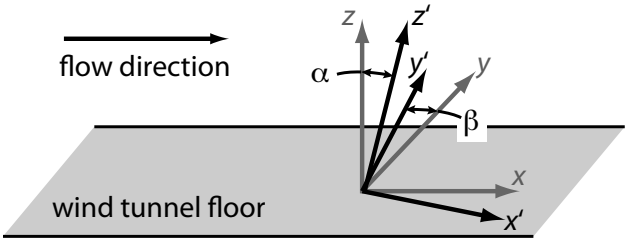

Fig. 2: Body frame and internal balance measurement coordinate system.

The other reference frame utilized in this chapter is the traditional wind axis frame that is defined by Barlow, Rae, and Pope [9] and shown in Figure 3. This is a fixed coordinate system in which the 1-axis points upstream, the 3-axis points through the floor of the test section, and the 2-axis completes the right handed system. The wind force and moment coefficients will be computed in this frame in a later section.

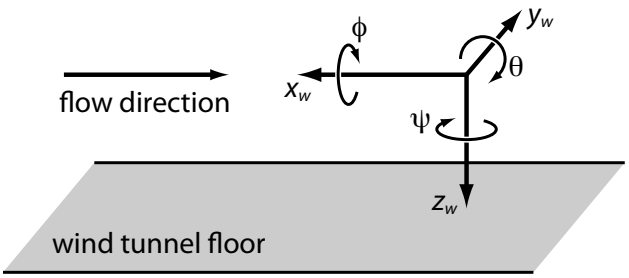

Fig. 3: Traditional wind axis frame and coordinate system.

Note that lift and drag are equal to the negative value of the forces in the x and z directions in this frame.

D. Sting Deflections

Before installation of the model for an internal balance test, sting deflections must be completed. This process is described at length in Chapter IV. The goal of performing sting deflections is to apply a linear correction to the pitch, roll, and yaw angles due to deflection of the sting caused by applied aerodynamic loading on the model. The result of performing sting deflections can be seen in Figures 101 through 103. The deflection in arc minutes is plotted against the applied load and the data is fit linearly. The normal deflections are performed at three locations. For each test, the resulting derivative of deflection per pound force is equal to the slope of the curve fit, as shown below for the pitch angle:

$$\alpha_n = \alpha_o + mF_N \tag{5.5}$$

In this equation, m refers to the derivative of the deflection as a function of applied load. These values are printed in the top left corner of Figures 101 through 103. The same equation is applied to the yaw and roll angles as a function of applied side force. The uncertainty in α_o can be found in Table 7 while the error in the normal force was calculated in the previous section. The uncertainty in the slope of the curve

fit is given as an output parameter of the fit function. The result for the normal force correction can be calculated using the following equation derived to describe the error propagation in this process:

$$\sigma_{\alpha_n}{}^2 = \sigma_{\alpha_o}{}^2 + \sigma_m{}^2 \left(F_N\right)^2 + \sigma_{F_N}{}^2 \left(m\right)^2 \tag{5.6}$$

The uncertainty values for all three angles were on the order of 10^{-3} degrees per pound force. In this case, the error added by the normal force correction is small, leaving the uncertainty in the pitch angle to be approximately $\pm 0.05°$.

E. Static Tare

Before making a data run, a wind-off static tare is performed. The resulting tare data allows the force due to gravity to be removed from internal balance readings acquired during the wind-on data run. The model is moved through the degree of freedom that will be tested while the internal balance measurements are recorded. There are two methods to perform a static tare. First, a wind-off data point can be recorded to match every increment in the degree of freedom to be tested. This permits a point-by-point subtraction of the static tare from the wind-on data. Second, due to the nature of a gravity tare, a wind-off data point can recorded at a fraction of the points to be tested. Then, the wind-off data can be fit with a series of sine and cosine functions. This allows the static tare to be subtracted from the wind-on data with the use of a series of functions. The benefit to this method is reduced testing time spent taking wind-off data by decreasing the number of recorded points. This method is also versatile if the wind-on recorded data points are changed during a test. Also, using a fit-style tare provides increased accuracy in the normal force and pitching moment.

The uncertainty in the static tare is simple to compute when using the point

by point tare method. The results is summarized in Equation 5.7. The value of the uncertainty on the right side of the equation comes from the appropriate force or moment uncertainty as defined in Equation 5.4. Since these equations are invariant between wind-on and wind-off data runs, the uncertainty will be the same for the forces and moments in both cases.

$$\sigma_{F/M_{i_n}} = \sigma_{F/M_{i_o}}\sqrt{2} \tag{5.7}$$

When using the curve fit subtraction method, the uncertainty is more difficult to define. Static tare data from a recent test at the LSWT is shown in Figures 105 and 106. The data has been fit as shown in Equation 5.8. Note that only the normal force, axial force, and pitching moment need to be fit. Since the internal balance is body fixed, these are the only parameters that vary with pitch angle. There is no variation in the balance readings with a change in yaw angle.

$$\begin{aligned} F_N &= W_N \cos(\alpha) + B_N \\ F_A &= W_A \sin(\alpha) + B_A \\ M_P &= W_N \left[X_N \cos(\alpha) - Z_N \sin(\alpha)\right] + B_N \end{aligned} \tag{5.8}$$

These equations fit the necessary balance outputs as a function of pitch angle. As can be seen in Figure 105, the curve is well aligned with the tare data. The values of the fit coefficients and their uncertainties are printed in the top left corner of the figure. Notice that the forces and moments go through zero since the balance null offset was performed with the model installed. These equations are then subtracted from the wind-on data as a function of the pitch angle. This is the reason it is important to correct the angles for sting deflections before performing the static tare.

In order to calculate the error in the fit method, the uncertainties of both the wind-on forces and the fit parameters must be known. The uncertainties in the

forces and moments are calculated using Equation 5.4 in a previous section. The uncertainties in the fit coefficients are output of the fit function. Note that the uncertainty values given in Figure 105 are relatively small compared to the value of the corresponding parameter. Equation 5.9 shows the simplified version of the error propagation equations for the forces and moment being fit. The terms related to the fit coefficients and their covariance can be ignored according to Bevington and Robinson's Rule as long as the uncertainty for all of the coefficients is less than 0.25 lbf. At this point, the terms that were ignored begin to grow large enough to influence the final result.

$$\begin{aligned} {\sigma_{F_{N_n}}}^2 &= {\sigma_{F_{N_o}}}^2 + {\sigma_\alpha}^2 \left[{W_N}^2 \sin^2(\alpha) \right] \\ {\sigma_{F_{A_n}}}^2 &= {\sigma_{F_{A_o}}}^2 + {\sigma_\alpha}^2 \left[{W_A}^2 \cos^2(\alpha) \right] \\ {\sigma_{M_{P_n}}}^2 &= {\sigma_{M_{P_o}}}^2 + {\sigma_\alpha}^2 \left\{ {W_N}^2 \left[X_N \sin(\alpha) + Z_N \cos(\alpha) \right]^2 \right\} \end{aligned} \tag{5.9}$$

Figure 106 shows the non-fit parameters as a function of pitch angle. This shows that all of the values remain close to zero throughout a range of pitch angles as expected. The side force is fit as a function of roll angle in order to calculate potential misalignment in the model installation. In this test, the fit calculates a model roll misalignment of +0.05 degrees. However, the parameters are small enough to be within the internal balance uncertainty limits of zero.

F. Flow Angularity

Wind tunnel testing creates unique issues for test design and data processing. Many models tested in wind tunnels are designed to operate in an open atmosphere. However, most wind tunnels are enclosed and the boundaries constrain the airflow around the model. Therefore, a necessary part of wind tunnel testing is to correct for the restrictions that are placed on the model due to the testing environment.

It is often seen that wind tunnels do not have aligned flow in the direction of the test section. Although the effect can be small, flow angularity should be accounted for in every test. This is the increment in angle of attack that the model experiences due to misaligned flow in the test section. Flow angularity can be calculated in most instances by running a model in its upright and inverted configurations and comparing the normal force versus angle of attack. Data from a previous test at the LSWT is shown in Figure 104 for both the upright and inverted configurations.

The method utilized to measure the flow angularity is an abstraction and is only first order accurate. To calculate this value, both the upright and inverted sets of data are fit linearly and then the slopes are averaged. Each set of data is then re-fit with the averaged slope to determine the x-intercepts. Once this is done, the flow angularity and corrected model angle of attack can be determined using:

$$\begin{aligned} \Delta\alpha &= \left(\alpha_{o_{inv}} - \alpha_{o_{up}}\right)/2 \\ \alpha_n &= \alpha_o + \Delta\alpha \end{aligned} \tag{5.10}$$

For internal balance tests at the LSWT, a typical value for the flow angularity in pitch is approximately 1.5° of upflow. The flow angularity correction has no influence on measured values of interest dependent on internal balance readings. Examples of parameters unaffected by this process are the maximum lift coefficient, the drag polar, and the lift curve slope. The error in the flow angularity measurement is dependent on the uncertainty in the original angle of attack from Eqaution 5.6 and the uncertainty in the x-intercepts. The error propagation in the angle of attack due to the flow angularity correction is:

$$\begin{aligned} {\sigma_{\Delta\alpha}}^2 &= \left(\tfrac{1}{4}\right)\left({\sigma_{\alpha_{o_{inv}}}}^2 + {\sigma_{\alpha_{o_{up}}}}^2\right) \\ {\sigma_{\alpha_n}}^2 &= {\sigma_{\alpha_o}}^2 + {\sigma_{\Delta\alpha}}^2 \end{aligned} \tag{5.11}$$

A flow angularity correction can be applied in the same manner to increment

the yaw angle. The upright and inverted side force as a function of yaw angle will yield the appropriate angle. This is not addressed in depth here since the yaw angle correction has been found to be much smaller than the pitch angle correction during previous tests at the LSWT. This also implies that the uncertainty in the pitch angle is much larger than that of the other angles due to the upflow in that direction. The HARS mount adds a considerable portion of the blockage to the lower half of the test section. This is the likely cause to the consistent up flow angle calculated during testing. However, the lack of asymmetry from left to right in the test section leads to a yaw angle correction that is significantly smaller than that of the pitch angle.

G. Solid and Wake Blockage

There are a number of steps that are required in the testing sequence and data processing to correct for the effects of the wind tunnel walls on the model. Multiple methods can be used to evaluate the wind tunnel boundaries and the consequence of the model in the test section, but one such approach, developed by Glauert [9], is the method of images. In order to bound the vortex pair produced by a lifting body, a double infinite vortex system can be used to produce a zero streamline at the location of each of the tunnel boundaries. This is one of many items to take into account during a wind tunnel test.

Wind tunnel data must be corrected for two types of blockage effects. First, solid blockage result from placing a model into the test section, thereby reducing the cross sectional area for the airflow. Due to conservation of mass, the reduced area for low speed flow means that the streamlines around the model are moving faster than they would in free flight. This causes extra force to be placed on the model that must be accounted for in the data reduction. Second, wake blockage is a similar effect caused

by the wake deficit behind the model that decreases the area of the free-stream flow. Since the airflow is bound within the tunnel walls, the presence of diminished flow velocity behind the model decreases the overall area available for free-stream flow in the test section, causing the free-stream flow to appear faster that it would in a free flight with commensurately larger forces.

In order to account for these effects, solid and wake blockage correction factors can be calculated from model and test section parameters. Equation 5.12 can be used to calculate the solid blockage correction factors. The κ_i and τ_i parameters can be derived from figures found in the text by Barlow [9]. These parameters are characteristic to the model and test section dimensions. The variable C is the test section cross-sectional area, which is 68 ft^2 in the usual LSWT 7 ft by 10 ft configuration. These correction factors are a non-dimensional volume correlation between the model volume and test-section representative volume represented by $C^{\frac{3}{2}}$ which is 561 ft^3.

$$\begin{aligned} \epsilon_{wing} &= \left(\kappa_1 \tau_{1w} V_w\right) / C^{\frac{3}{2}} \\ \epsilon_{body} &= \left(\kappa_3 \tau_{1b} V_b\right) / C^{\frac{3}{2}} \end{aligned} \tag{5.12}$$

Wake blockage is a function of the model drag. An initial estimate of the drag and the associated wake blockage correction factor can be calculated using Equation 5.13. To calculate the wake blockage correction factor, it is necessary to use the uncorrected test section dynamic pressure. This is acceptable since the correction is small and the approach being utilized is linear.

$$\begin{aligned} D &= \left[F_A \cos(\alpha) + F_N \sin(\alpha)\right] - \left[F_S\right] \sin(\beta) \\ \epsilon_{wake} &= \frac{D}{2 q_a C} \end{aligned} \tag{5.13}$$

With these parameters, the total correction factor can be calculated and then used to increment the test section dynamic pressure using:

$$q_c = q_a (1 + \epsilon_{wing} + \epsilon_{body} + \epsilon_{wake})^2 \tag{5.14}$$

The uncertainty associated with the blockage correction is handled differently than the previous equations. This is due to the fact that the goal of wind tunnel experimentation is to understand more about a model in free flight. The blockage correction equations are built from principles that require some approximation in order to subtract the effect of the test section boundaries from the data.

$$\sigma_{q_c}{}^2 = \sigma_{q_a}{}^2 + (2q_a\epsilon_T)^2 \tag{5.15}$$

Since the results of these equations are small and approximations are already being used, the uncertainty in the correction is assumed to be equal to the correction itself as shown in above.

H. Additional Correction Considerations

Depending on the nature of a specific test, there are other corrections that can be considered. The first of these is a cavity pressure correction. Since the internal balance is mounted to the HARS unit with either a traditional or blade sting, a hole must exist for the sting to penetrate the model outline. Due to this, the pressure that would normally act on the model base is not being measured. Instead the pressure acting on a similar area inside the model cavity is included in the internal balance reading. To account for this, the force induced by the cavity pressure must be subtracted out of the measured force and the missing force due to the base pressure must be added.

To correct for the applied force, pressures are recorded in the model cavity and on the base surface around the hole in the model. Generally, two to four measurements of each type are documented and then averaged to obtain a better sample. The base and cavity areas on which the respective pressures are acting are known. In this example, the two areas are approximately equal and therefore only one area

measurement will be used. The blade mount was utilized in this test, which means the correction is made to the normal force reading from the internal balance. The subsequent correction equation is:

$$F_{Nn} = F_{No} + (P_b - P_c) A \tag{5.16}$$

The uncertainty terms that depend on the pressures are small enough that they able to be dropped. This may not be true if the area becomes large, but most internal balance tests will not have a large characteristic cavity area. The uncertainty term due to the area cannot be ignored since the pressure differential between the base and cavity can be large enough to offset the small uncertainty in the area itself. The magnitude of this term can be difficult to bound, so it is better to leave it in the equation. This gives the resulting equation:

$$\sigma_{F_{Nn}}{}^2 = \sigma_{F_{No}}{}^2 + \sigma_A{}^2 (P_b - P_c)^2 \tag{5.17}$$

The next consideration is streamline curvature. The curvature of the streamlines is altered since they must be contained within the test section boundaries. This causes the body to appear to have more camber than it actually does by increasing the apparent angle of attack. The values for τ_2 and δ can be calculated using figures found in the text by Barlow [9]. A distinct, but mathematically related concern is normal downwash. This refers to a portion of induced flow in the lift direction at the location of the model caused by the presence of the test section boundaries. Normal downwash makes the lift too large and the drag too small at a given angle of attack. The corrections to the angle of attack, pitching moment, and drag force are:

$$\begin{aligned} \Delta\alpha_{ac} &= \delta \left(\tfrac{L}{Cq_c}\right) (1 + \tau_2) \\ \Delta M_{p_{sc}} &= \left(\tfrac{c}{8}\right) \Delta\alpha_{sc} \left[\tfrac{dL}{d\alpha}\right] \\ \Delta D_{ND} &= \delta \left(\tfrac{L^2}{Cq_c}\right) \end{aligned} \tag{5.18}$$

Much like the blockage corrections, the streamline curvature and normal downwash equations are used to account for effects that are presented by the presence of the test section walls. As before, the associated uncertainty is assumed to be as large as the correction itself. The resulting propagation equations are:

$$\begin{aligned} {\sigma_{\alpha_n}}^2 &= {\sigma_{\alpha_o}}^2 + {\Delta\alpha_{ac}}^2 \\ {\sigma_{F/M_n}}^2 &= {\sigma_{F/M_o}}^2 + {\Delta F/M_i}^2 \end{aligned} \tag{5.19}$$

I. Coordinate Transformations

The final steps in the data analysis process are to transfer the moments to the desired moment reference center, rotate the reference frame to acquire wind axis forces and moments, and make the data non-dimensional. The moment transfer from the balance moment center (BMC) to the moment reference center (MRC) can be seen in Equation 5.20. The variables Δx, Δy, and Δz are measured from the balance moment center in the body axis frame. Note that in some cases, these variables could be negative.

$$\begin{aligned} M_{R_{MRC}} &= M_{R_{BMC}} + (F_S \Delta z - F_N \Delta y) \\ M_{P_{MRC}} &= M_{P_{BMC}} + (F_N \Delta x - F_A \Delta z) \\ M_{Y_{MRC}} &= M_{Y_{BMC}} + (F_A \Delta y - F_S \Delta x) \end{aligned} \tag{5.20}$$

The associated error propagation equations are shown in Equation 5.21. Note that the terms due to the position of the MRC in reference to the BMC are dropped from these equations. They are less than 10% of the original uncertainty in the moment and can be ignored.

$$\begin{aligned} \left(\sigma_{M_{R_{MRC}}}\right)^2 &= \left(\sigma_{M_{R_{BMC}}}\right)^2 + {\sigma_{F_S}}^2 (\Delta z)^2 + {\sigma_{F_N}}^2 (\Delta y)^2 \\ \left(\sigma_{M_{P_{MRC}}}\right)^2 &= \left(\sigma_{M_{P_{BMC}}}\right)^2 + {\sigma_{F_N}}^2 (\Delta x)^2 + {\sigma_{F_A}}^2 (\Delta z)^2 \\ \left(\sigma_{M_{Y_{MRC}}}\right)^2 &= \left(\sigma_{M_{Y_{BMC}}}\right)^2 + {\sigma_{F_A}}^2 (\Delta y)^2 + {\sigma_{F_S}}^2 (\Delta x)^2 \end{aligned} \tag{5.21}$$

Once this is complete, the rotations shown in Equation 5.22 can be used to calculate the forces and moments in the wind axis frame as shown in Figure 3. These rotations are easier to calculate before the forces and moments are put into coefficient form. If done after, reference lengths that are used to make the data non-dimensional would also appear in these equations. Note that the lift and drag forces are defined in the opposite direction from the forces along the x and z axes of the wind frame.

$$\begin{aligned}
F_x &= -\left[F_A\cos(\alpha)+F_N\sin(\alpha)\right]\cos(\beta)+\left[F_S\right]\sin(\beta) &&= -D \\
F_y &= +\left[F_A\cos(\alpha)+F_N\sin(\alpha)\right]\sin(\beta)+\left[F_S\right]\cos(\beta) &&= +Y \\
F_z &= +\left[F_A\right]\sin(\alpha)-\left[F_N\right]\cos(\alpha) &&= -L \\
M_x &= -\left[M_R\cos(\alpha)+M_Y\sin(\alpha)\right]\cos(\beta)+\left[M_P\right]\sin(\beta) \\
M_y &= +\left[M_R\cos(\alpha)+M_Y\sin(\alpha)\right]\sin(\beta)+\left[M_P\right]\cos(\beta) \\
M_z &= +\left[M_R\right]\sin(\alpha)-\left[M_Y\right]\cos(\alpha)
\end{aligned} \tag{5.22}$$

The uncertainty added by the coordinate rotation is generally small. For most internal balance tests, neither the pitch or yaw angles will be greater than 30°. In the test data presented in this chapter, the maximum pitch angle was less than 20°. Once each individual term was determined using the error propagation equation, the uncertainty equations were able to be simplified dramatically. The term dependent on the error in the yaw angle was disregarded since the uncertainty in the angle is small. The part of the equation contingent on the uncertainty in alpha was also able to be ignored. The three terms based on the forces or moments are considered significant and must be included.

However, the part of the equation based on the force or moment that dominates the result in each equation, such as axial force for F_x, was much larger than the other two remaining terms. Since the non-dominant terms are multiplied by the sine of an angle, they were also ignored and replaced with a simpler model. It was found that

multiplying the uncertainty of the dominant term in each equation by the square root of two would increase the uncertainty by an amount large enough to safely account for the ignored force or moment terms, even at high angles of attack. As a result, Equation 5.7 was again utilized to propagate the error of each force and moment through the coordinate rotation.

The last consideration is accounting for lift-drag contamination due to misaligned flow in the test section. Assuming parallel flow, the lift and drag vectors point up and downstream, respectively. However, it has already been shown that the flow in the test section is misaligned. Equation 5.23 is a simple correction to realign the lift and drag vectors with the new direction of the free stream flow.

$$\begin{aligned} L_c &= L\cos(\Delta\alpha) - D\sin(\Delta\alpha) \\ D_c &= L\sin(\Delta\alpha) + D\cos(\Delta\alpha) \end{aligned} \tag{5.23}$$

The rotations shown below can be used to transfer the wind axis forces and moments back to the body axis. These equations are not often needed when performing an internal balance test, but can be useful in recalculating the body forces from the lift and drag during the correction process.

$$\begin{aligned} F_A &= [-F_x\cos(\beta) + F_y\sin(\beta)]\cos(\alpha) + [F_z]\sin(\alpha) \\ F_S &= [F_x]\sin(\beta) + [F_y]\cos(\beta) \\ F_N &= [-F_x\cos(\beta) + F_y\sin(\beta)]\sin(\alpha) - [F_z]\cos(\alpha) \\ M_R &= [-M_x\cos(\beta) + M_y\sin(\beta)]\cos(\alpha) + [M_z]\sin(\alpha) \\ M_P &= [M_x]\sin(\beta) + [M_y]\cos(\beta) \\ M_Y &= [-M_x\cos(\beta) + M_y\sin(\beta)]\sin(\alpha) - [M_z]\cos(\alpha) \end{aligned} \tag{5.24}$$

The last step in the data analysis is to make all of the force and moments non-dimensional. This allows the data to be compared to other test runs that were not

performed at the same testing conditions. Also, it allows for scaling of the data as desired. The equations for the both the body and wind axis coefficients are:

$$\begin{aligned} C_A &= F_A/(q_c S) & C_D &= D/(q_c S) \\ C_S &= F_S/(q_c S) & C_Y &= Y/(q_c S) \\ C_N &= F_N/(q_c S) & C_L &= L/(q_c S) \\ C_{M_R} &= M_R/(q_c S b) & C_l &= M_x/(q_c S b) \\ C_{M_P} &= M_P/(q_c S c) & C_m &= M_y/(q_c S c) \\ C_{M_Y} &= M_Y/(q_c S b) & C_n &= M_z/(q_c S b) \end{aligned} \tag{5.25}$$

In each case, the uncertainty equation can be dramatically simplified. This results in the following generalized uncertainty propagation equation:

$$\sigma_{C_i}{}^2 = C_i{}^2 \left[\left(\frac{\sigma_i}{i} \right)^2 + \left(\frac{\sigma_{q_c}}{q_c} \right)^2 \right] \tag{5.26}$$

The only two terms that add significantly to the uncertainty stem from the force or moment and the dynamic pressure. The error propagation is simplified by adding the definition for the coefficient back into each term in the equation.

J. Summary of Uncertainty Results

Data from a typical LSWT internal balance test was analyzed using the steps outlined in the previous sections of this chapter. The first item of interest was the magnitude of the uncertainty for the fully analyzed results. These numbers are shown in Table 8 for the model angles and the test section dynamic pressure. Similarly, Table 9 contains the values for the force and moment coefficients in the body and wind axis reference frames.

The uncertainty in the pitch angle was $\pm 0.24°$, which was by far the largest for any of the model orientation angles. The error in the yaw and roll angles was

Table 8: Uncertainty of the Reported Test Section and Model Parameters

Measurement	Symbol	Uncertainty
Model Alpha	α	$\pm 0.24°$
Model Beta	β	$\pm 0.05°$
Model Gamma	γ	$\pm 0.05°$
Test Section Dynamic Pressure	q_c	± 0.14 psf

Table 9: Uncertainty of the Reported Force and Moment Coefficients

Measurement	Frame	Symbol	Mark X	Mark XIII
Axial Force	Body	C_A	± 0.010	± 0.011
Side Force	Body	C_S	± 0.012	± 0.048
Normal Force	Body	C_N	± 0.013	± 0.038
Rolling Moment	Body	C_{M_R}	± 0.003	± 0.010
Pitching Moment	Body	C_{M_P}	± 0.008	± 0.029
Yawing Moment	Body	C_{M_Y}	± 0.002	± 0.011
Drag Force	Wind	C_D	± 0.014	± 0.015
Side Force	Wind	C_Y	± 0.017	± 0.068
Lift Force	Wind	C_L	± 0.018	± 0.054
Rolling Moment	Wind	C_l	± 0.004	± 0.015
Pitching Moment	Wind	C_m	± 0.012	± 0.041
Yawing Moment	Wind	C_n	± 0.002	± 0.015

only $\pm 0.05°$, while the uncertainty in the corrected test section dynamic pressure was calculated to be ± 0.14 psf.

The results in Table 9 show several notable trends. First, the uncertainty in force and moment coefficients for the Mark XIII internal balance are higher than the respective values for the Mark X balance. Secondly, the data show a trend that the moment coefficients are slightly more accurate than the force coefficients. Lastly, of

the three force coefficients for each reference frame, the axial force and drag coefficients are the most accurate. This is a logical conclusion since the axial force is the only force coefficient to be directly measured. As shown previously, the drag force in the wind axis consists mainly of the axial force component in the body axis.

The second item of interest was to determine what part of the analysis process provided the main portion of uncertainty for each coefficient. In order to accomplish this, the uncertainty of the forces and moments at each step in the procedure was made to be non-dimensional. Then, the difference in the results from one step to the next was calculated and divided by the final uncertainty of the coefficient. This yielded both a difference in the uncertainty and a percent increase as a function of the overall error for each parameter through each step of the test and analysis. This data can be found in Tables 10 and 11 for all the tunnel parameters and body axis coefficients. Note that this was not completed for the wind axis coefficients since they were not calculated until the end of the process.

Table 10: Summary of the Uncertain Analysis for the Model Parameters

Analysis Step	σ_α	σ_β	σ_γ	σ_{q_c}
Instrument Data Acquisition	$\pm 0.02^\circ$	$\pm 0.05^\circ$	$\pm 0.05^\circ$	± 0.02 psf
	15.63%	99.91%	99.45%	14.81%
Sting Deflections	$\pm 0.00^\circ$	$\pm 0.00^\circ$	$\pm 0.00^\circ$	
	0.00%	0.09%	0.55%	
Flow Angularity	$\pm 0.12^\circ$	$\pm 0.00^\circ$		
	50.00%	0.00%		
Blockage Corrections				± 0.12 psf
				85.19%
Additional Corrections	$\pm 0.10^\circ$			
	41.67%			

The uncertainty contribution breakdown in Table 10 contains multiple noteworthy results. The first is that the main portion of error for both the yaw and roll angles is contributed by the original setup and measurement processes. This is not the case for the pitch angle where the majority of the uncertainty is incorporated during the correction phase. Similarly, the majority of the uncertainty in the final test section dynamic pressure was introduced during the blockage corrections.

The force and moment coefficient data in Table 11 also shows several interesting trends. All of the force coefficients had at least a third of their uncertainty introduced by the data acquisition step. The uncertainties of the moment coefficients were less dependent on the data acquisition. However, with the exception of the yawing moment, they were still strongly influenced by this part of the process. The force and moment calculation instituted a large portion of the error for both the pitching moment and yawing moment. There was a significant growth in the uncertainty in the normal and side force coefficient as well. Note that the increase was larger for the normal force coefficient as its initial uncertainty was higher for the Mark X balance.

The point by point static tare introduced an even increase in the uncertainty for all of the coefficients. This increase is a percentage based on the overall uncertainty while assuming a point by point tare is being used in the data analysis process. Note that the percentage values of each coefficient for the other steps include the curve fit static tare data and exclude the point by point tare data. These percentages would be different if based on the point by point tare.

The curve fit tare introduced a larger increase in the error for all of the variables except the normal force and pitching moment. These two coefficients, used to determine the static tare fit, actually experienced a drastic decrease in the uncertainty initiated into the process during this step.

Table 11: Summary of the Uncertain Analysis for an Internal Balance Test

Analysis Step	σ_{C_A}	σ_{C_S}	σ_{C_N}	$\sigma_{C_{M_R}}$	$\sigma_{C_{M_P}}$	$\sigma_{C_{M_Y}}$
Instrument Data Acquisition	±0.0058	±0.0042	±0.0083	±0.0013	±0.0020	±0.0002
	58.98%	35.33%	65.59%	49.74%	23.74%	11.28%
Force & Moment Calculation		±0.0018	±0.0035		±0.0040	±0.0005
		14.63%	27.17%		47.60%	30.60%
Static Tare (Pointwise)	±0.0024	±0.0025	±0.0049	±0.0005	±0.0025	±0.0003
	29.07%	29.26%	27.86%	29.08%	22.86%	22.98%
Static Tare (Curve Fit)	±0.0039	±0.0060	±0.0001	±0.0013	±0.0000	±0.0006
	40.38%	49.96%	0.50%	49.74%	0.25%	41.88%
Cavity Pressure Correction			±0.0002			
			1.27%			
Additional Corrections	±0.0000		±0.0001		±0.0006	
	0.31%		0.56%		7.06%	
Coordinate Transformation				±0.0000	±0.0017	±0.0002
				0.38%	20.38%	16.12%
Non-Dimensionalization	±0.0000	±0.0000	±0.0006	±0.0000	±0.0001	±0.0000
	0.33%	0.08%	4.92%	0.13%	0.97%	0.13%

The reason this did not hold true for the axial force is that the static tare measurements for the axial force are larger in magnitude. As shown in Equation 5.9, this makes the uncertainty in the axial force more dependent on the error in the pitch angle, thereby creating a larger increase in the uncertainty of the axial force. The side force, rolling moment, and yawing moment are not being fit and therefore the error is much larger since they are assumed zero instead of using the point-by-point subtraction method. In the future, determining model fit equations for these parameters would decrease the uncertainty.

The two correction steps did little to cause the error in the coefficients to become larger. The only exception was the increase in the uncertainty of the pitching moment coefficient due to the streamline curvature correction. The same is true of the transformation and non-dimensionalization steps in the analysis process. The only significant growth in uncertainty were in the pitching and yawing moment coefficients during the transformation step and the normal force coefficient when it was made to be non-dimensional.

CHAPTER VI

CONCLUSIONS AND RECOMMENDATIONS

The goal of this thesis is to improve: efficiency and consistency in internal balance setup and testing and provide a record of data uncertainty and limitations. Both of these will lead to higher quality results. Three tasks were outlined in Chapter I in order to achieve the goal of this thesis.

The first task was to produce standardized documentation for an internal balance test at the LSWT. This was partially achieved in Chapter II by recording detailed information about the LSWT. The important results in this chapter detail the limitations of the test equipment and internal balances owned by the LSWT. This information is crucial in properly designing and sizing a wind tunnel test. An example is shown in Chapter VI as the Mark X internal balance uncertainty limitations were significantly less than the larger Mark XIII balance.

The second part of this task was completed in Chapter III through flow uniformity and turbulence intensity testing. It was displayed that the flow uniformity of the empty test section was excellent. With HARS installed in the test section, the flow uniformity declined, but was still acceptable in the region of the model. Yawing the HARS mount decreased the quality of the flow uniformity while pitching HARS had the opposite effect. The turbulence intensity in the test section was shown to be a function of both the test section dynamic pressure and motor RPM. However, the turbulence intensity magnitude was generally less than or equal to 0.25%.

The second task was to become more accurate and efficient in executing internal balance tests. This was realized in Chapter IV by creating documentation of an internal balance test at the LSWT. The use of checklists for HARS installation,

internal balance installation, sting deflections, and an overview of testing procedures has helped decrease setup time and increase operational dependability.

The third and final task was to completely reduce the tunnel output data and perform an uncertainty analysis on the reduction routine. This was completed in Chapter V by outlining a step by step data routine with an accompanying uncertain examination for each stage. The results of the uncertainty analysis can be seen in Tables 8 and 9. Higher quality results were achieved by quantifying the error of the primary output parameters and showing repeatability of the results within the defined uncertainty limits. The repeatability of the results are shown in Figure 107 through Figure 112. The average difference between corresponding data points was less than the defined uncertainty limits for each coefficient.

A step by step analysis of the uncertainty routines was used to reveal which phases had the greatest effect on the final uncertainty values. For the pitch angle, this occurred during the additional corrections step, while the error in the dynamic pressure stemmed from the blockage corrections. In light of the results and conclusions of this thesis, there are several recommendations to be considered in the future.

First, a multi-hole probe should be used to create flow angularity maps of the test section with and without the HARS mount. This would provide a better understanding of how the introduction of HARS into the test section affects the flow quality before the installation of the model. Secondly, renovations should be made to the HARS mount stand and testing room to allow for better organization. All equipment associated with an internal balance test should have a designated storage space on the HARS mount stand. This would increase setup efficiency in conjunction with the checklists provided in this thesis.

For the force and moment coefficients, the majority of the uncertainty was introduced by the data acquisition and static tare steps. A precise calibration stand

should be designed and built for the Mark X and Mark XIII internal balances. This stand could be used periodically to determine the validity of the internal balance calibrations in a more accurate manner. This could help reveal any instrumental error introduced by the internal balances and decrease the overall uncertainty in the data acquisition phase of the procedure. Last, a study to find an appropriate method for fitting the remaining force and moments during the static tare would help decrease the uncertainty added into the process during this step.

REFERENCES

[1] van Doorninck, C. I., "Gilchrist, Gibb," November 2012. Retrieved from http://www.tshaonline.org/handbook/online/articles/fgi14

[2] "History," November 2012. Retrieved from http://www.easterwoodairport.com/hist.html

[3] "History of the Office," November 2012. Retrieved from http://president.tamu.edu/about/history-of-the-office/index.html

[4] Iglesias, E., "Oran W. Nicks - Remembered by the Soaring Club of Houston," November 1998. Retrieved from http://www.ssa.org/myhome.asp?mbr =5811273455&show=blog&id=675&archive=11/1/1998

[5] "Calibration and Use of Internal Strain-Gage Balances with Application to Wind Tunnel Testing," Tech. Rep. R-091-2003, American Institute of Aeronautics and Astronautics, 2003.

[6] White, E. B., *Breakdown of Crossflow Voritces*, Ph.D. dissertation, Arizona State University, 2000.

[7] Walker, I. R., *Reliability in Scientific Research: Improving the Dependability of Measurements, Calculations, Equipment, and Software*, Cambridge University Press, Cambridge, U.K., 2011.

[8] Bevington, P. and Robinson, D. K., *Data Reduction and Error Analysis for the Physical Sciences*, McGraw-Hill Companies, Boston, MA, 1992.

[9] Barlow, J. B., Rae Jr., W. H., and Pope, A., *Low-Speed Wind Tunnel Testing*, Wiley & Sons, 1999.

APPENDIX A

FIGURES OF THE LOW SPEED WIND TUNNEL FACILITY

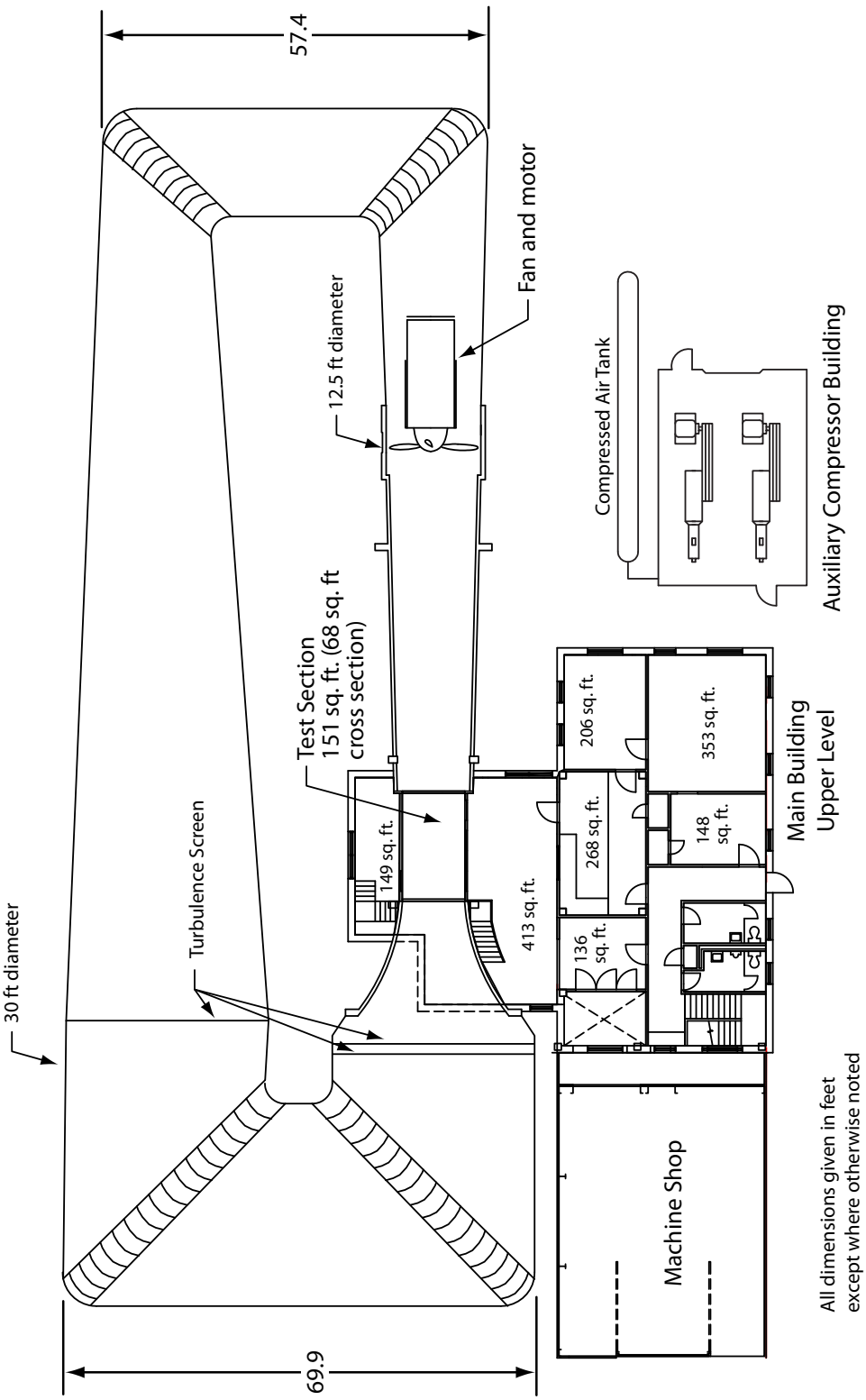

Fig. 4: Schematic of the Texas A&M Low Speed Wind Tunnel facility.

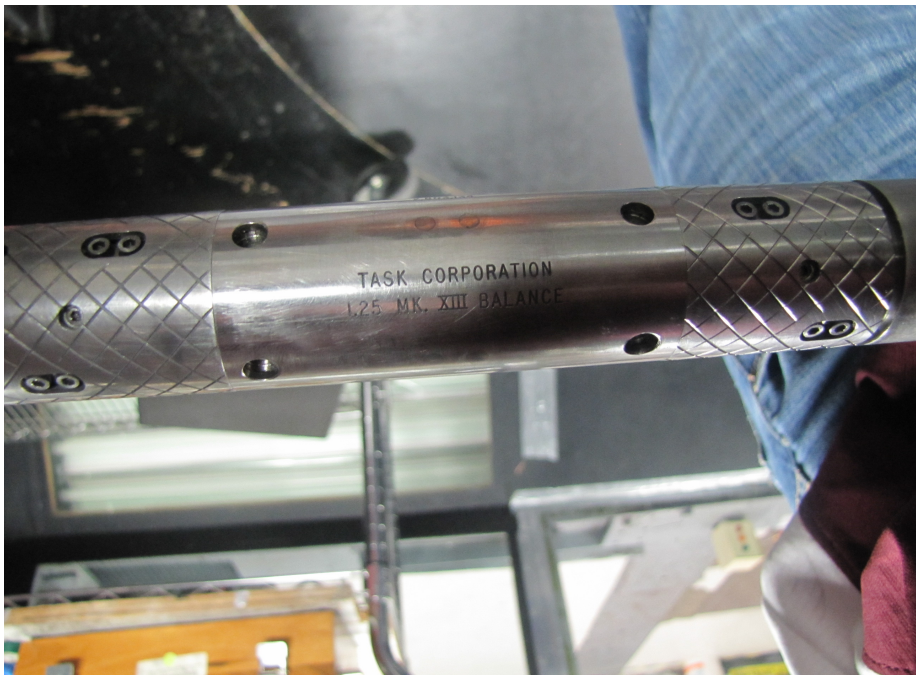

Fig. 5: The Mark XIII internal balance.

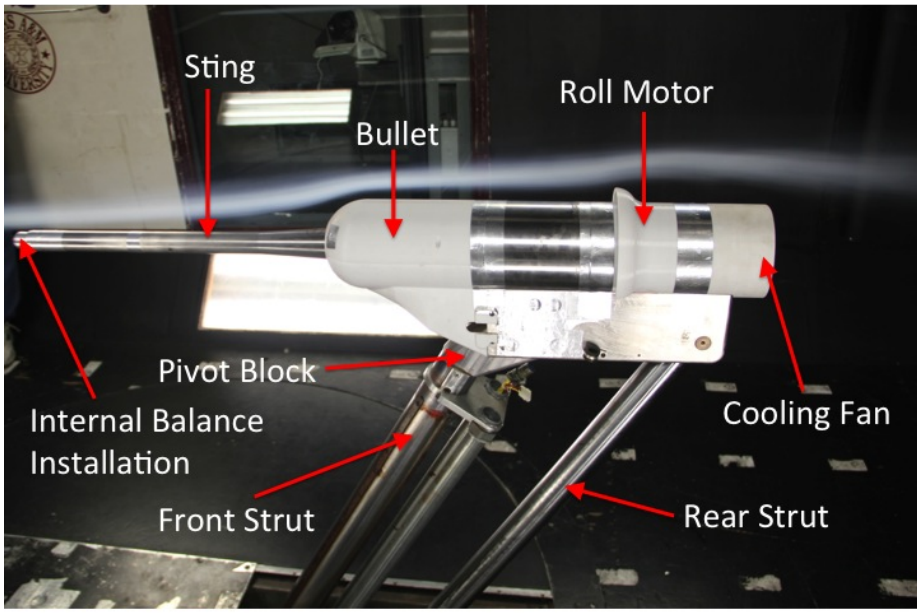

Fig. 6: The HARS unit during smoke flow visualization.

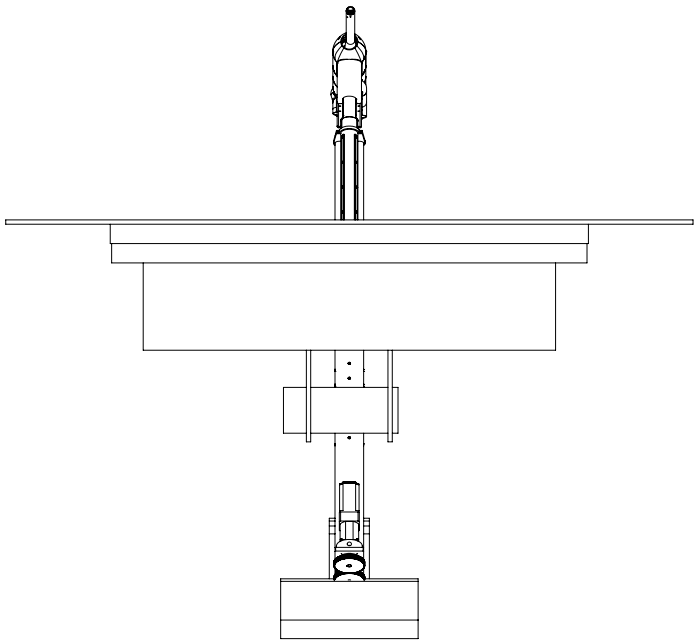

Fig. 7: Front view of the HARS mount.

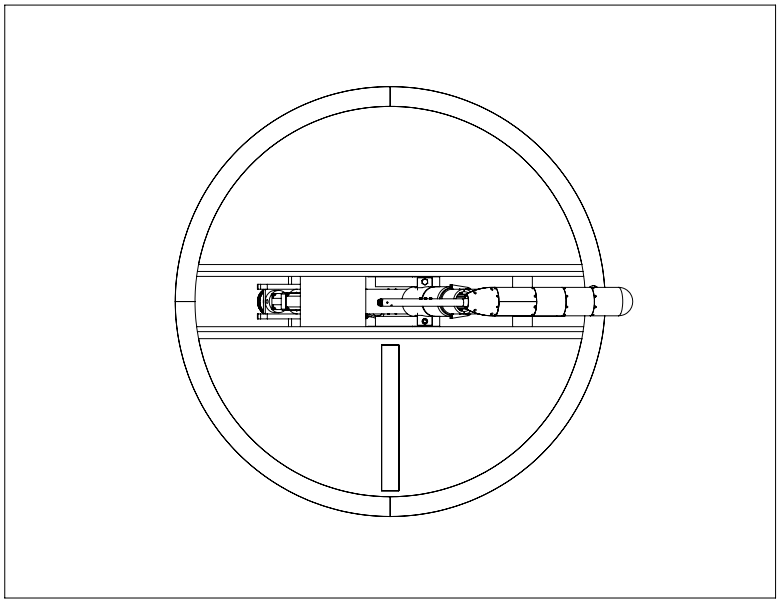

Fig. 8: Top view of the HARS mount.

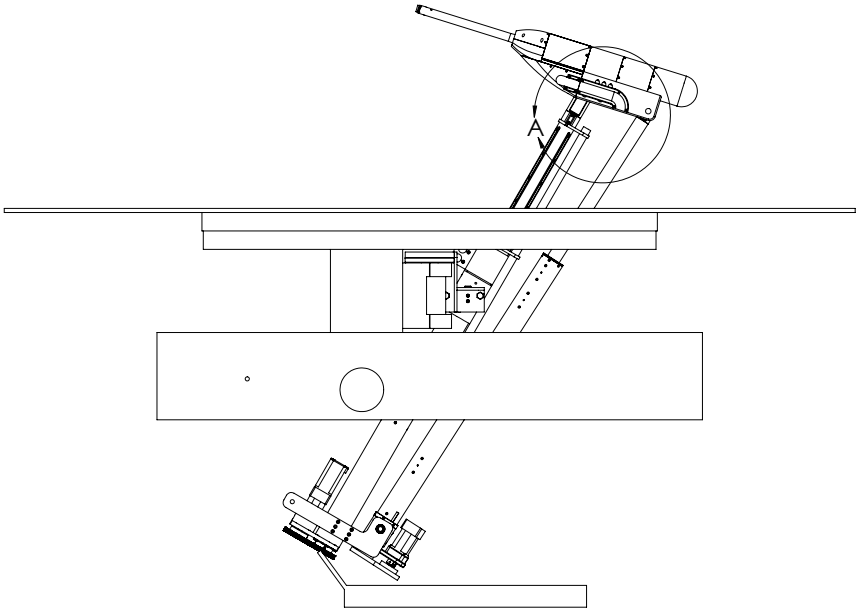

Fig. 9: Side view of the HARS mount with the normal block installed.

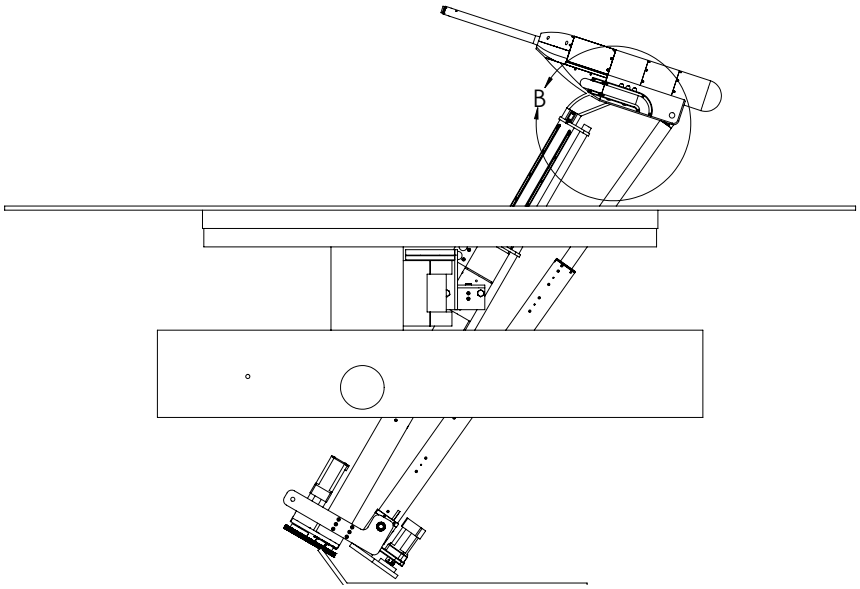

Fig. 10: Side view of the HARS mount with the 90 degree block installed.

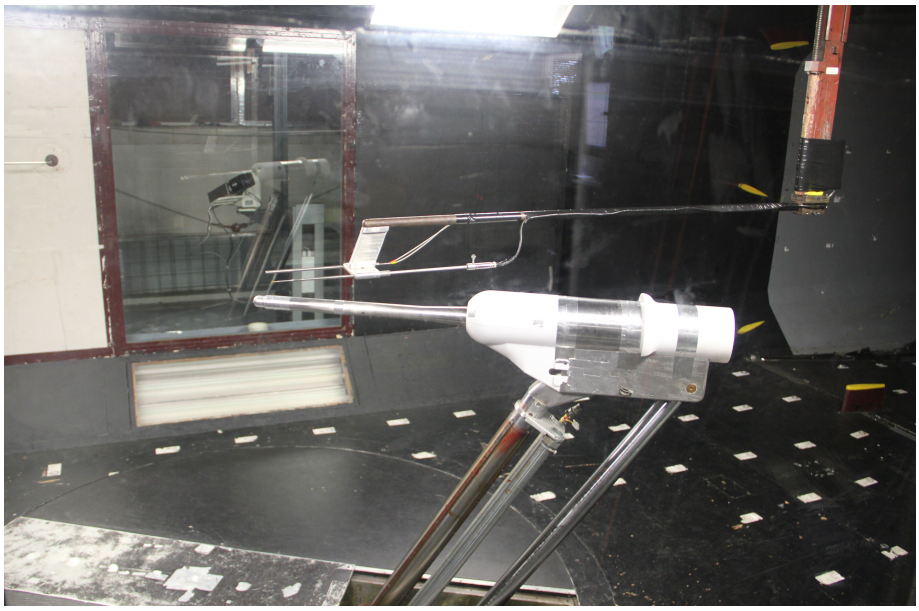

Fig. 11: The traversing mechanism and extension arm installed in the tunnel.

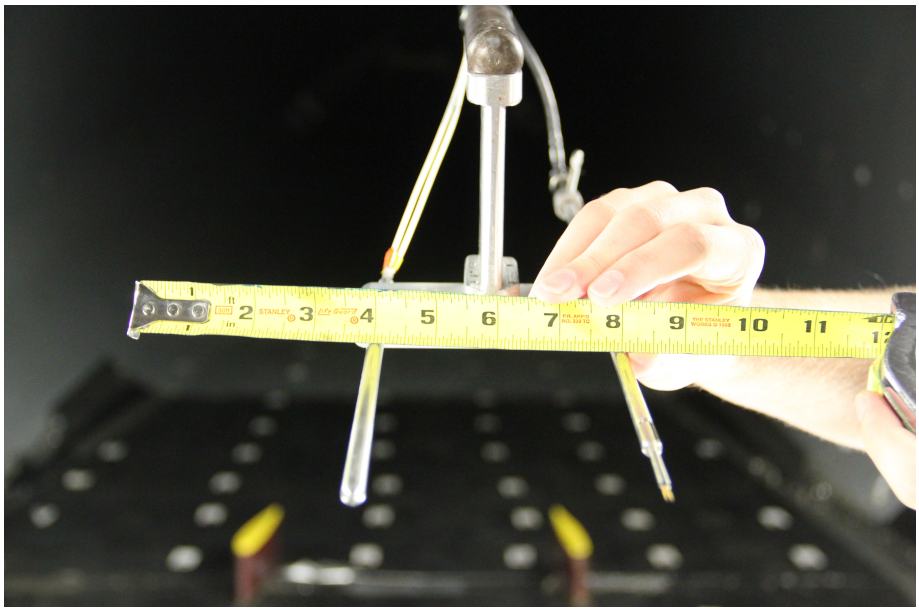

Fig. 12: The Pitot tube and hotwire mounted at the end of the extension arm.

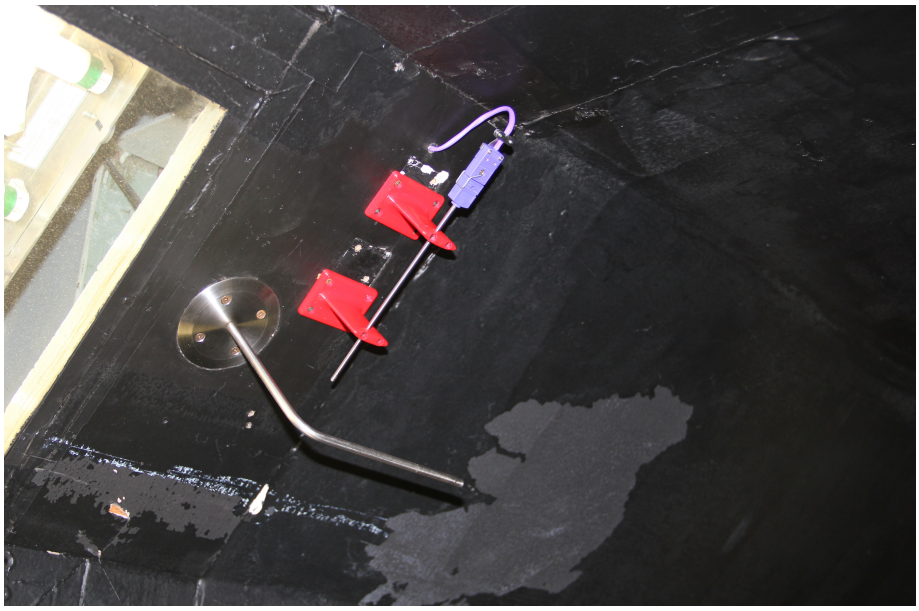

Fig. 13: The thermocouple mounted on the wall to measure test section temperature.

Fig. 14: Ball cover used to keep flow from entering the sting.

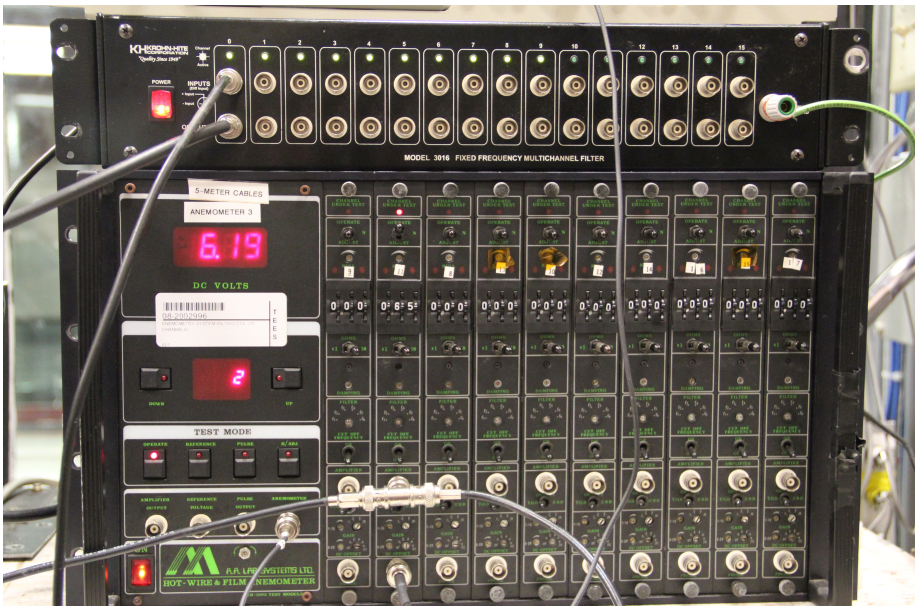

Fig. 15: The constant temperature hotwire anemometer.

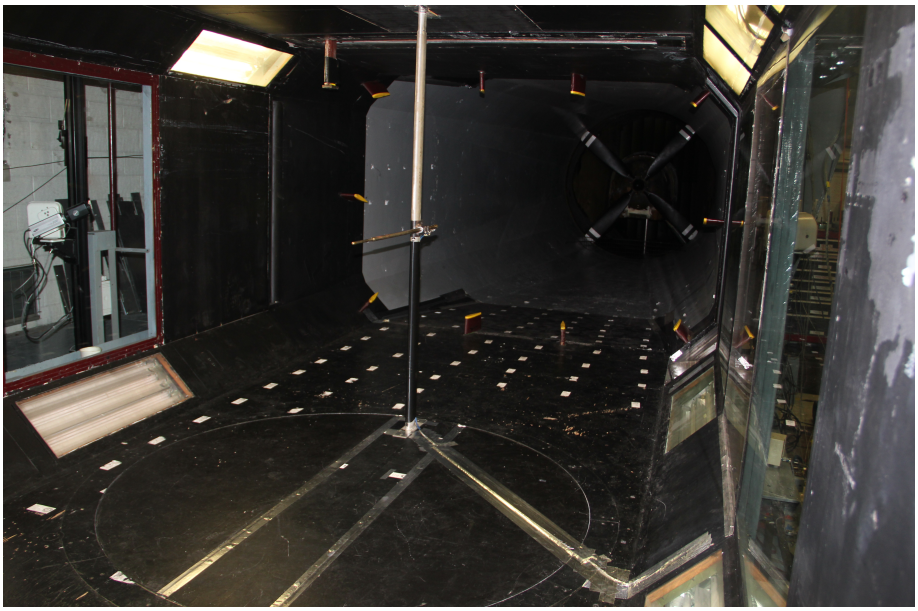

Fig. 16: The test section dynamic pressure calibration setup.

APPENDIX B

HOTWIRE CALIBRATION METHODOLOGY

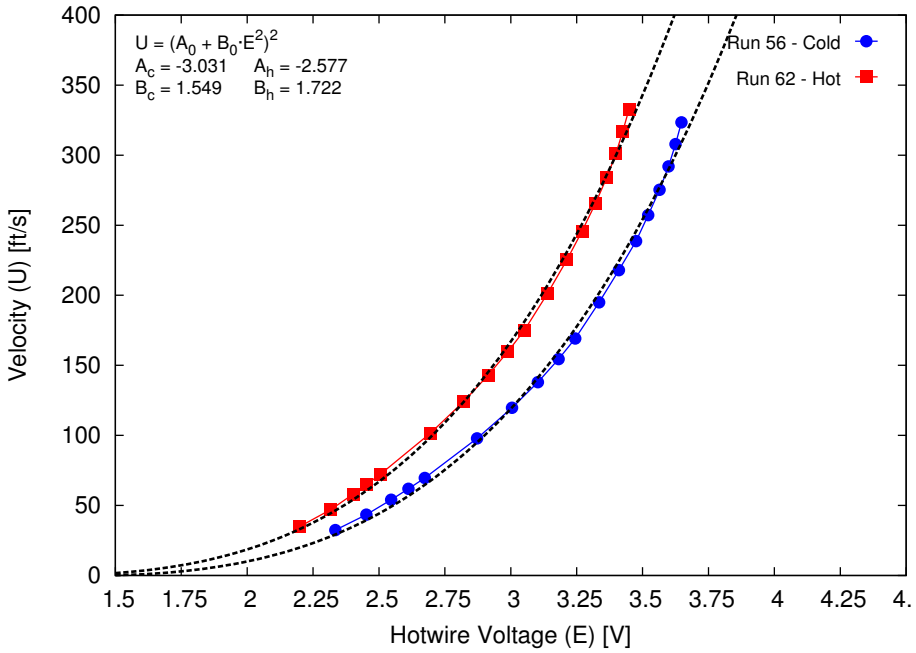

Fig. 17: Hot and cold calibration data for the hotwire with associated curve fits.

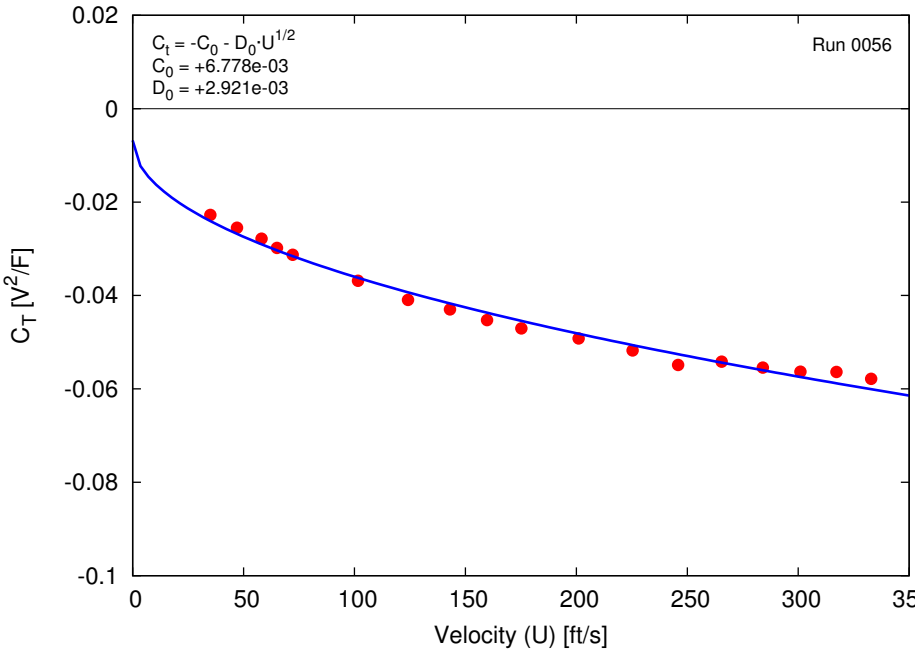

Fig. 18: Thermal correction coefficient and curve fit.

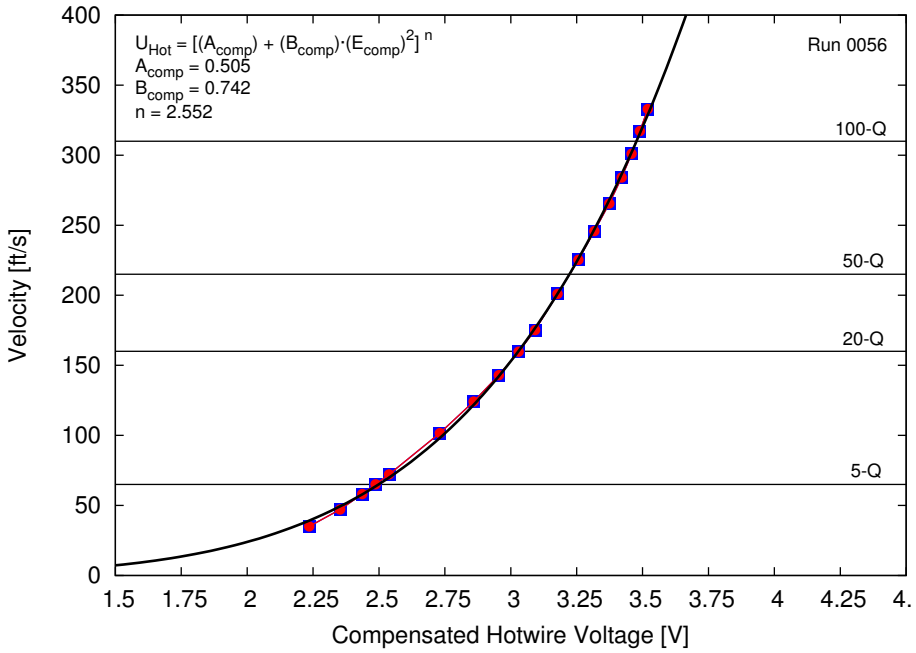

Fig. 19: Temperature compensated hot-wire data and curve fit calibration.

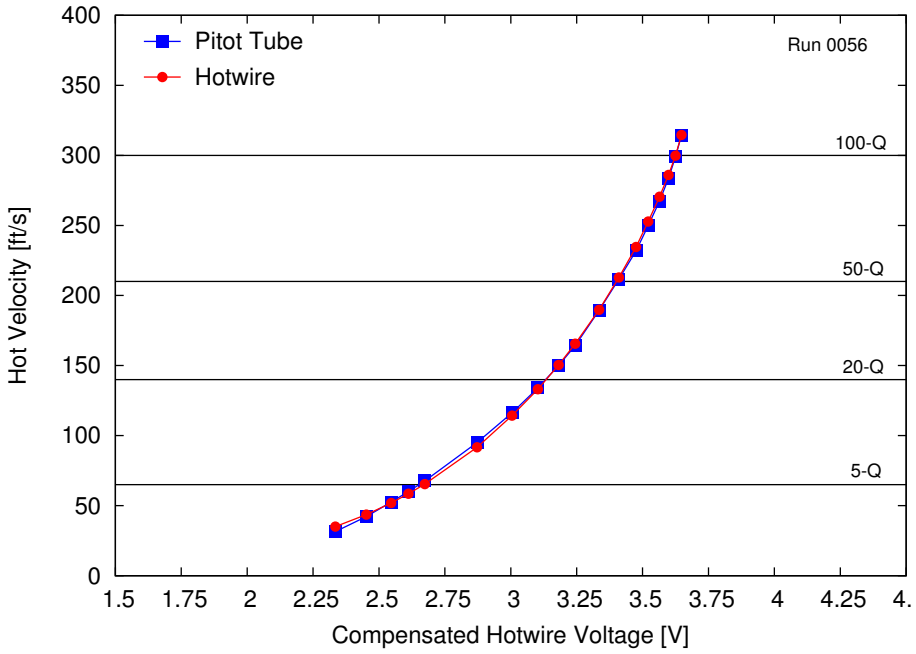

Fig. 20: Calibration check data from hot and cold hotwire runs.

APPENDIX C

FLOW CHARACTERIZATION PLOT DATABASE

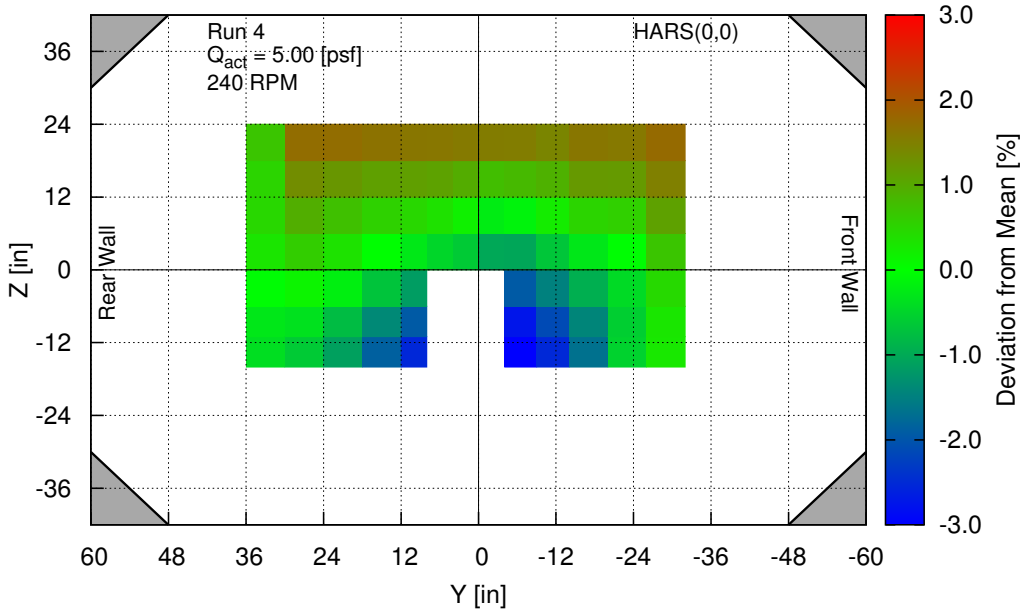

Fig. 21: Dynamic pressure variation at q_a of 5 [psf], 240 RPM, Test 1227.004.

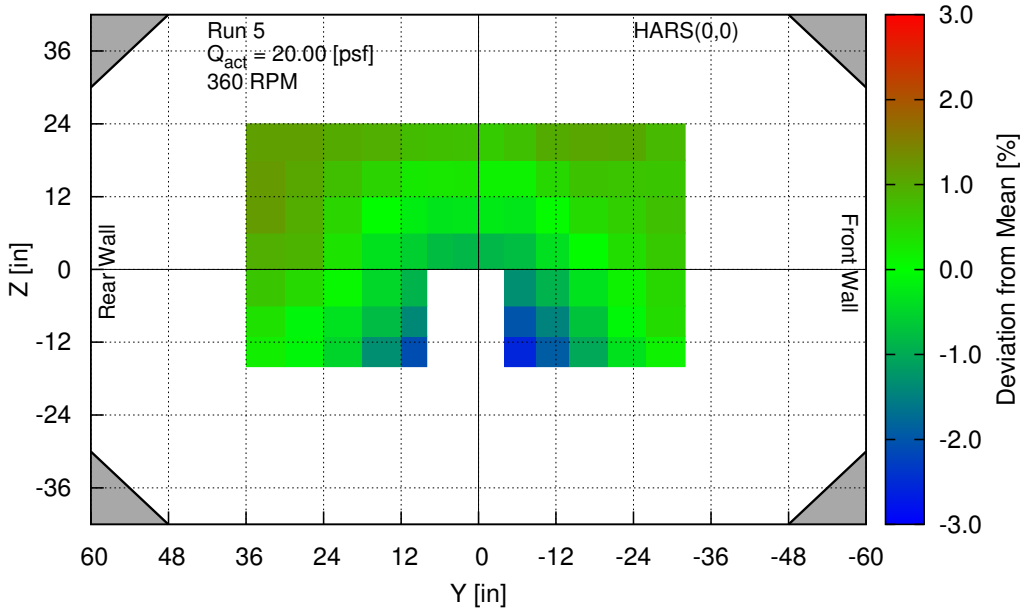

Fig. 22: Dynamic pressure variation at q_a of 20 [psf], 360 RPM, Test 1227.005.

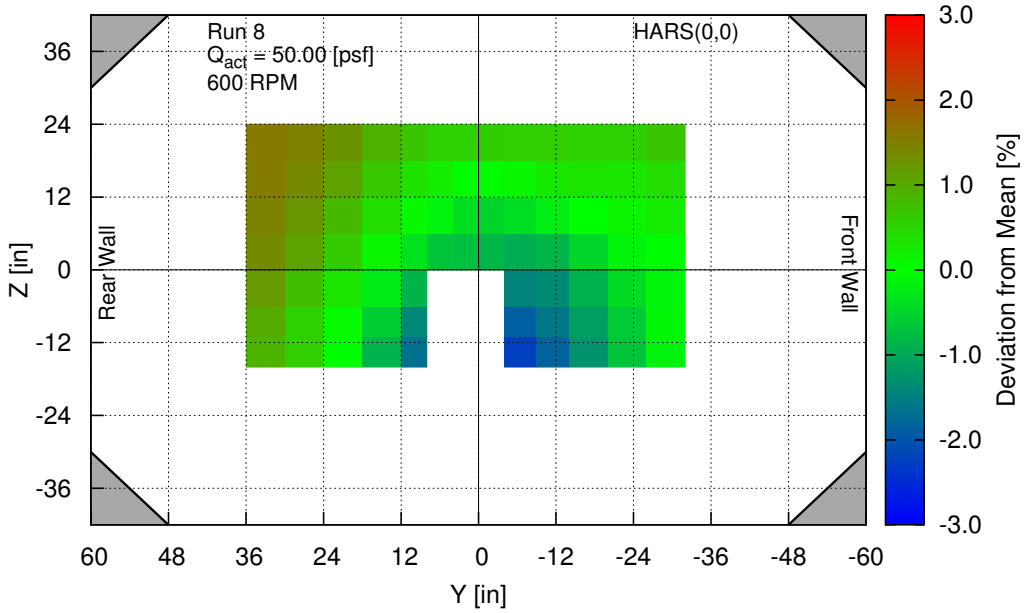

Fig. 23: Dynamic pressure variation at q_a of 50 [psf], 600 RPM, Test 1227.008.

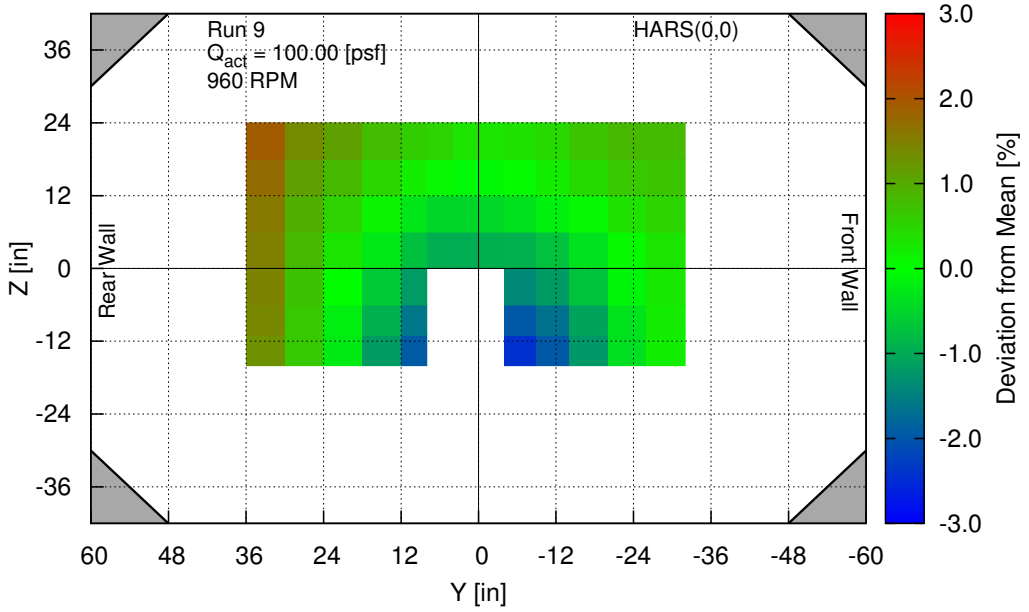

Fig. 24: Dynamic pressure variation at q_a of 100 [psf], 960 RPM, Test 1227.009.

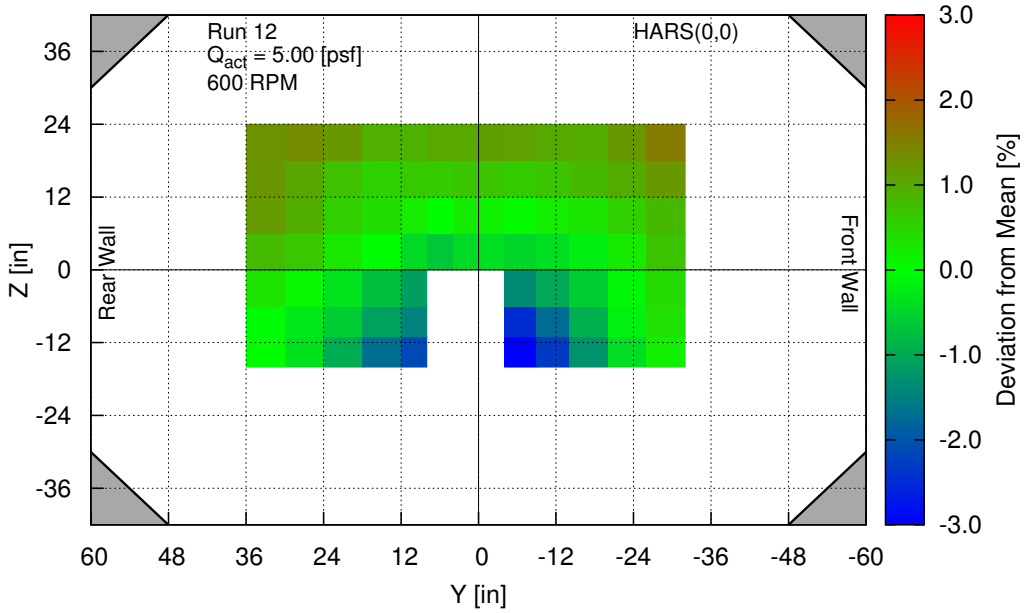

Fig. 25: Dynamic pressure variation at q_a of 5 [psf], 600 RPM, Test 1227.012.

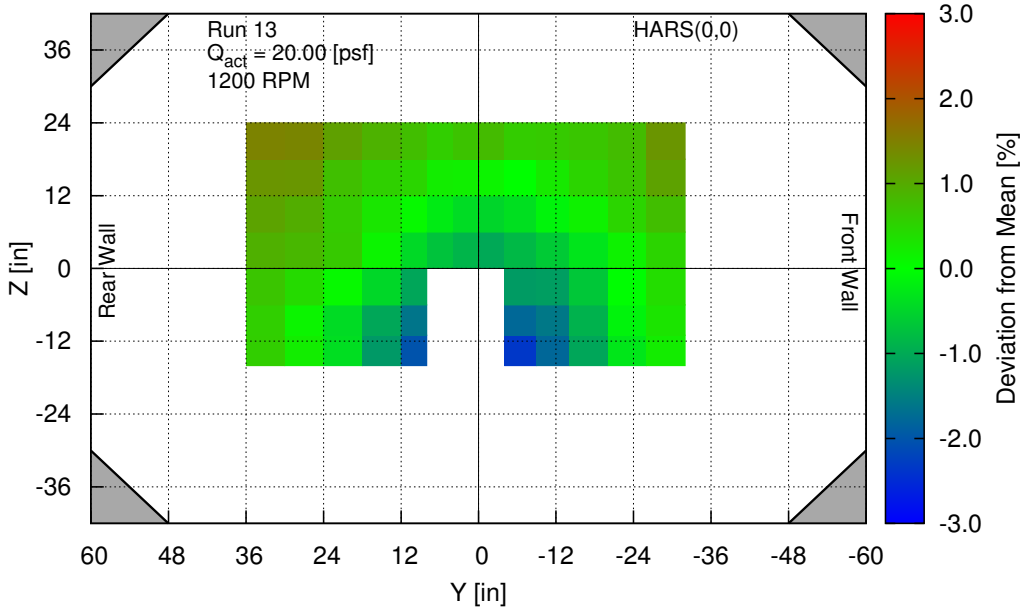

Fig. 26: Dynamic pressure variation at q_a of 20 [psf], 1200 RPM, Test 1227.013.

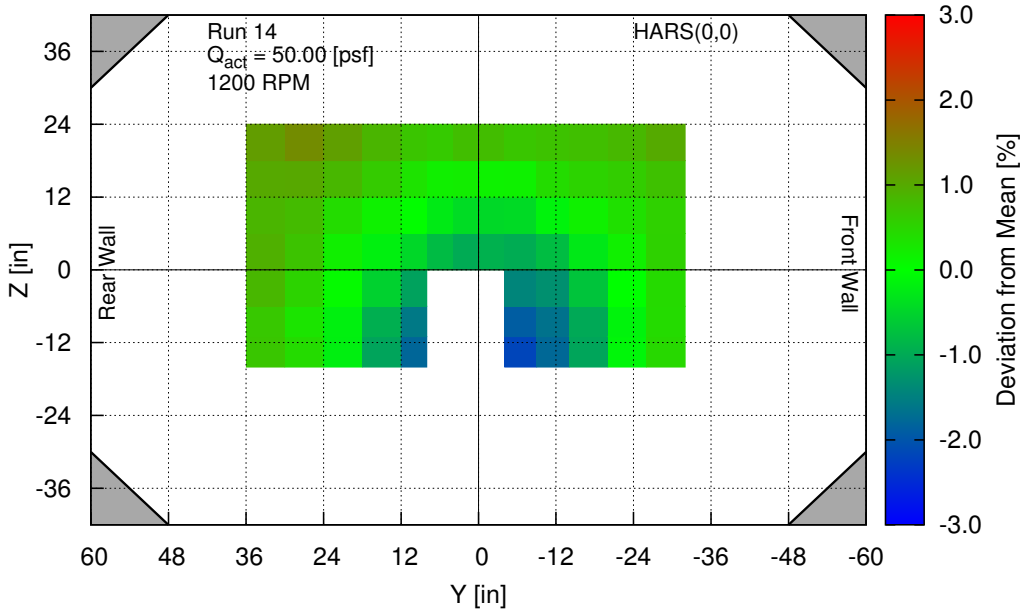

Fig. 27: Dynamic pressure variation at q_a of 50 [psf], 12000 RPM, Test 1227.014.

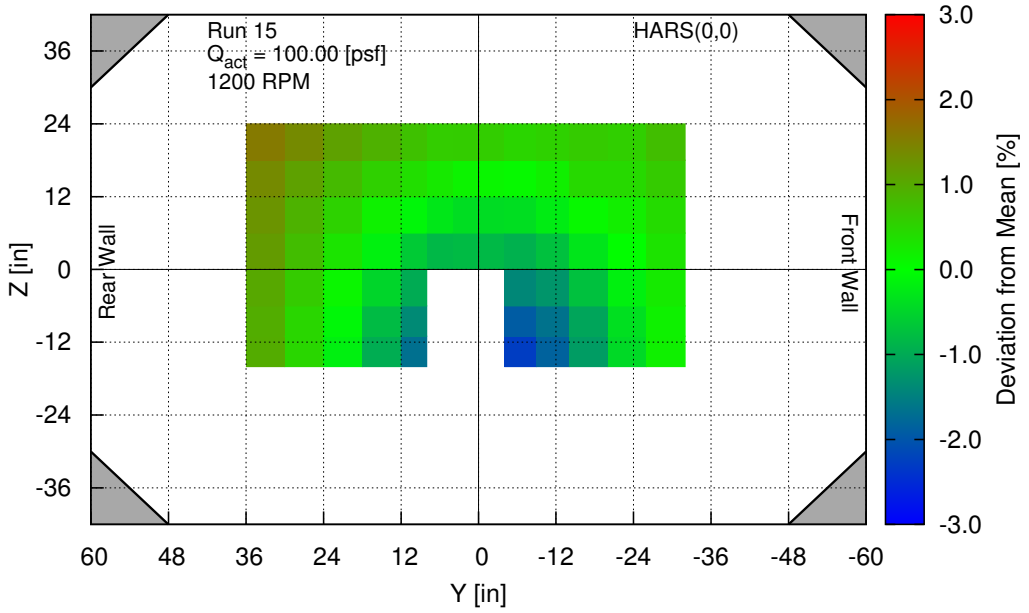

Fig. 28: Dynamic pressure variation at q_a of 100 [psf], 1200 RPM, Test 1227.015.

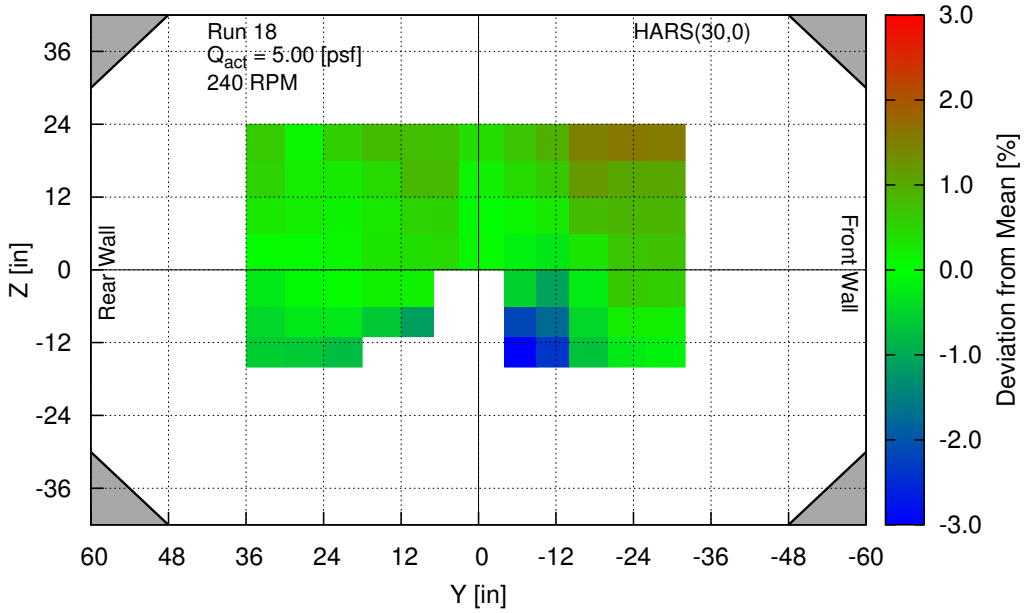

Fig. 29: Dynamic pressure variation at q_a of 5 [psf], 240 RPM, Test 1227.018.

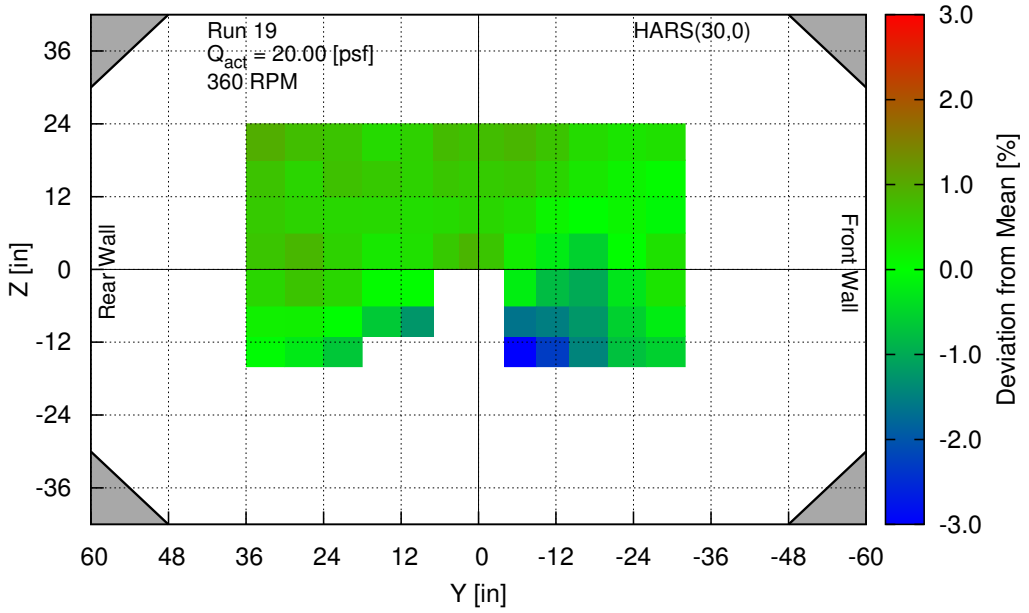

Fig. 30: Dynamic pressure variation at q_a of 20 [psf], 360 RPM, Test 1227.019.

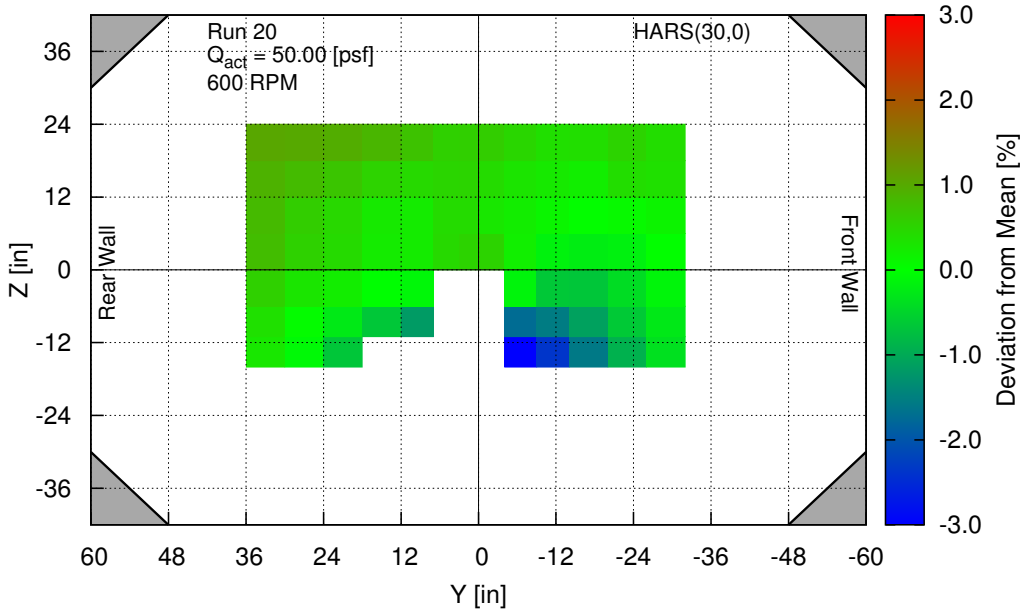

Fig. 31: Dynamic pressure variation at q_a of 50 [psf], 600 RPM, Test 1227.020.

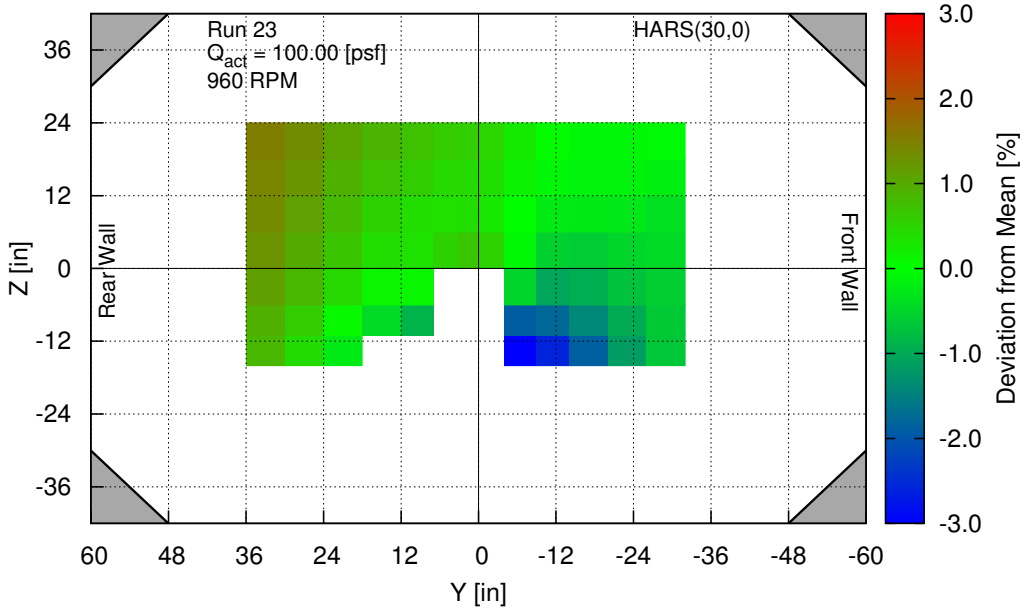

Fig. 32: Dynamic pressure variation at q_a of 100 [psf], 960 RPM, Test 1227.023.

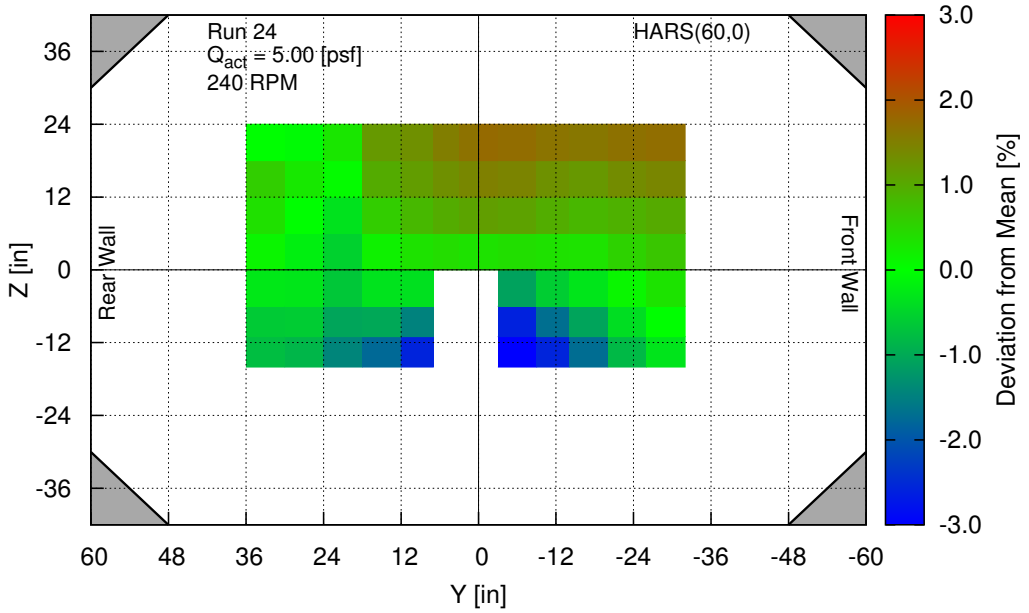

Fig. 33: Dynamic pressure variation at q_a of 5 [psf], 240 RPM, Test 1227.024.

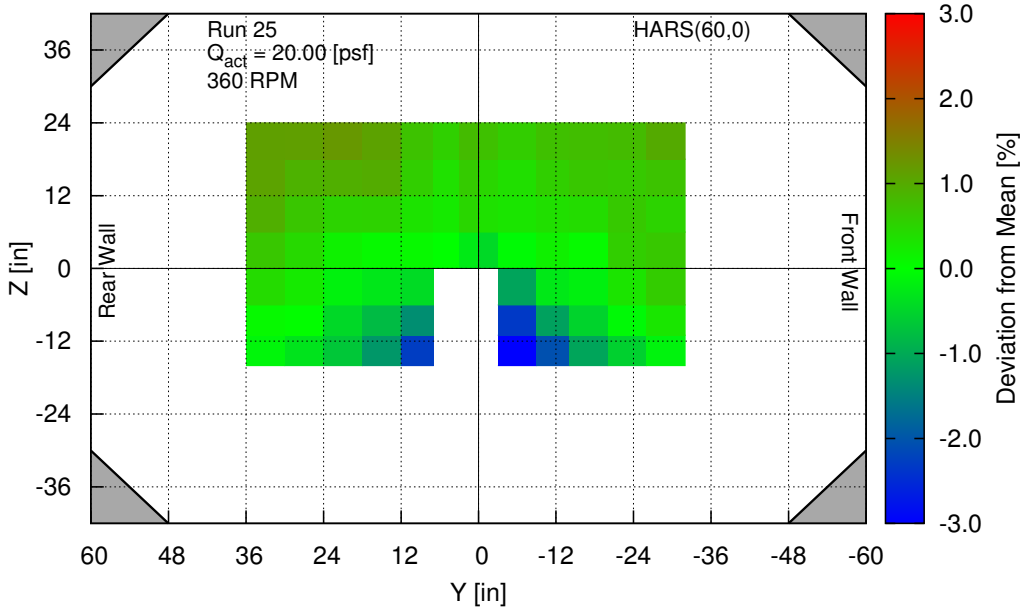

Fig. 34: Dynamic pressure variation at q_a of 20 [psf], 360 RPM, Test 1227.025.

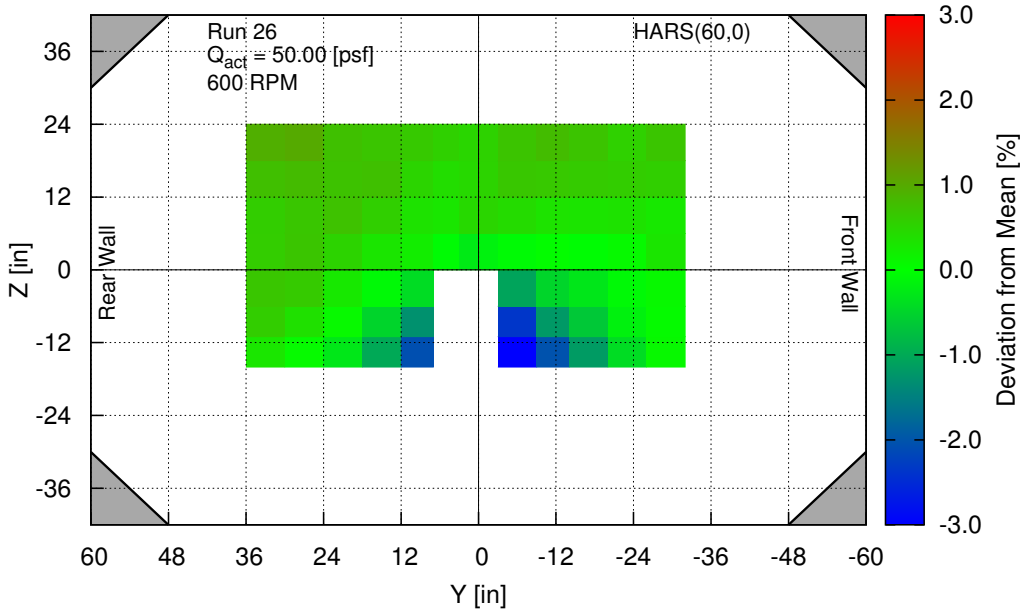

Fig. 35: Dynamic pressure variation at q_a of 50 [psf], 600 RPM, Test 1227.026.

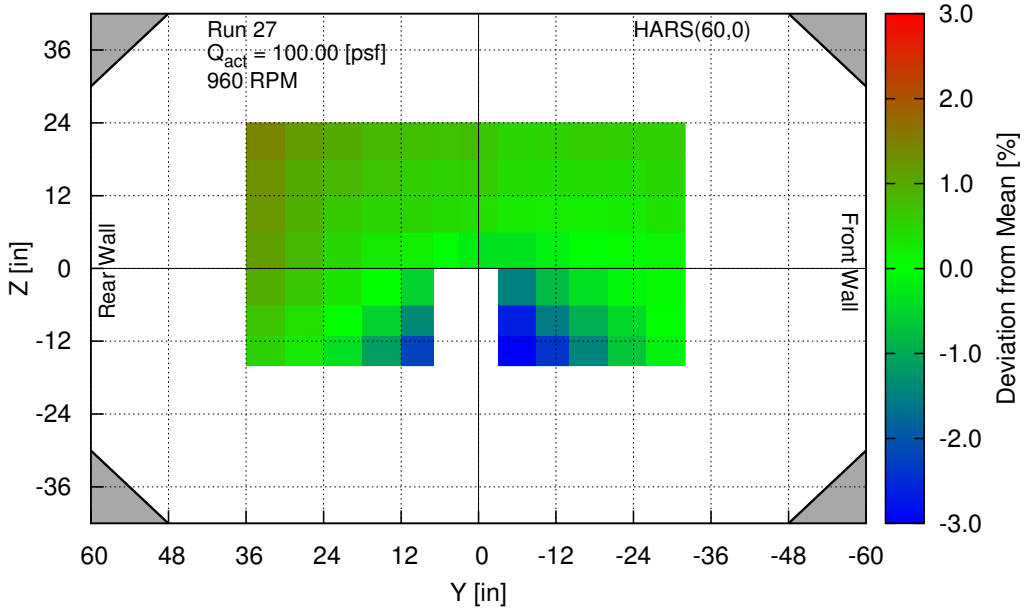

Fig. 36: Dynamic pressure variation at q_a of 100 [psf], 960 RPM, Test 1227.027.

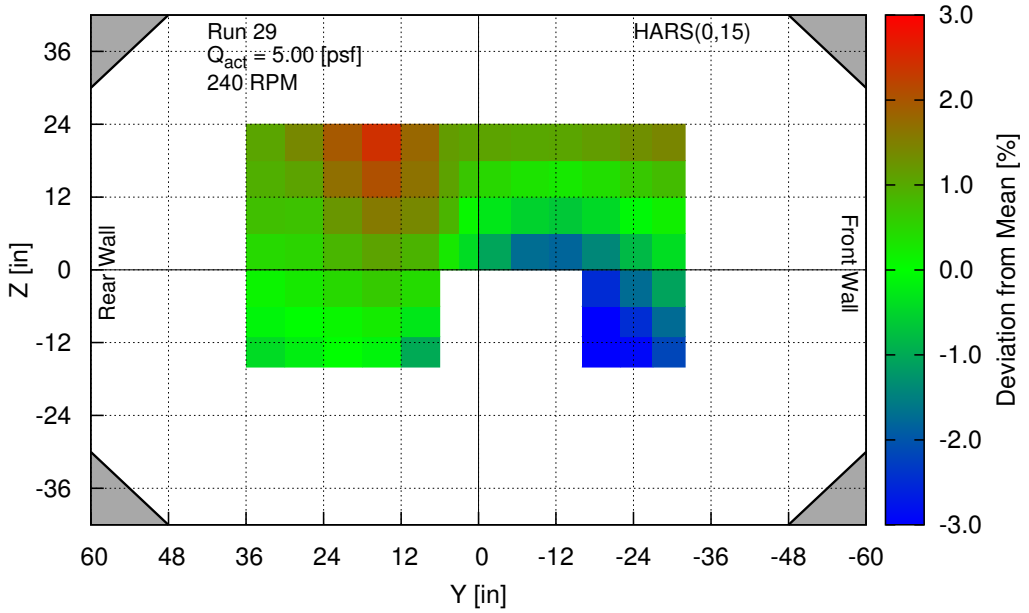

Fig. 37: Dynamic pressure variation at q_a of 5 [psf], 240 RPM, Test 1227.029.

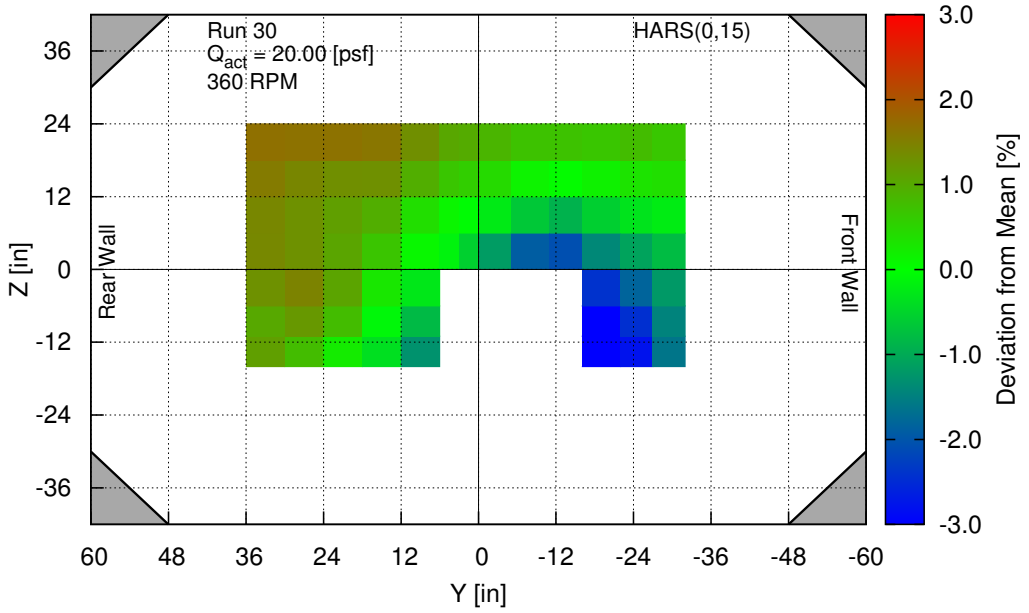

Fig. 38: Dynamic pressure variation at q_a of 20 [psf], 360 RPM, Test 1227.030.

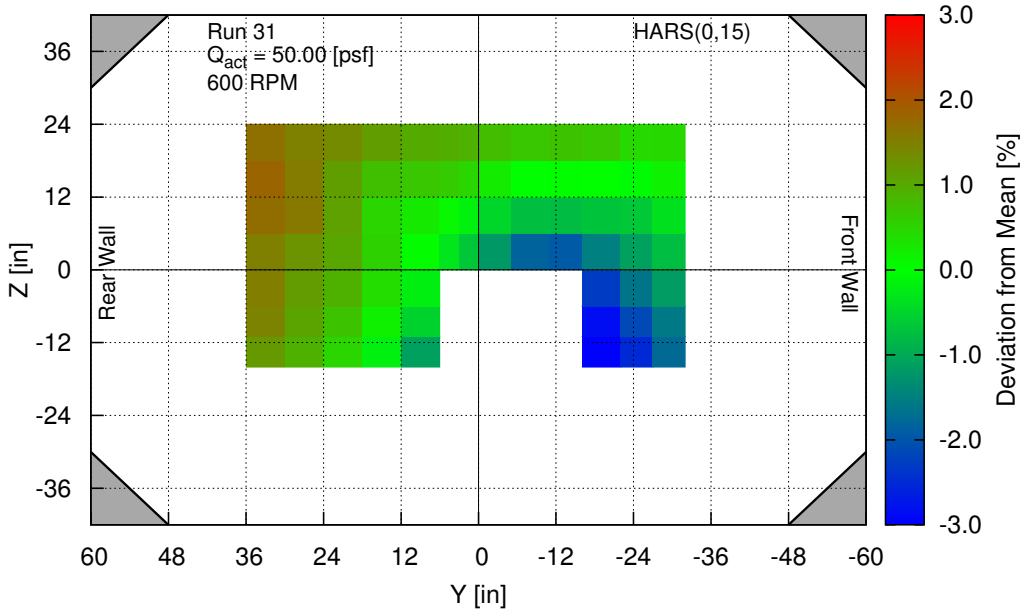

Fig. 39: Dynamic pressure variation at q_a of 50 [psf], 600 RPM, Test 1227.031.

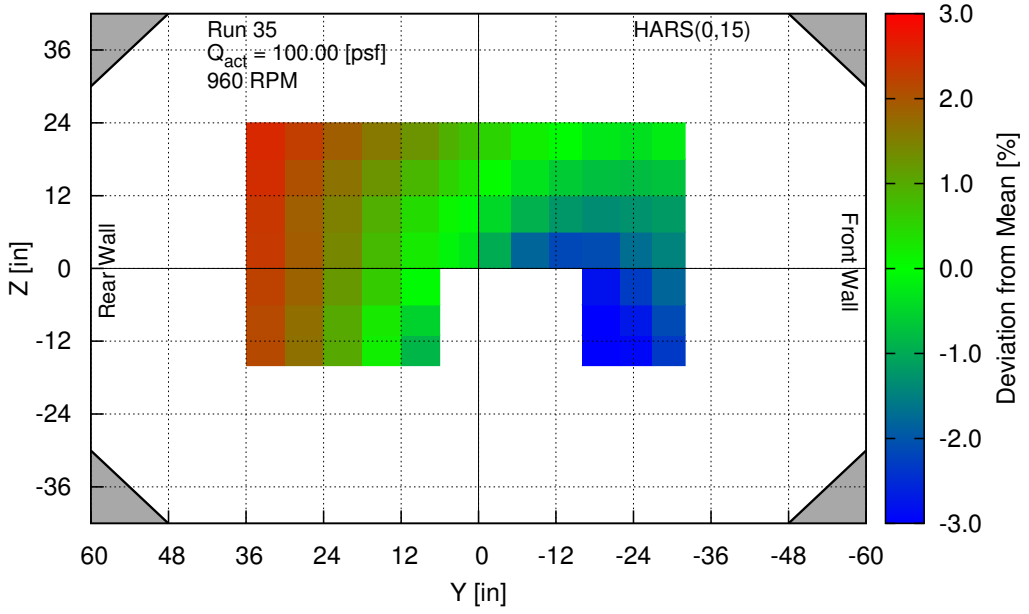

Fig. 40: Dynamic pressure variation at q_a of 100 [psf], 960 RPM, Test 1227.035.

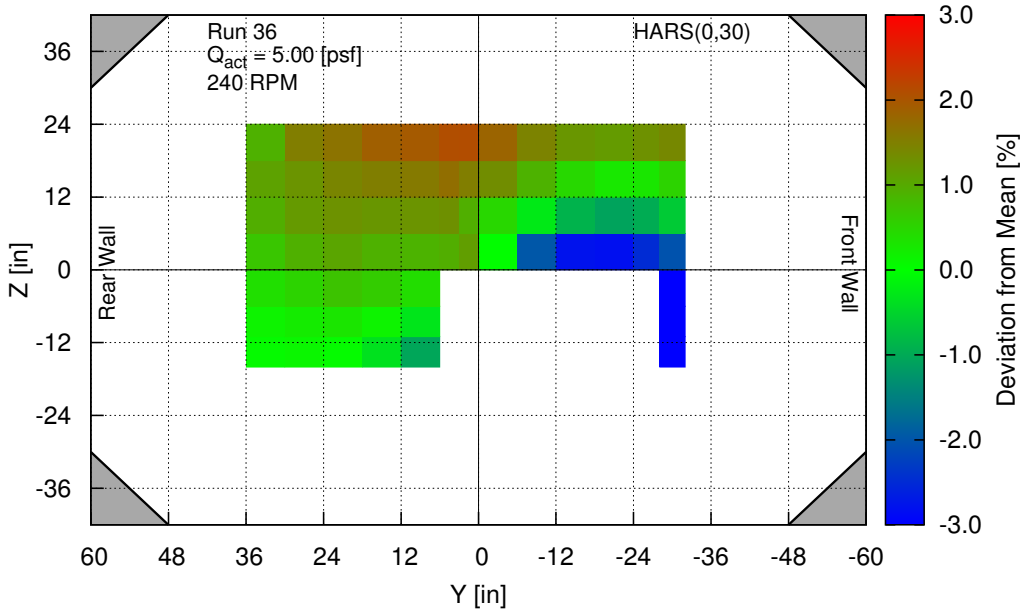

Fig. 41: Dynamic pressure variation at q_a of 5 [psf], 240 RPM, Test 1227.036.

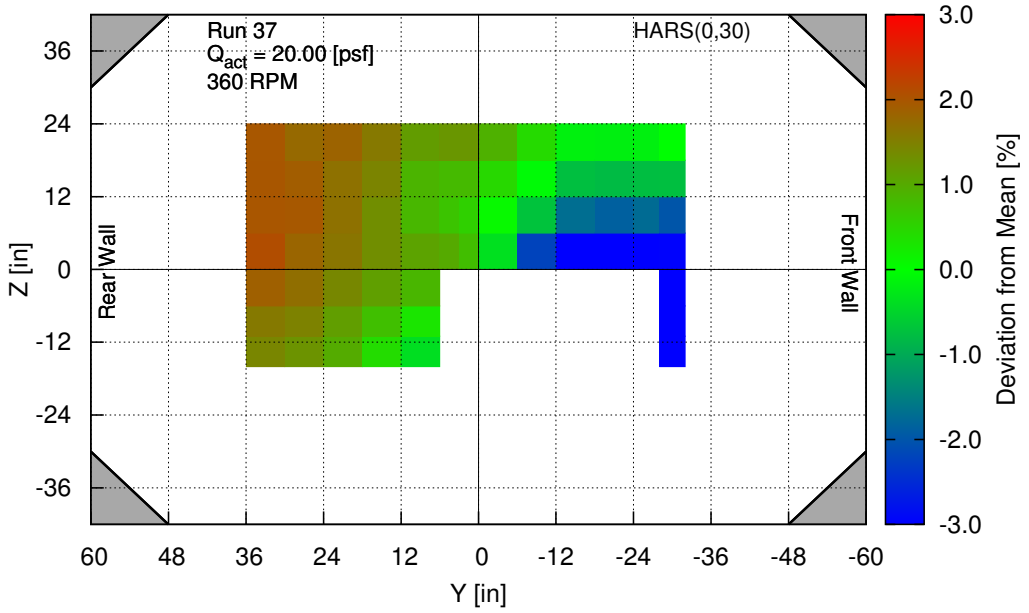

Fig. 42: Dynamic pressure variation at q_a of 20 [psf], 360 RPM, Test 1227.037.

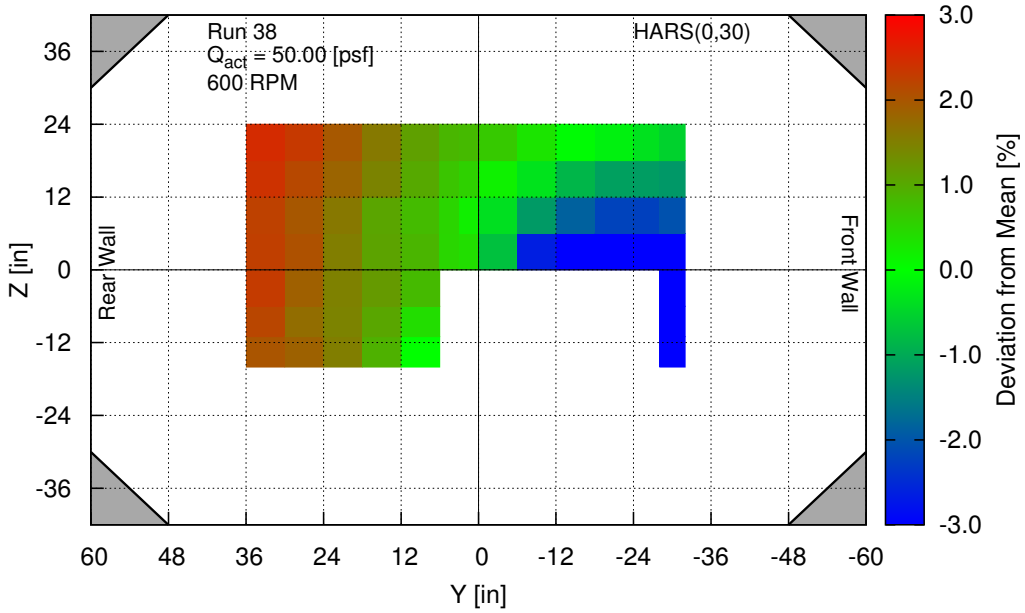

Fig. 43: Dynamic pressure variation at q_a of 50 [psf], 600 RPM, Test 1227.038.

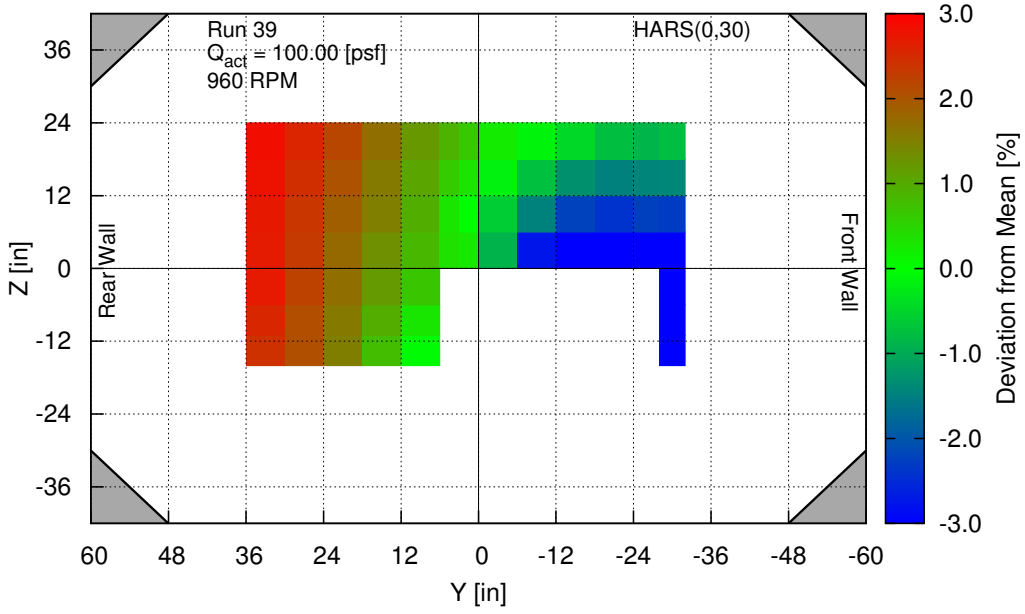

Fig. 44: Dynamic pressure variation at q_a of 100 [psf], 960 RPM, Test 1227.039.

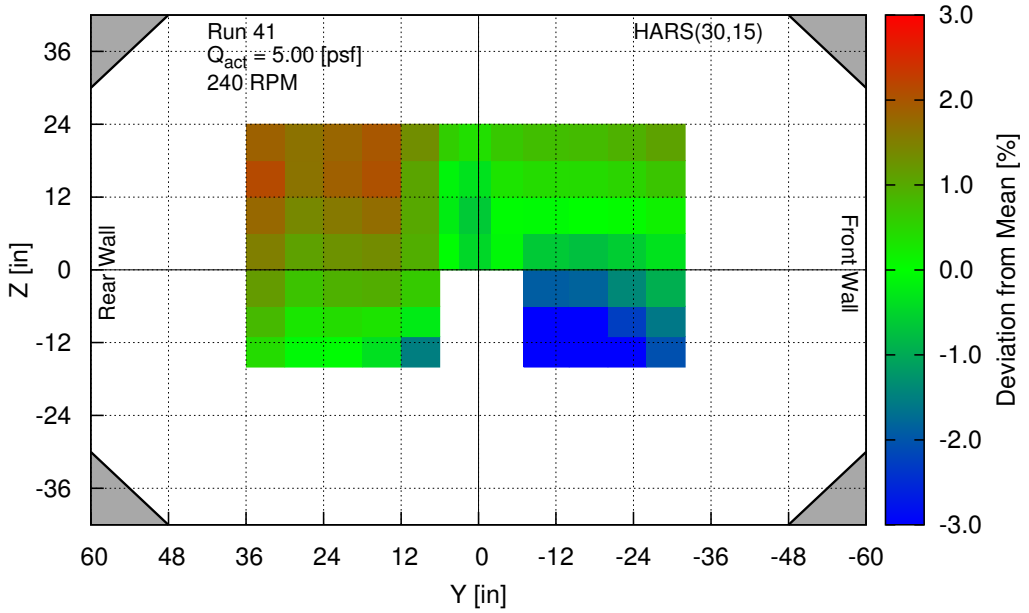

Fig. 45: Dynamic pressure variation at q_a of 5 [psf], 240 RPM, Test 1227.041.

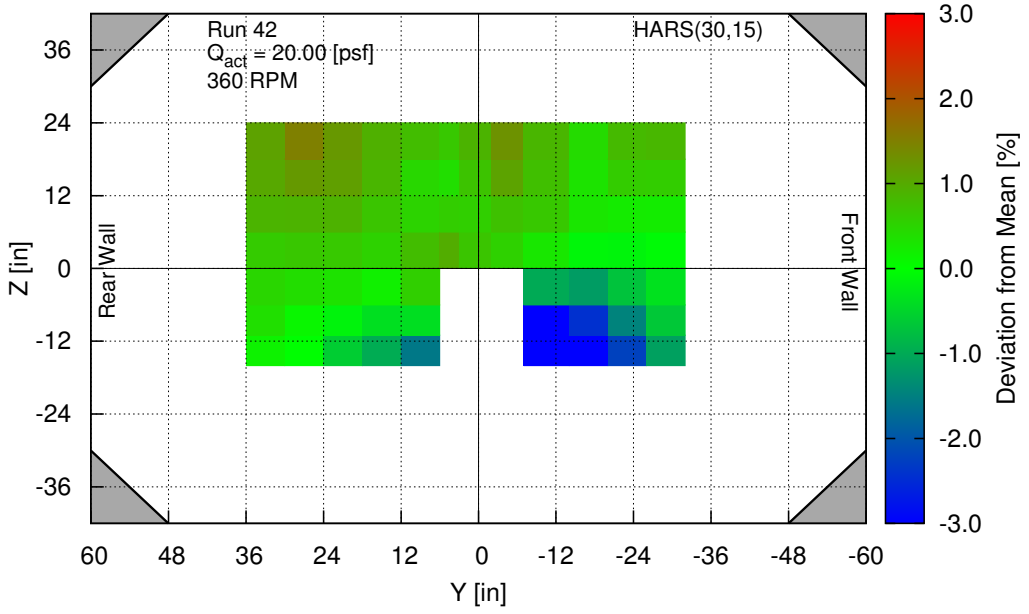

Fig. 46: Dynamic pressure variation at q_a of 20 [psf], 360 RPM, Test 1227.042.

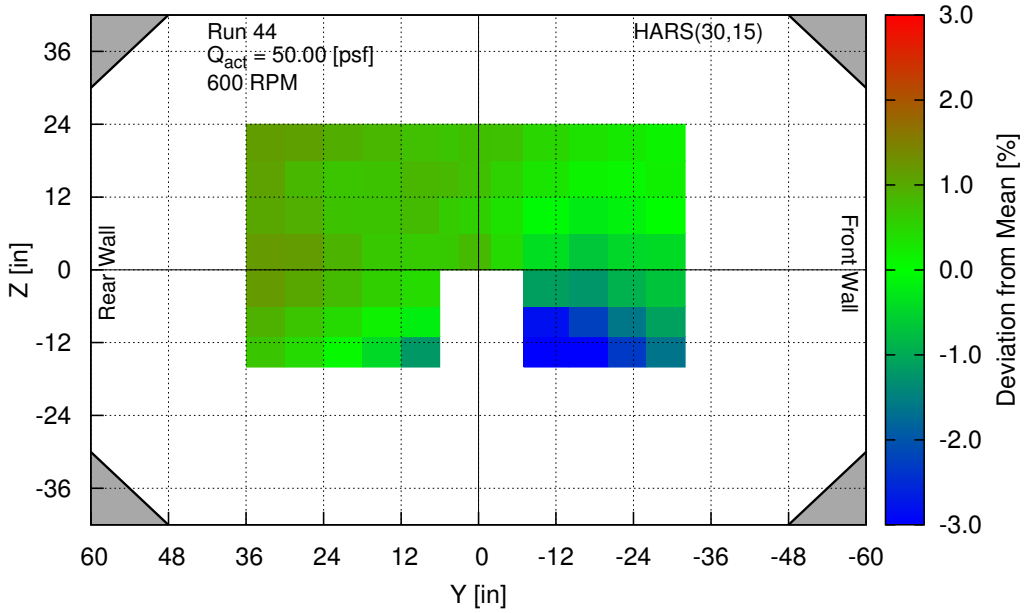

Fig. 47: Dynamic pressure variation at q_a of 50 [psf], 600 RPM, Test 1227.044.

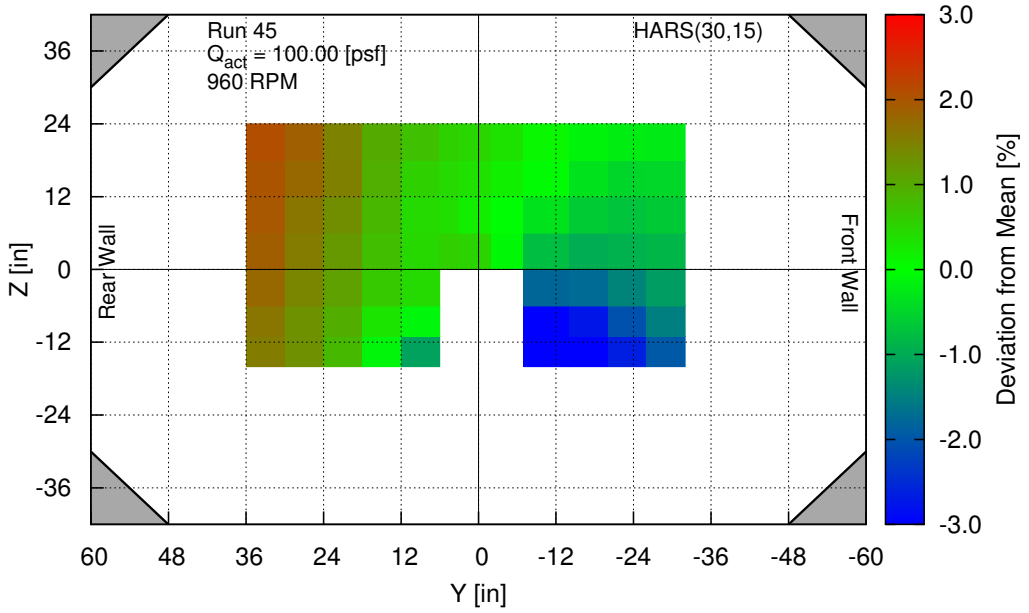

Fig. 48: Dynamic pressure variation at q_a of 100 [psf], 960 RPM, Test 1227.045.

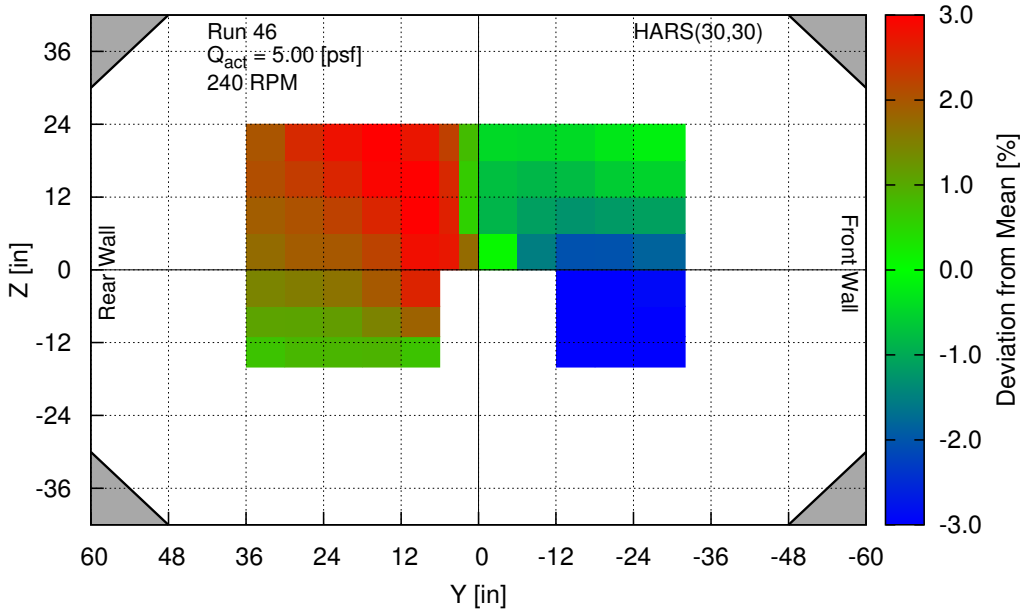

Fig. 49: Dynamic pressure variation at q_a of 5 [psf], 240 RPM, Test 1227.046.

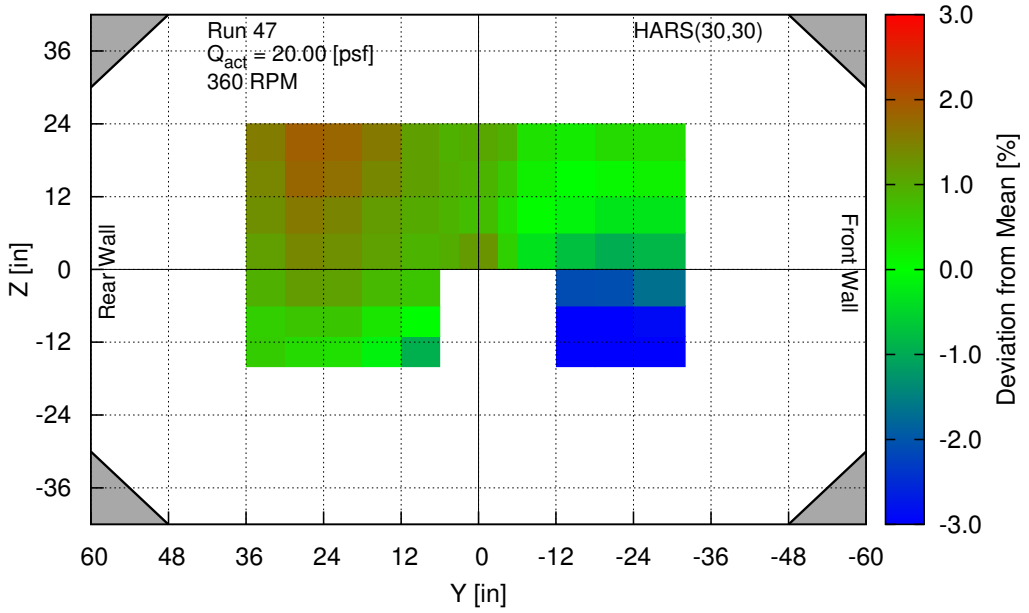

Fig. 50: Dynamic pressure variation at q_a of 20 [psf], 360 RPM, Test 1227.047.

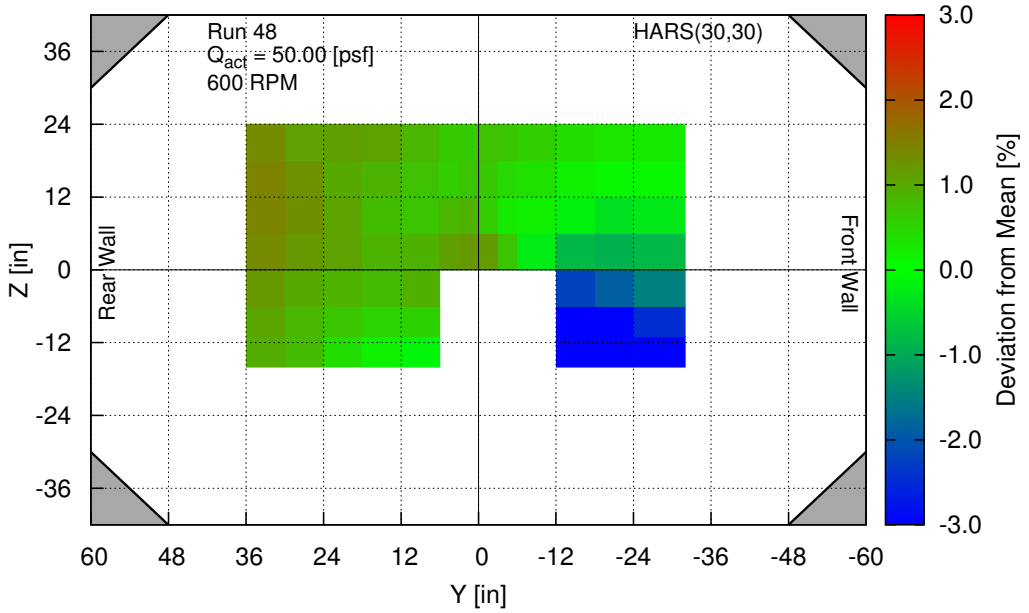

Fig. 51: Dynamic pressure variation at q_a of 50 [psf], 600 RPM, Test 1227.048.

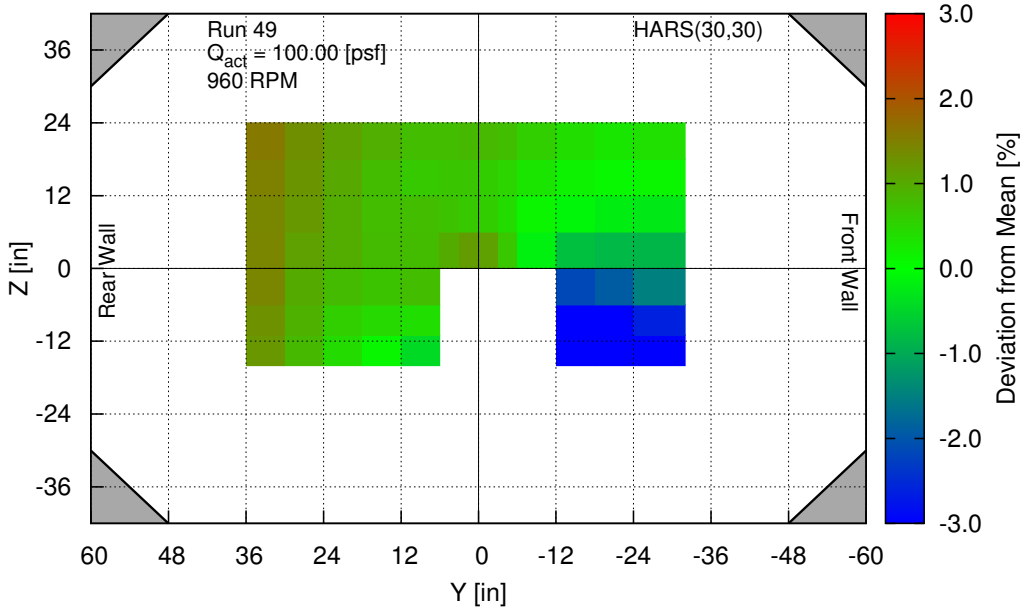

Fig. 52: Dynamic pressure variation at q_a of 100 [psf], 960 RPM, Test 1227.049.

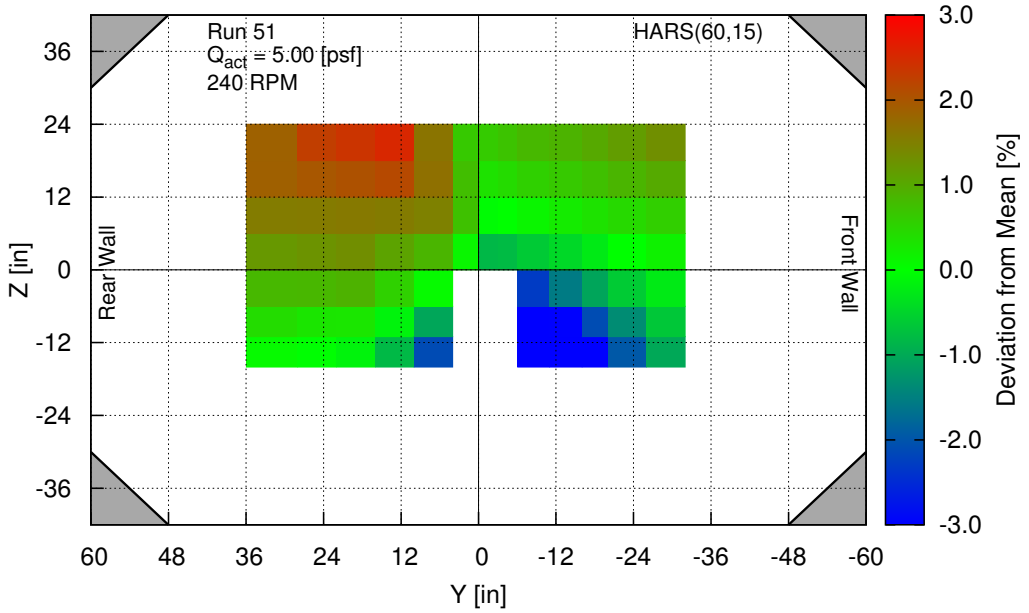

Fig. 53: Dynamic pressure variation at q_a of 5 [psf], 240 RPM, Test 1227.051.

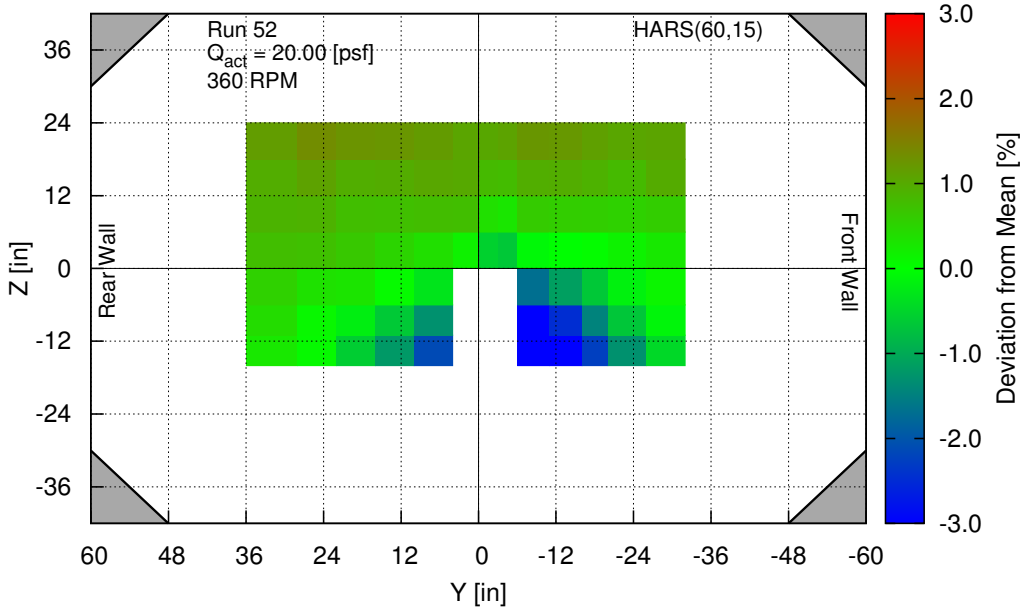

Fig. 54: Dynamic pressure variation at q_a of 20 [psf], 360 RPM, Test 1227.052.

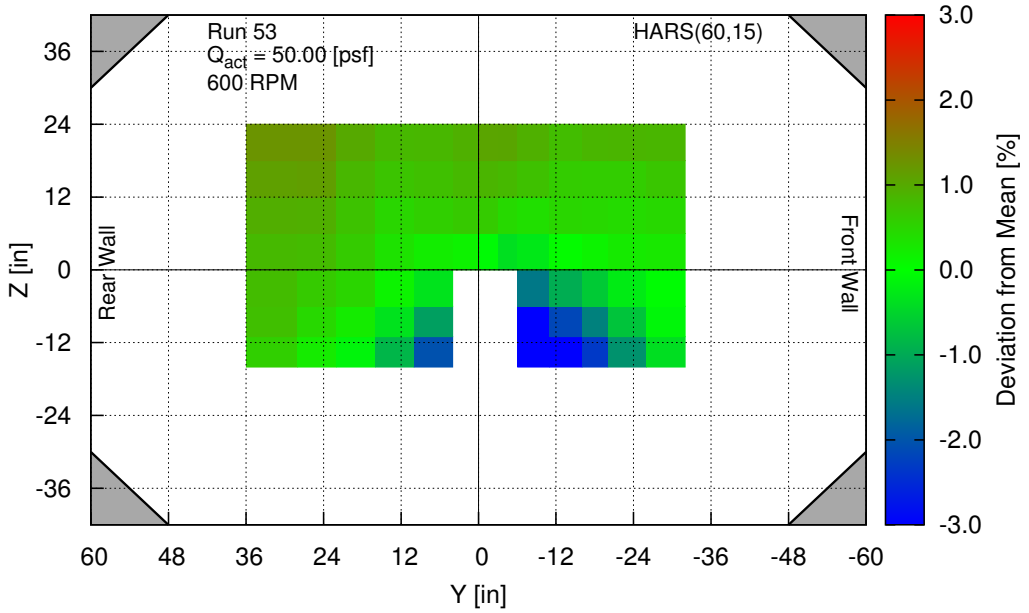

Fig. 55: Dynamic pressure variation at q_a of 50 [psf], 600 RPM, Test 1227.053.

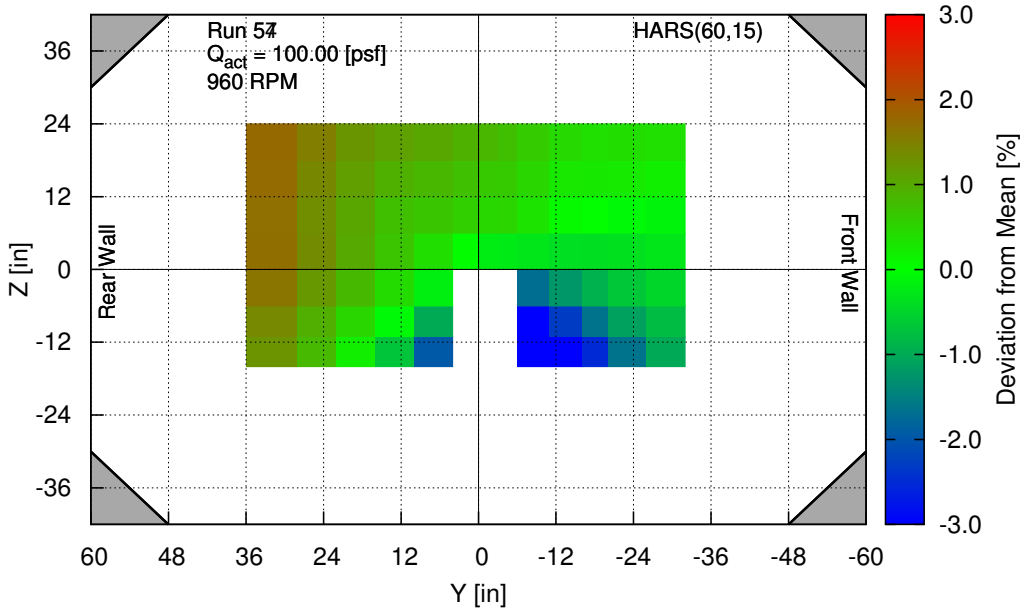

Fig. 56: Dynamic pressure variation at q_a of 100 [psf], 960 RPM, Test 1227.057.

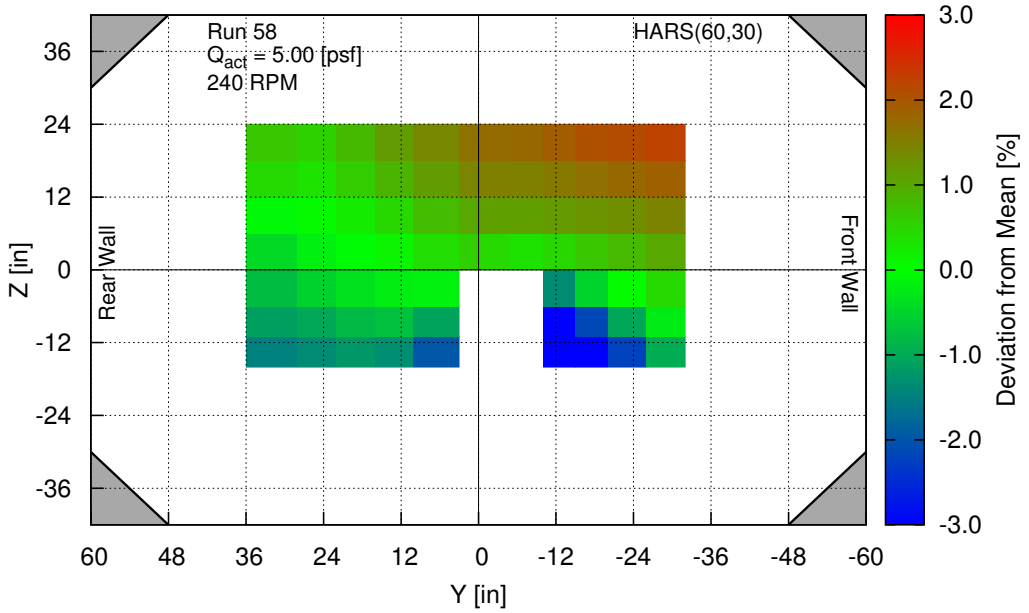

Fig. 57: Dynamic pressure variation at q_a of 5 [psf], 240 RPM, Test 1227.058.

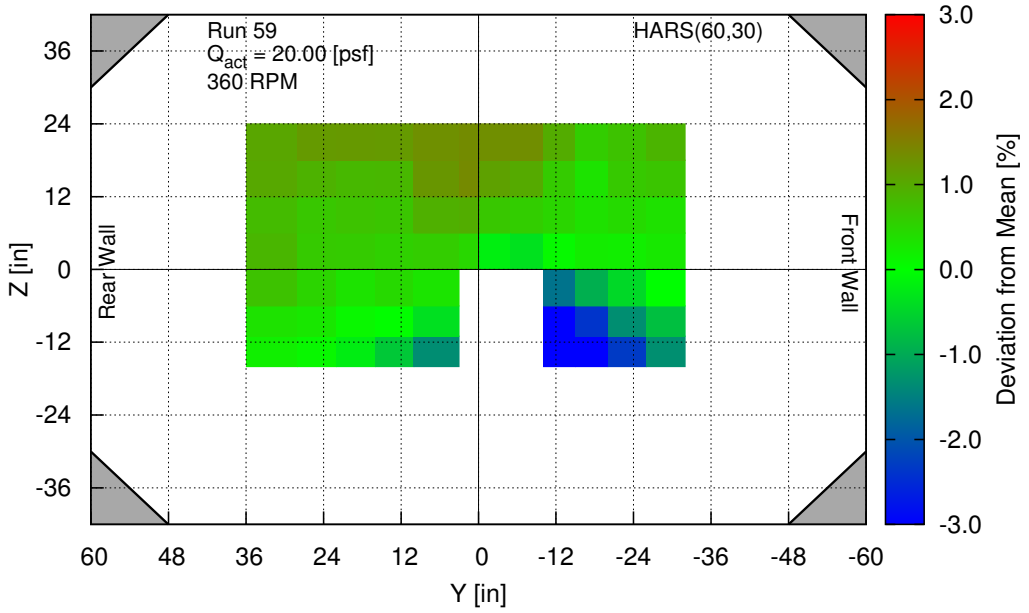

Fig. 58: Dynamic pressure variation at q_a of 20 [psf], 360 RPM, Test 1227.059.

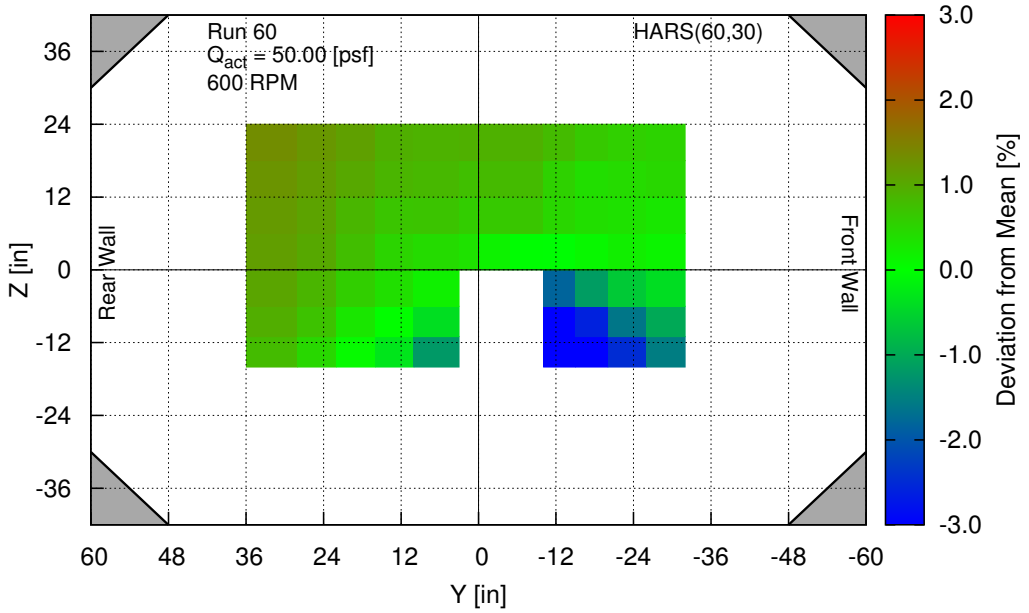

Fig. 59: Dynamic pressure variation at q_a of 50 [psf], 600 RPM, Test 1227.060.

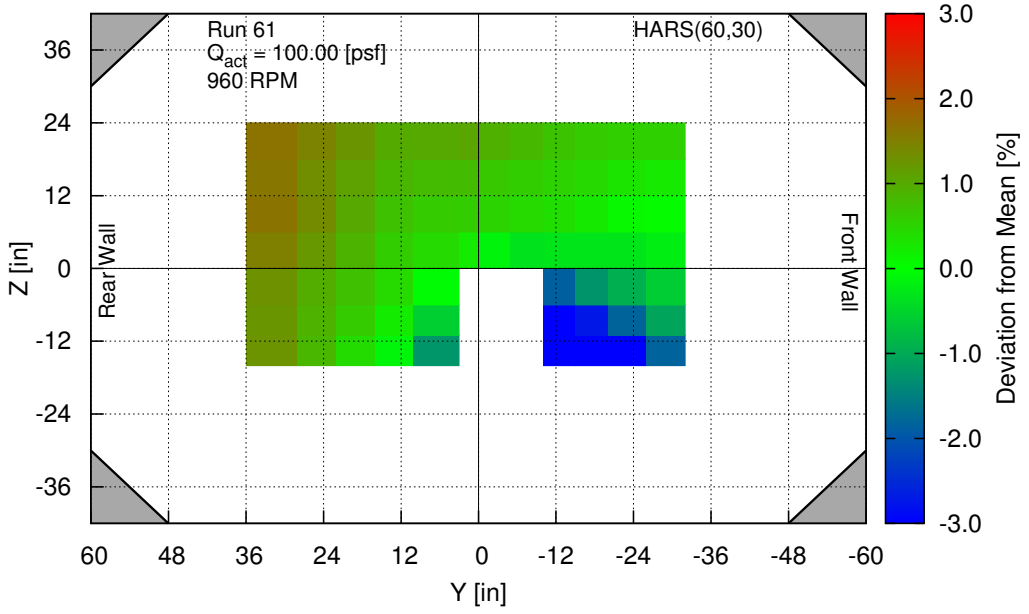

Fig. 60: Dynamic pressure variation at q_a of 100 [psf], 960 RPM, Test 1227.061.

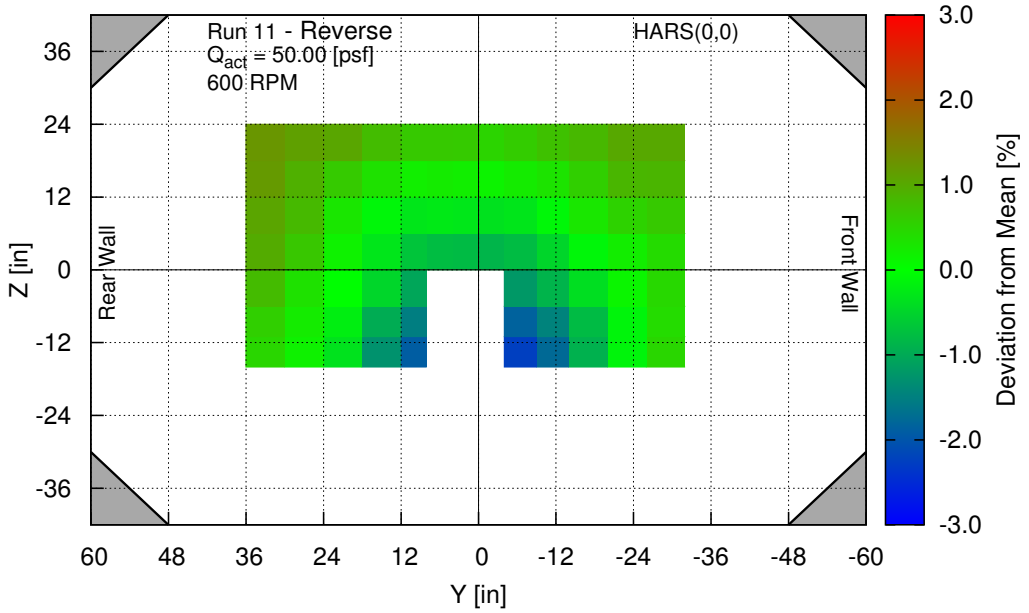

Fig. 61: Dynamic pressure variation at q_a of 50 [psf], 600 RPM, Test 1227.011.

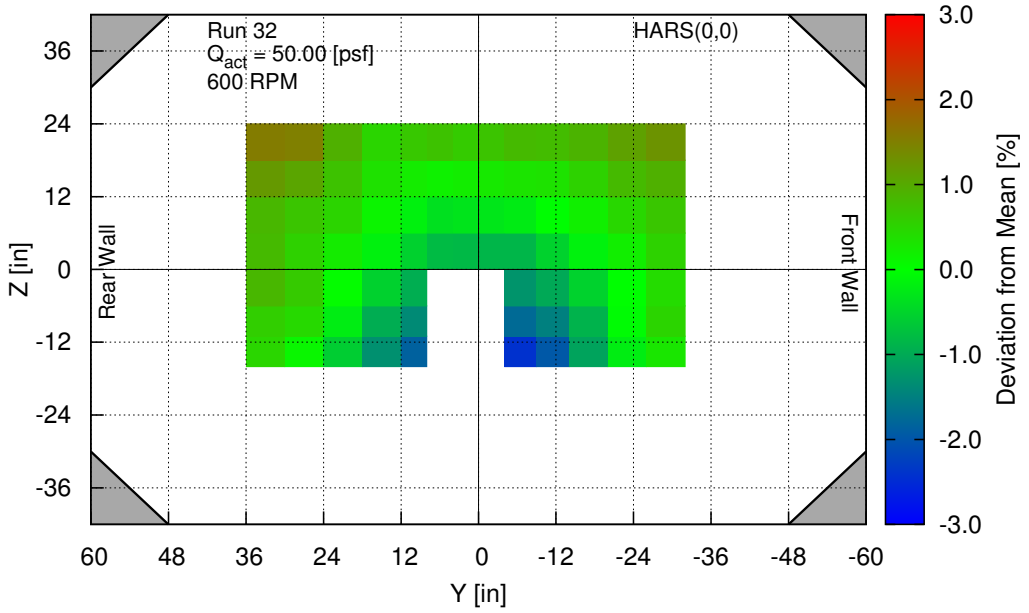

Fig. 62: Dynamic pressure variation at q_a of 50 [psf], 600 RPM, Test 1227.032.

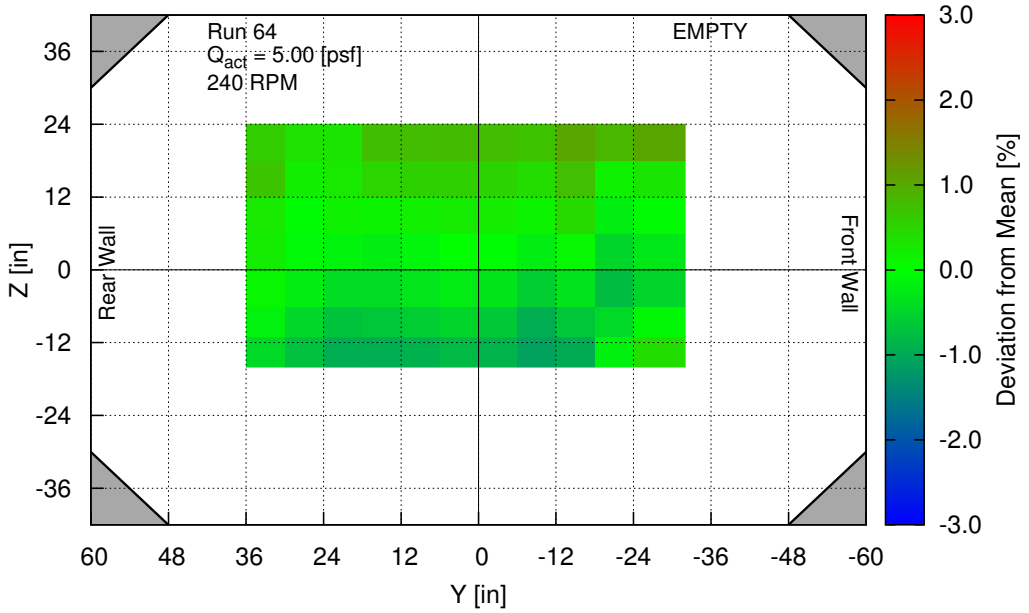

Fig. 63: Dynamic pressure variation at q_a of 5 [psf], 240 RPM, Test 1227.064.

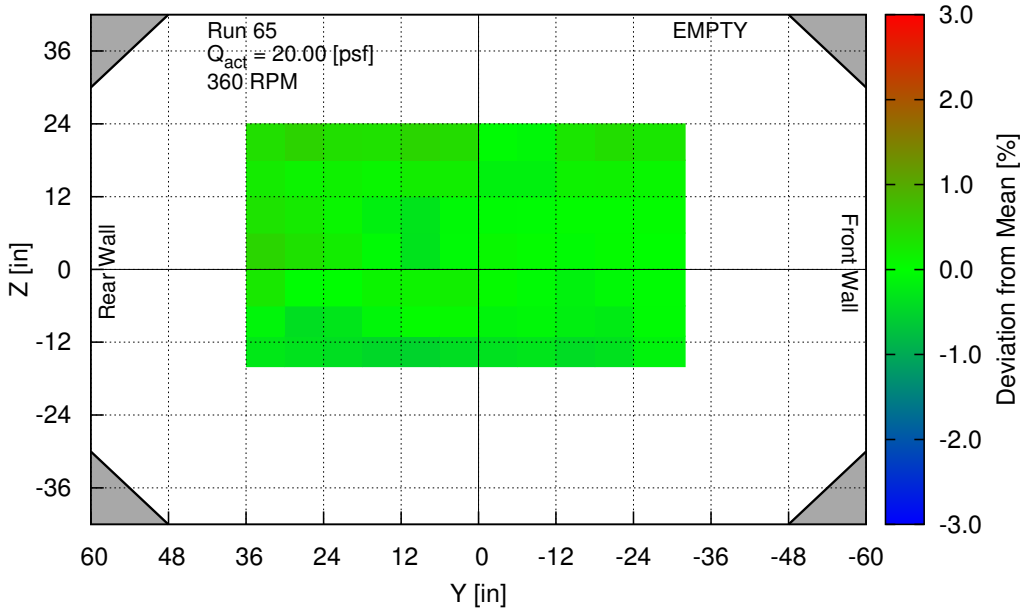

Fig. 64: Dynamic pressure variation at q_a of 20 [psf], 360 RPM, Test 1227.065.

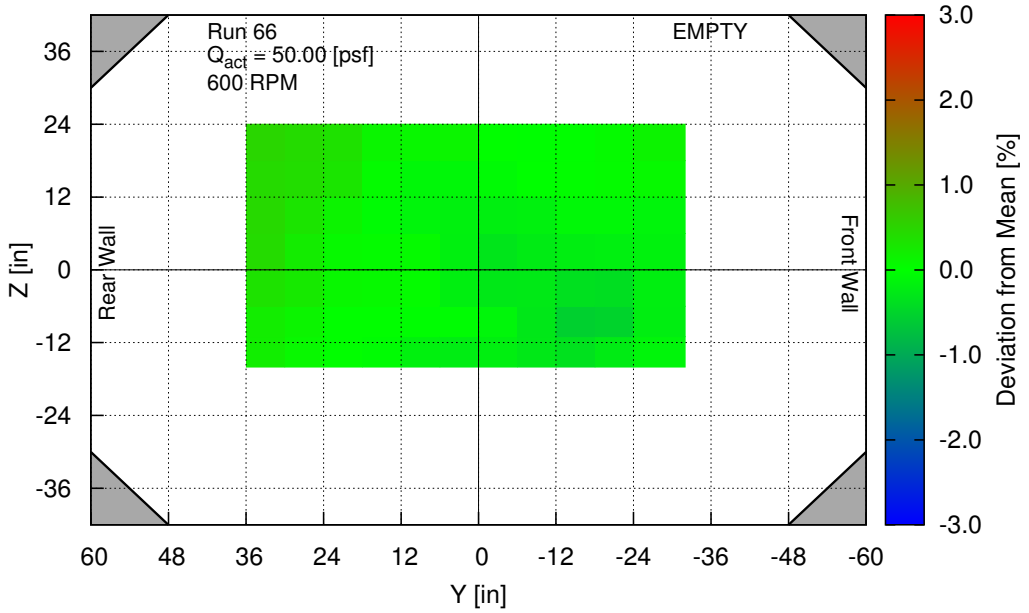

Fig. 65: Dynamic pressure variation at q_a of 50 [psf], 600 RPM, Test 1227.066.

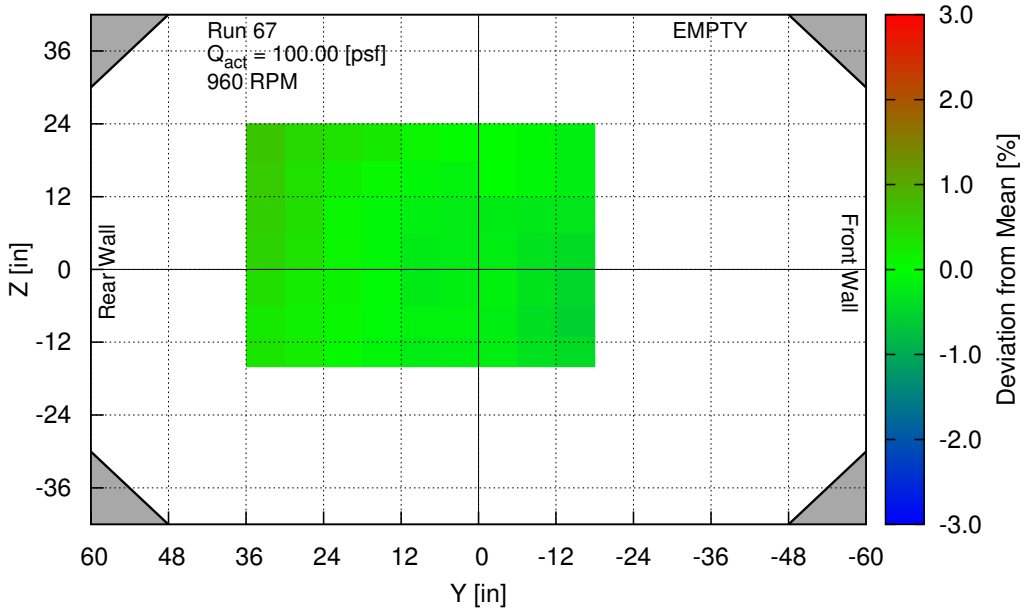

Fig. 66: Dynamic pressure variation at q_a of 100 [psf], 960 RPM, Test 1227.067.

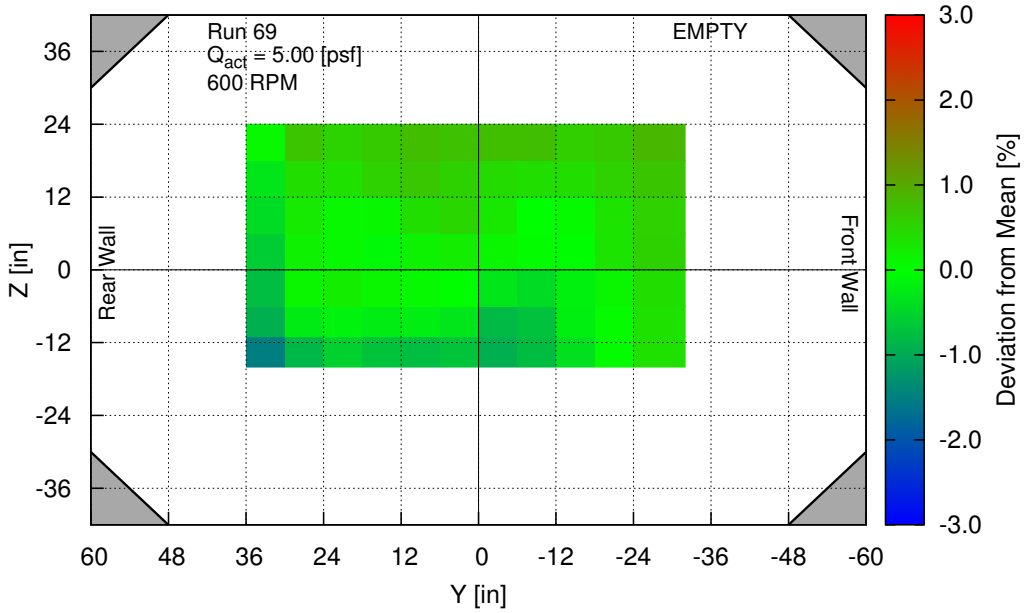

Fig. 67: Dynamic pressure variation at q_a of 5 [psf], 600 RPM, Test 1227.069.

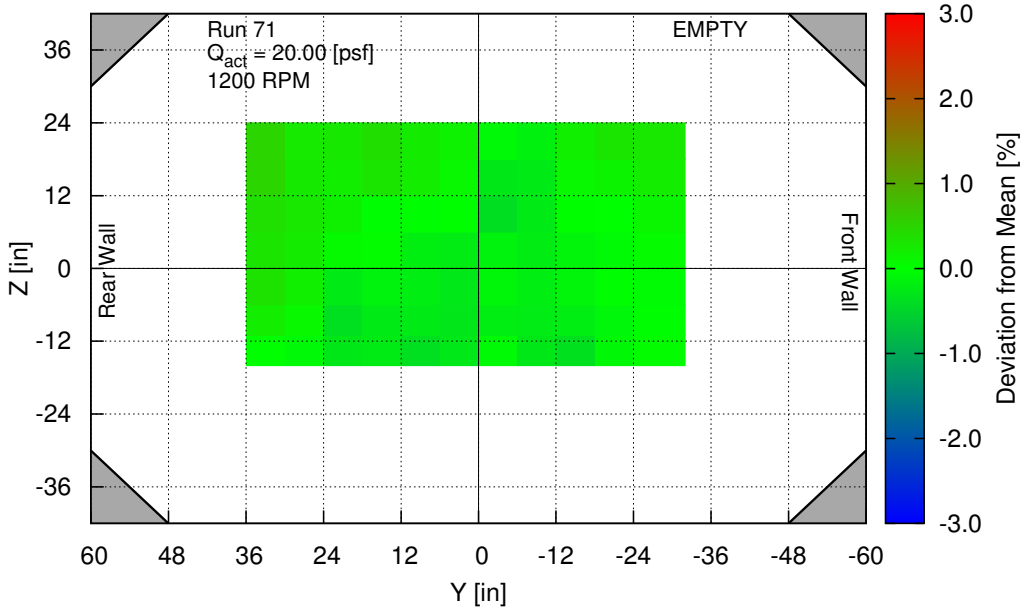

Fig. 68: Dynamic pressure variation at q_a of 20 [psf], 1200 RPM, Test 1227.071.

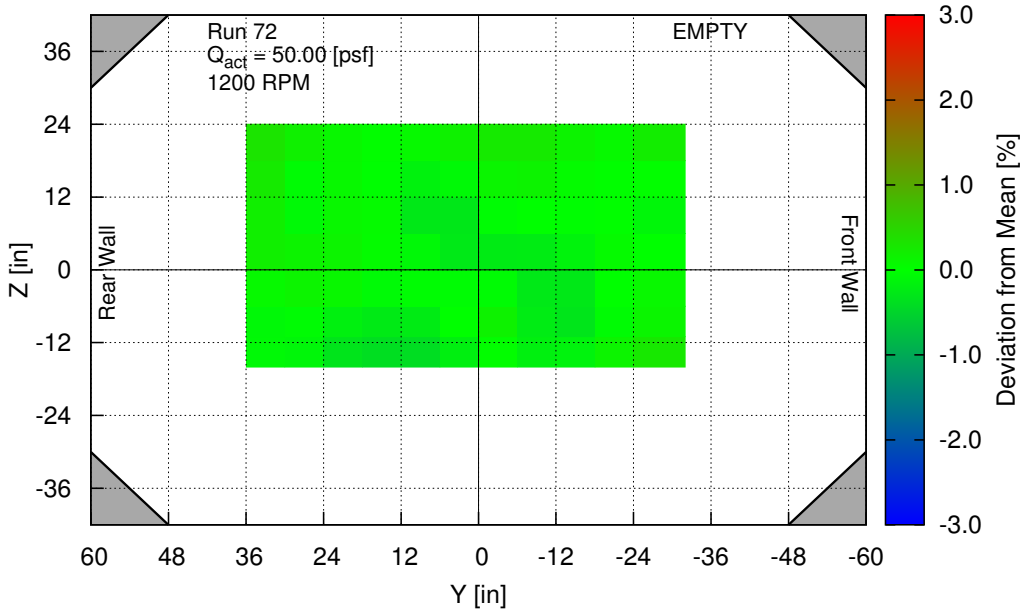

Fig. 69: Dynamic pressure variation at q_a of 50 [psf], 1200 RPM, Test 1227.072.

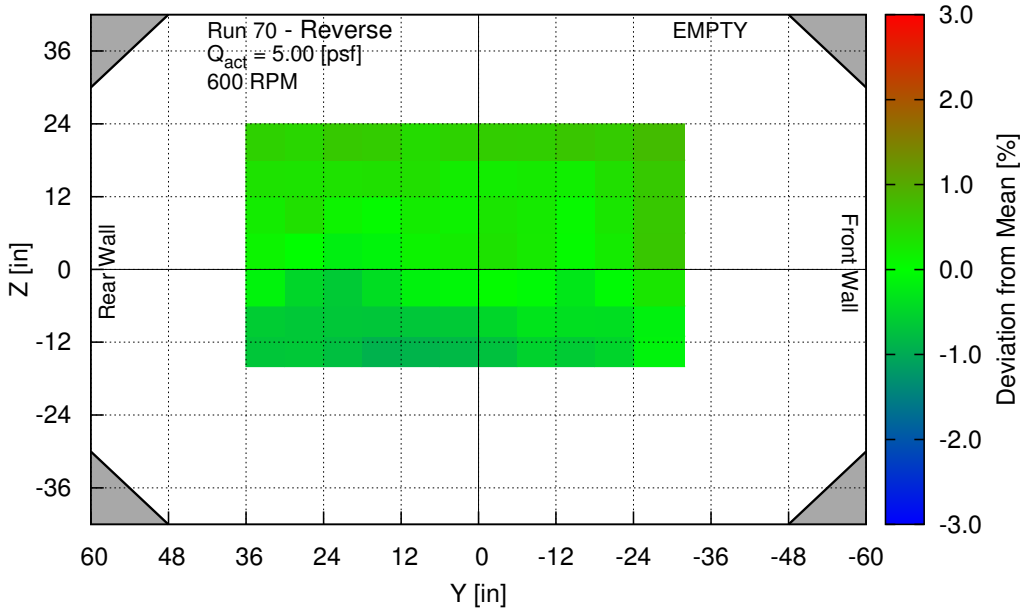

Fig. 70: Dynamic pressure variation at q_a of 5 [psf], 600 RPM, Test 1227.070.

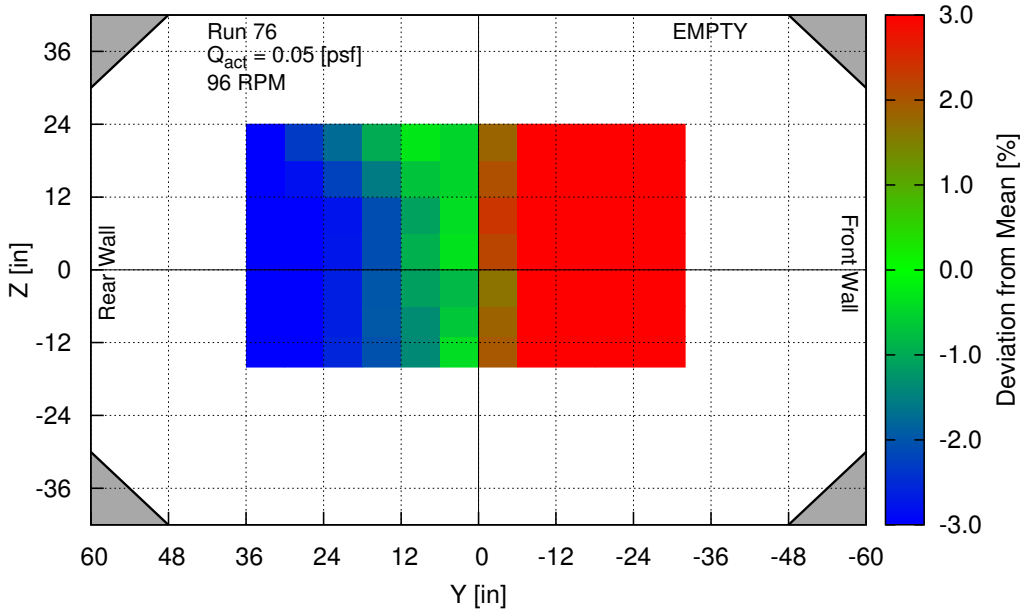

Fig. 71: Dynamic pressure variation at q_a of 0.05 [psf], 96 RPM, Test 1227.076.

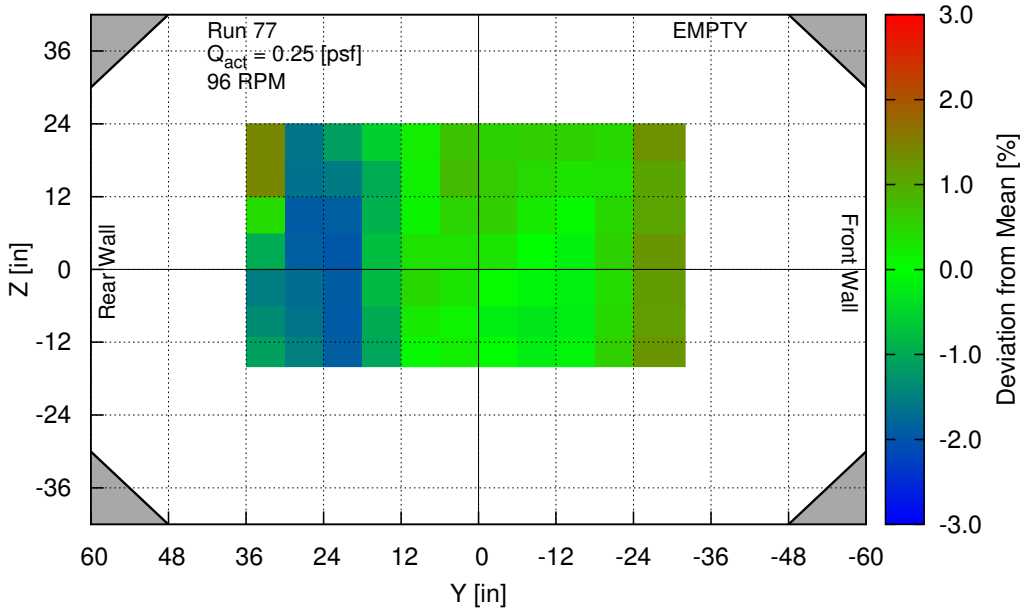

Fig. 72: Dynamic pressure variation at q_a of 0.25 [psf], 96 RPM, Test 1227.077.

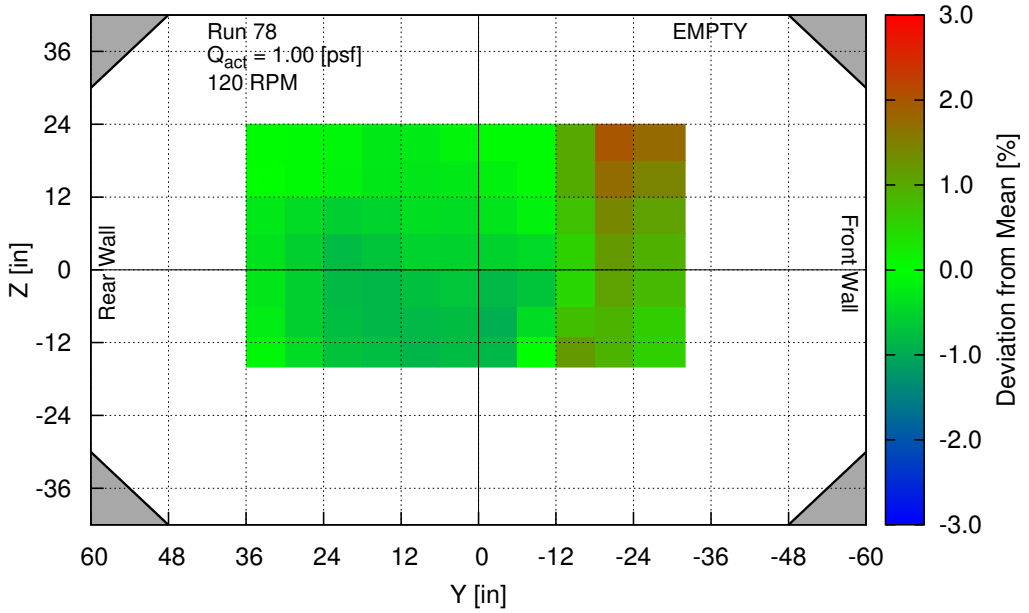

Fig. 73: Dynamic pressure variation at q_a of 1 [psf], 120 RPM, Test 1227.078.

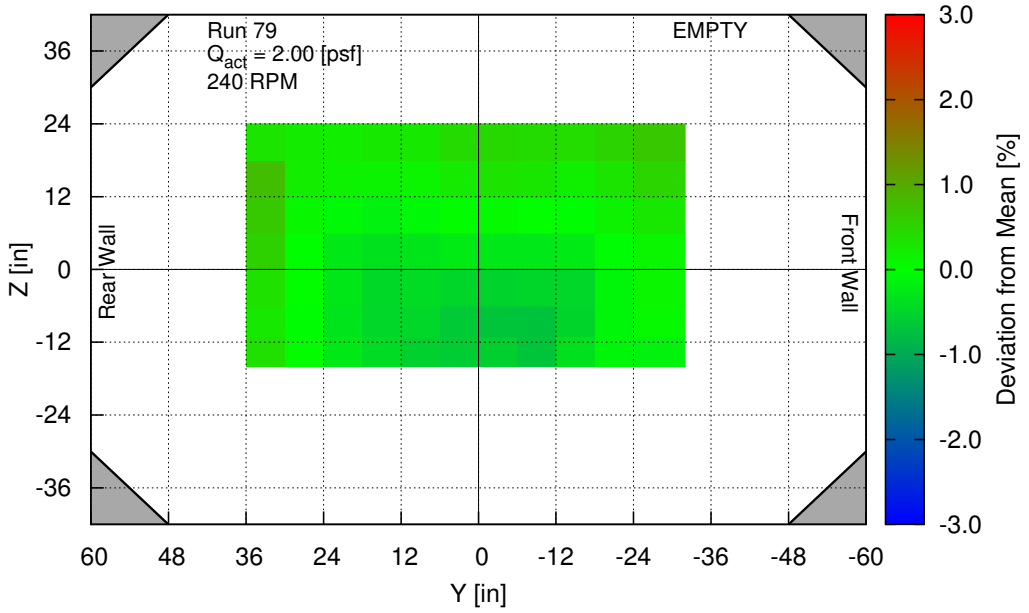

Fig. 74: Dynamic pressure variation at q_a of 2 [psf], 240 RPM, Test 1227.079.

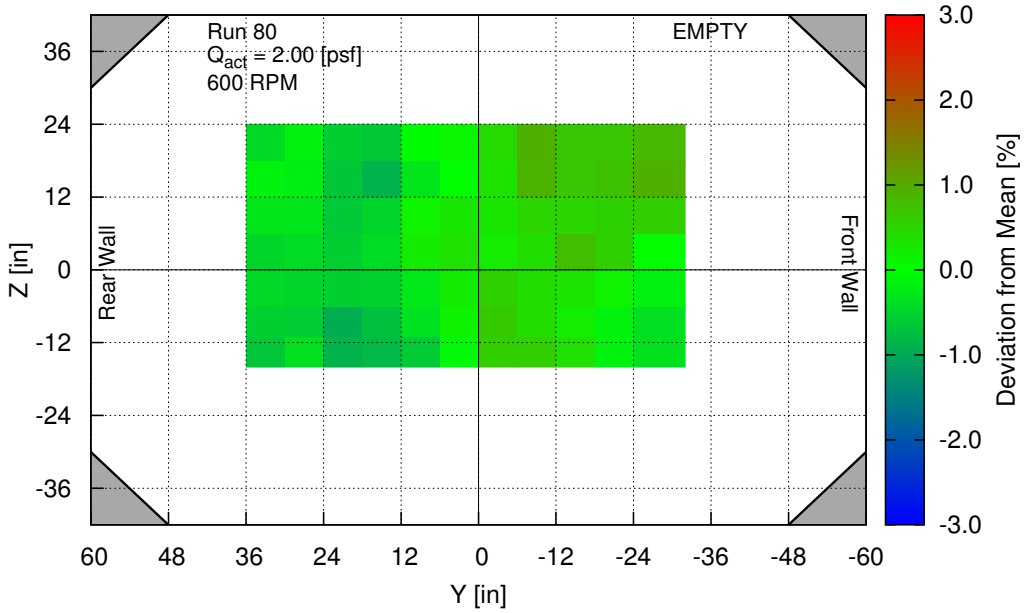

Fig. 75: Dynamic pressure variation at q_a of 2 [psf], 600 RPM, Test 1227.080.

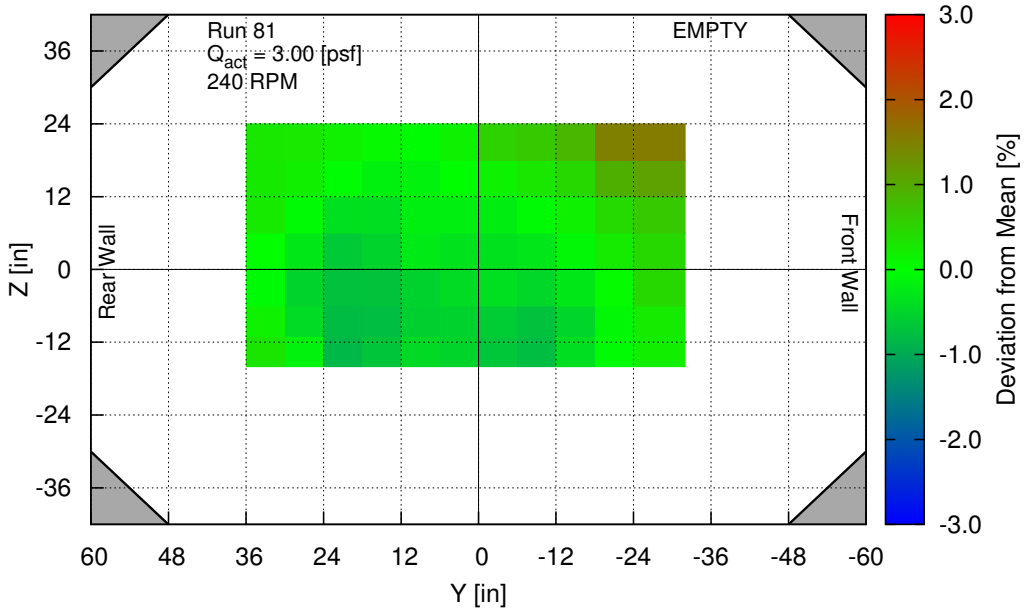

Fig. 76: Dynamic pressure variation at q_a of 3 [psf], 240 RPM, Test 1227.081.

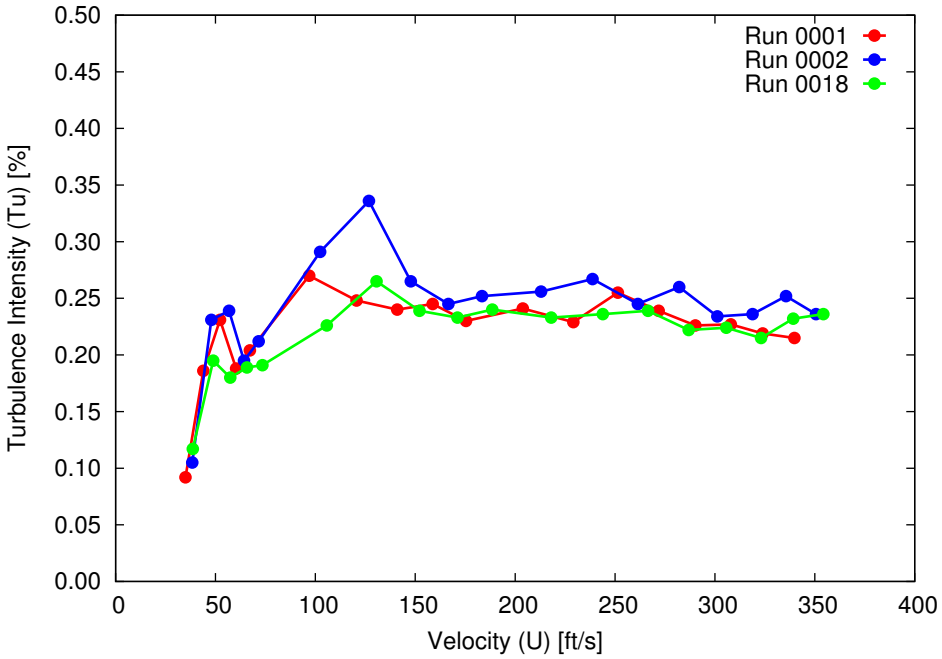

Fig. 77: Turbulence intensity values for a range of test section dynamic pressures.

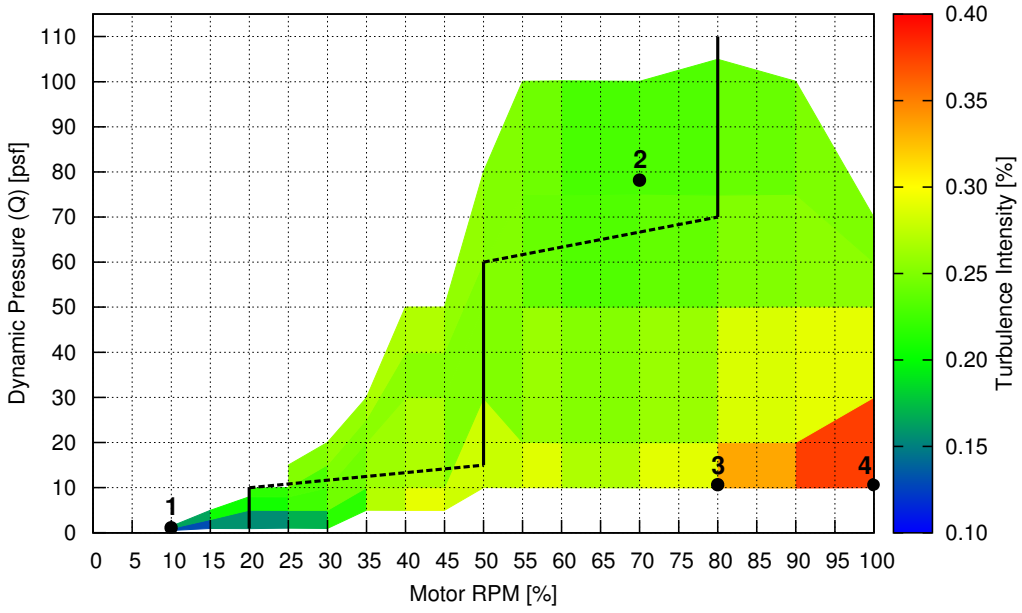

Fig. 78: Turbulence intensity map from LSWT Test 1236 as a function of motor power and test section dynamic pressure.

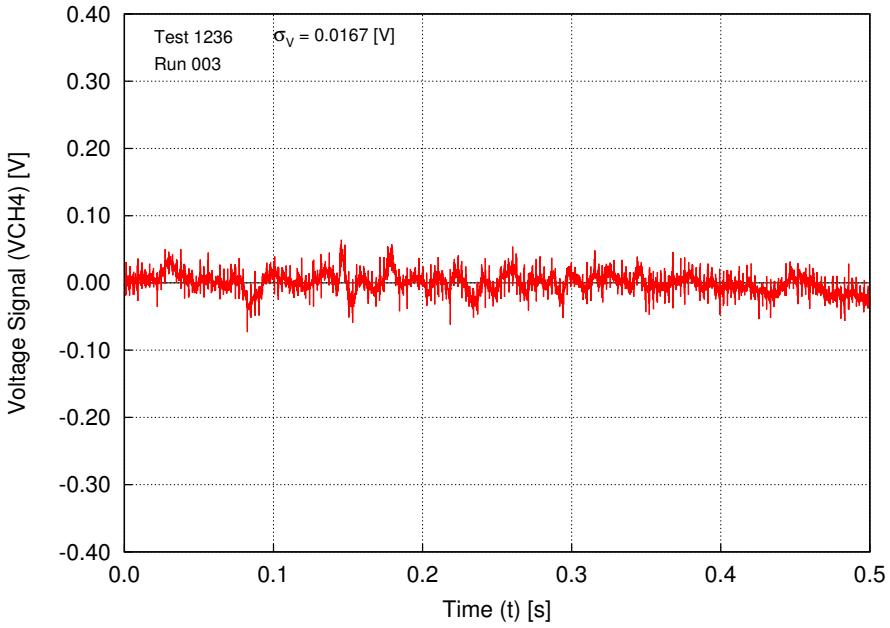

Fig. 79: Filtered voltage signal from the hot-wire for point 1 at 10% motor power.

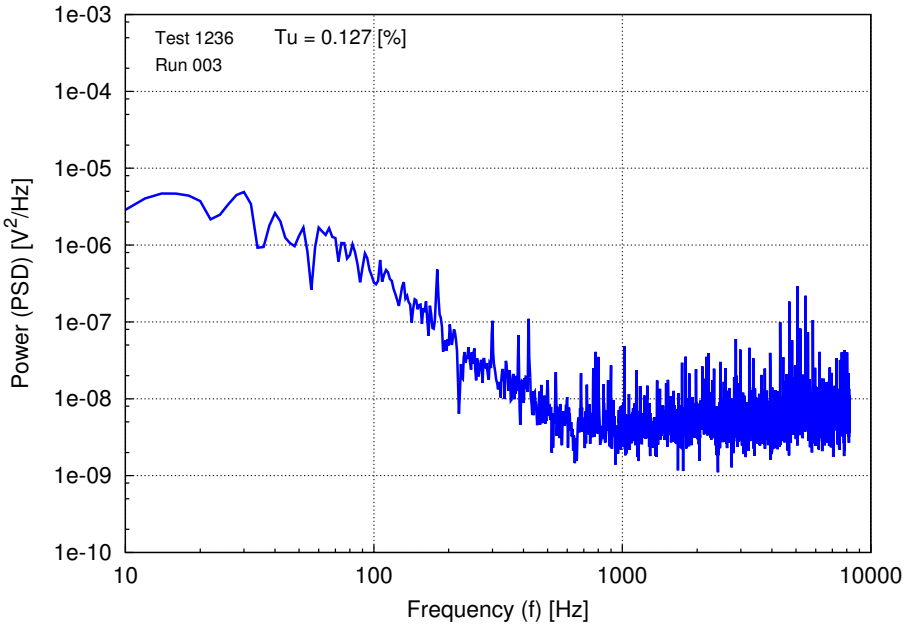

Fig. 80: Power spectra in the frequency domain of the voltage signal for point 1.

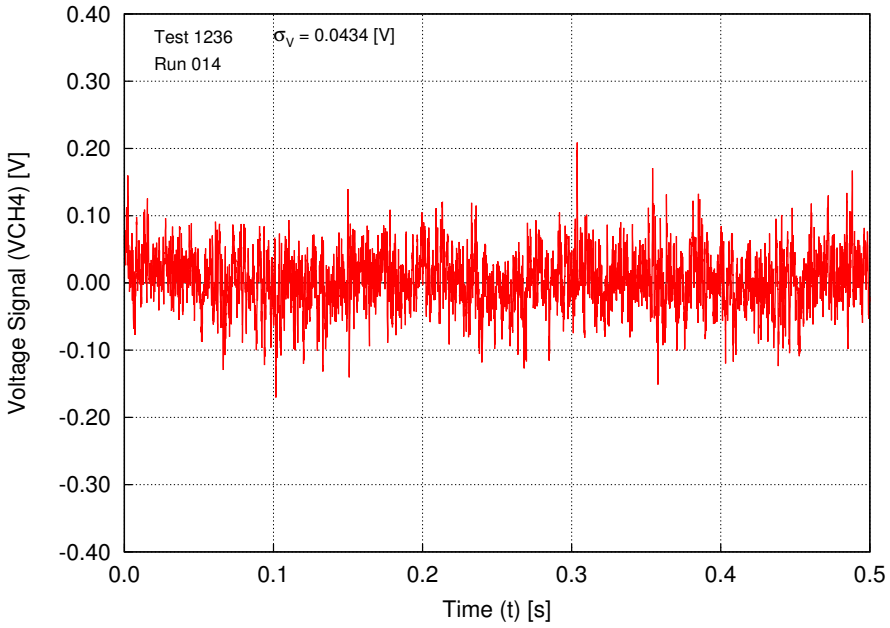

Fig. 81: Filtered voltage signal from the hot-wire for point 2 at 70% motor power.

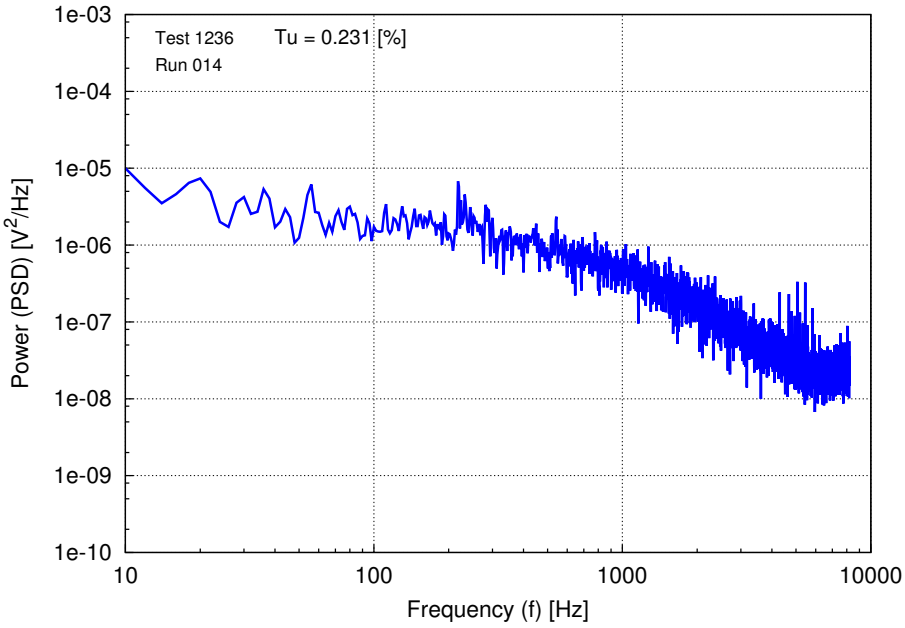

Fig. 82: Power spectra in the frequency domain of the voltage signal for point 2.

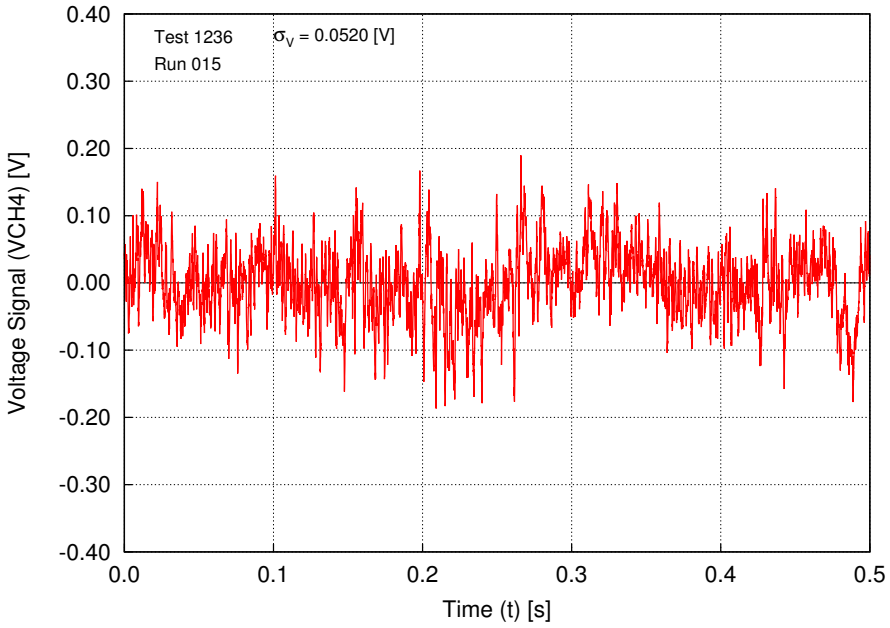

Fig. 83: Filtered voltage signal from the hot-wire for point 3 at 80% motor power.

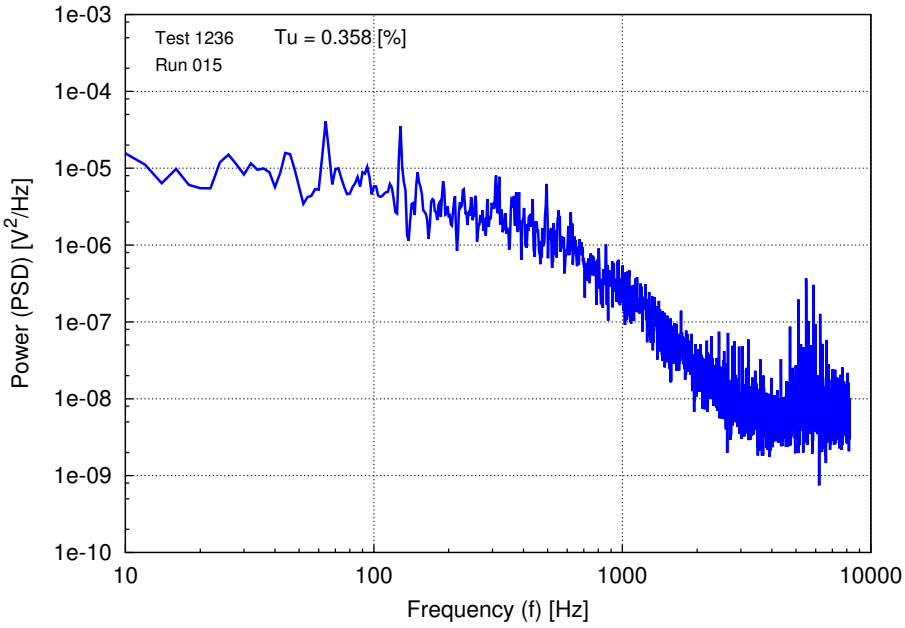

Fig. 84: Power spectra in the frequency domain of the voltage signal for point 3.

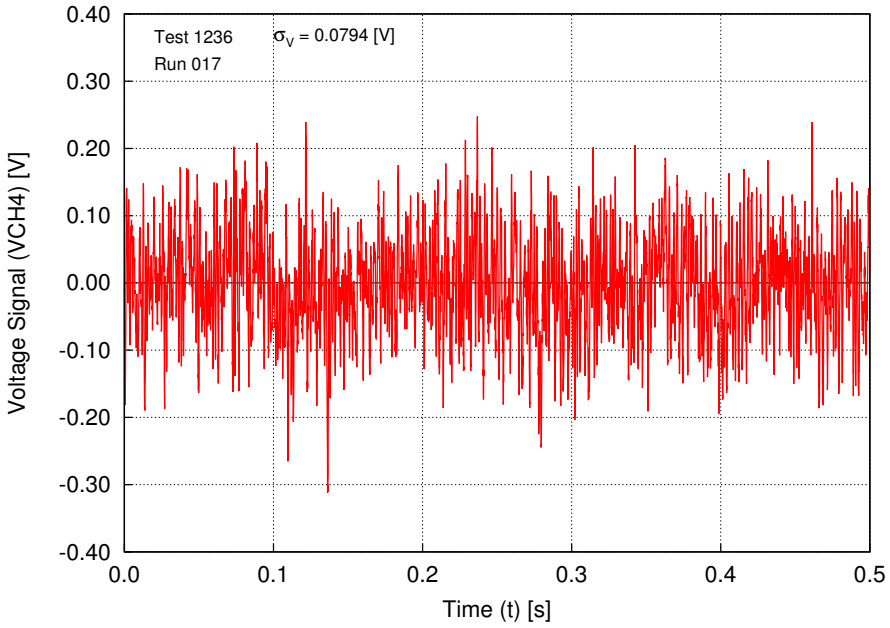

Fig. 85: Filtered voltage signal from the hot-wire for point 4 at 100% motor power.

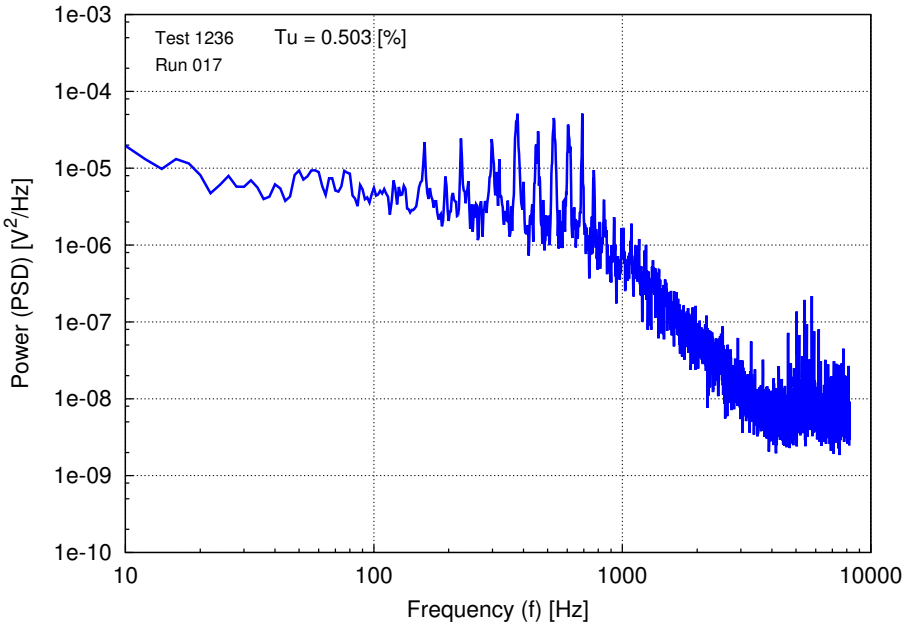

Fig. 86: Power spectra in the frequency domain of the voltage signal for point 4.

APPENDIX D

MOTOR OPERATION PLOT DATABASE

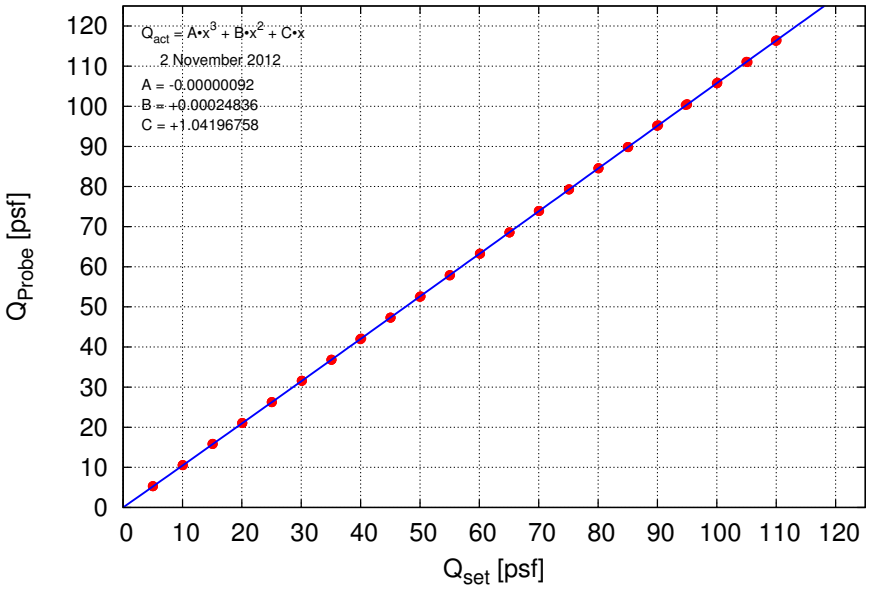

Fig. 87: Calibration between the contraction pressure differential and the true test section dynamic pressure.

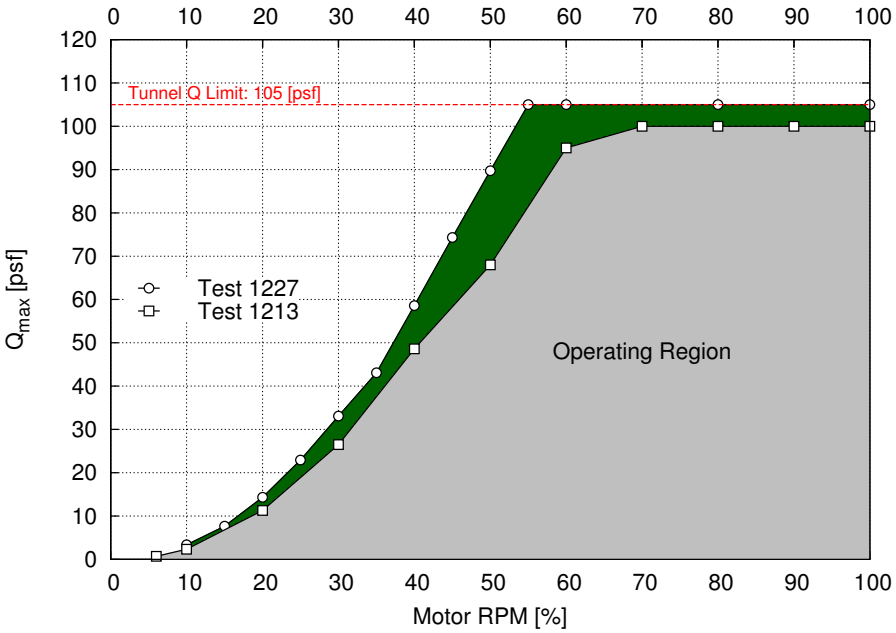

Fig. 88: Operational range of the tunnel at different motor RPM values.

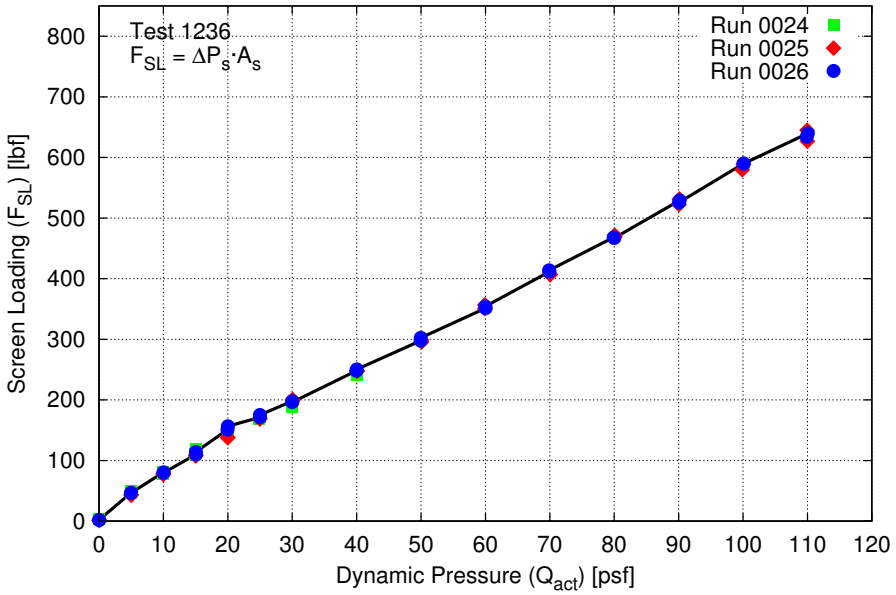

Fig. 89: Approximate calculated drag force on the screens.

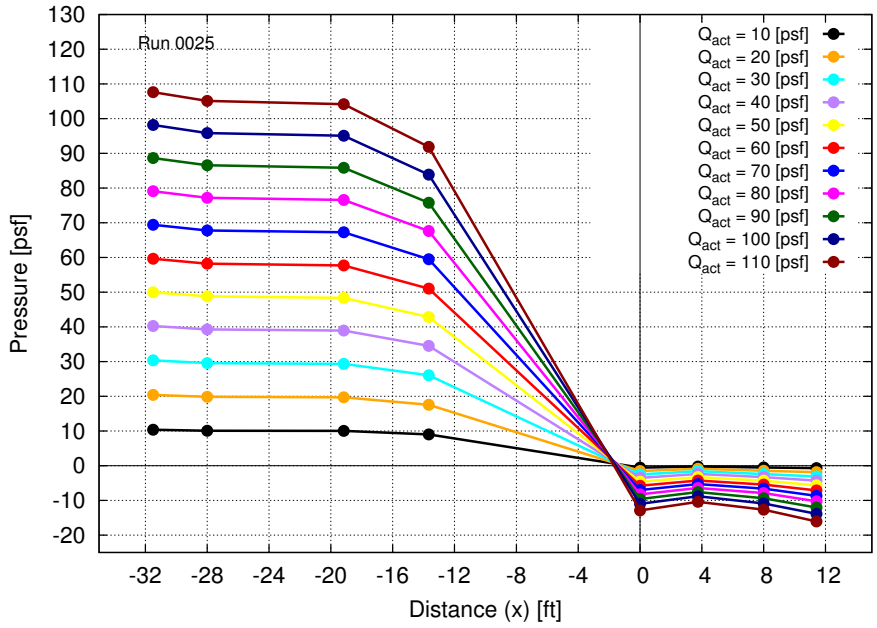

Fig. 90: Static pressure deviation along the tunnel at various dynamic pressures.

APPENDIX E

CHECKLIST DATABASE

Internal Balance Testing Checklist

Ver. 1.0, Instructions on Reverse Side *Updated 6 Dec. 2012*

Test Set-Up

- ◯ Mount Installation ..... COMPLETE
- ◯ Internal Balance Installation ..... COMPLETE
- ◯ Sting Deflections ..... COMPLETE
- ◯ Model Installation ..... COMPLETE
- ◯ Pressure Measurements ..... READY
- ◯ Foul Circuit ..... READY
- ◯ Test Matrix ..... READY

Testing Considerations

- ◯ Re_c Dependency ..... DONE
- ◯ Flow Angularity (Pitch) ..... DONE
- ◯ Flow Angularity (Yaw) ..... DONE
- ◯ Repeatability Test ..... DONE
- ◯ Sensativity Test ..... DONE

AM Procedures

- ◯ Model Position Check ..... DONE

Check all deflection possibilities:

- ◯ Pitch ..... DONE
- ◯ Yaw ..... DONE
- ◯ Roll ..... DONE

- ◯ IB Load Check ..... DONE

Check all loading cases:

- ◯ Normal Force (-/+) ..... DONE
- ◯ Side Force (-/+) ..... DONE
- ◯ Axial Force (-/+) ..... DONE
- ◯ Rolling Moment (-/+) ..... DONE

Internal Balance Testing Procedure Completion				
	AM Procedures		**PM Procedures**	
Date	Completed By:	Time:	Completed By:	Time:

Checklist Signed Off By: Test Completion Date:

Fig. 91: Version 1.0 of the Internal Balance Testing Checklist.

Checklist Instructions

Complete the checklist:

Verified or Completed Step: ⓥ or ◉

Skipped Step: ⊖

Use the notes block to indicate any problems, maintenance issues, and remark why steps were not completed.

The tunnel operations lead signs the checklist upon completion while noting the date and time.

Procedural Details

Notes

HARS Installation Checklist

Ver. 1.0, Instructions on Reverse Side *Updated 19 Nov. 2012*

Pre-Installation

- ◯ External balance ..... ON
- ◯ External balance zeroed ..... YES
- ◯ Test section roof ..... OFF
- ◯ Floor plate ..... OFF
- ◯ Two 1 [ft] struts ..... INSTALLED
- ◯ West clamp set at $10\frac{15}{16}$ [in] ..... YES
- ◯ Tighten slider side of west clamp ..... YES
- ◯ HARS cradle-halves ..... INSTALLED
- ◯ Alignment block ..... INSTALLED
- ◯ Tighten slider side, both clamps ..... YES
- ◯ Upper TT (switch) ..... OFF
- ◯ Upper TT slot down long axis ..... YES
- ◯ Lower TT (breaker) ..... ON
- ◯ Ignore UTT (switch) ..... ON
- ◯ Upper TT slot down long axis ..... YES
- ◯ Check table alignment ..... YES
- ◯ Alignment block ..... UNINSTALLED

Installation

- ◯ HARS in ready room ..... YES
- ◯ HARS attached to hoist ..... YES
- ◯ Lead line attached ..... YES
- ◯ Unbolt HARS from stand ..... YES
- ◯ Lift HARS into test section ..... YES
- ◯ Run four HARS motor cables ..... YES
- ◯ Run three roll motor cables ..... YES
- ◯ Set HARS into cradle halves ..... INSTALLED
- ◯ Bolt HARS to cradle halves ..... YES
- ◯ Tighten clamp side, both clamps ..... YES
- ◯ Check HARS block correct ..... YES
- ◯ Protective coat "90°" block ..... YES

Connection

- ◯ Relay (switch) ..... OFF
- ◯ Big red button ..... OFF
- ◯ Front and rear strut cables ..... CONNECTED
- ◯ Roll motor control cable ..... CONNECTED
- ◯ Grounding strap ..... CONNECTED
- ◯ Roll motor fan power supply ..... CONNECTED
- ◯ Roll motor thermocouple ..... CONNECTED
- ◯ Motion (breaker) ..... ON
- ◯ Beta (breaker) ..... ON
- ◯ Front Strut (breaker) ..... ON
- ◯ Rear Strut (breaker) ..... ON
- ◯ SoHARS Roll (breaker) ..... ON

Program Start-Up

- ◯ Visual Studio on "Motion" ..... OPEN
- ◯ "Motion Control - HARS2" ..... OPEN
- ◯ Program set for correct block ..... YES
- ◯ Big red button ..... ON
- ◯ Relay (switch) ..... ON
- ◯ Ignore UTT (switch) ..... OFF
- ◯ Upper TT (switch) ..... ON
- ◯ Automate (switch) ..... ON
- ◯ Click input fields and zero ..... YES
- ◯ Submit (button) ..... YES

Post-Installation

- ◯ Test section roof ..... ON
- ◯ Floor plate ..... ON
- ◯ Rough alignment transit ..... YES
- ◯ Pressure system needed ..... YES
- ◯ Connect foul circuit ..... YES

Checklist Complete By: Date and Time:

Fig. 92: Version 1.0 of the HARS Installation Checklist.

Checklist Instructions

Complete the checklist:

Verified or Completed Step: ⓥ or ◉

Skipped Step: ⊖

Use the notes block to indicate any problems, maintenance issues, and remark why steps were not completed.

The tunnel operations lead signs the checklist upon completion while noting the date and time.

Procedural Details

If removing the "90°" block and installing the standard block, it is important to coat the steel "90°" block with an oil based substance to protect it from rust.

The connections for HARS are located under the external balance in the balance room. The front strut cables and hook-up locations are marked. The 12 volt roll motor fan power supply can be plugged into a power strip on the far wall. The roll motor thermocouple needs to be hooked up to DAQ Channel 0.

When turning the breakers on, make absolutely certain that the Big Red Button and Relay switch are turned to off. Make sure to turn on the "SoHARS Roll" breaker and not the "HARS Roll" breaker.

The HARS program will not work if each input field is not activated by clicking in the field before sending the first command to HARS.

Clicking the "Submit" button will bring HARS out of storage to the zero position. If the following error becomes too large at any point, click "Clear Following Error". Then turn Relay off and start the checklist at again at step 5 in the Program Start-Up block on the previous page.

Notes

Internal Balance Installation Checklist

Ver. 1.0, Instructions on Reverse Side *Updated 19 Nov. 2012*

Pre-Installation

- ◯ Sting installed ..... YES
- ◯ String through internal bore ..... YES
- ◯ IB cable attached to string ..... YES
- ◯ IB cable run through sting ..... YES
- ◯ IB cable run into balance room ..... YES

Installation

- ◯ IB into end of sting ..... YES
- ◯ "Anti-rotation" pin gently set IB ..... YES
- ◯ Push on bolts and tighten ..... YES
- ◯ "Anti-rotation" pin fully set ..... YES
- ◯ Remove push on bolts ..... YES
- ◯ Opposing set-screws into place ..... YES

Connection

- ◯ IB SCXI block taped to cradle ..... YES
- ◯ IB cables connected ..... YES

Post-Installation

- ◯ "Cal-body" block ..... INSTALLED
- ◯ "Cal-body" block set with pin ..... YES
- ◯ Roll angle ..... ZERO
- ◯ Pitch angle ..... ZERO
- ◯ "Cal-body" block removed ..... YES
- ◯ Test info set to correct IB ..... YES
- ◯ Visual Basic on "DAQ" ..... OPEN
- ◯ SCXI program ..... OPEN
- ◯ Initial loads check of connections ..... YES
- ◯ IB null offeset ..... YES
- ◯ IB loads reading zero ..... YES

Internal Balance Connections

For the Mark X and Mark XIII internal balances, each channel has four , color-coded, wires that must be connected in the following order:

Signal Input (S+) ..... GREEN
Signal Output (S-) ..... VARIED
Power Input (P+) ..... RED
Power Output (P-) ..... BLACK

There are a total of six internal balance channels that need to be connected. Each channel is connected in the order shown above. However, the channel signal outputs are also color-coded. The individual channels should be connected in the following order:

- ◯ N1 ..... BLUE
- ◯ N2 ..... WHITE
- ◯ S1 ..... GRAY
- ◯ S2 ..... YELLOW
- ◯ RM ..... ORANGE
- ◯ AF ..... PURPLE

Checklist Complete By: Date and Time:

Fig. 93: Version 1.0 of the Internal Balance Installation Checklist.

Checklist Instructions

Complete the checklist:

Verified or Completed Step: ⓥ or ◉

Skipped Step: ⊖

Use the notes block to indicate any problems, maintenance issues, and remark why steps were not completed.

The tunnel operations lead signs the checklist upon completion while noting the date and time.

Procedural Details

Be extremely careful with the IB and the IB cable while running it through the internal bore of the sting. The push bolts are used to get enough torque to push the balance into the end of the sting. Once the "anti-rotation" pin is firmly set, the push bolts should be replaced with set screws.

There are a total of 24 connections on the IB SCXI block. The instructions in the right column show what order to connect the wires.

When zeroing HARS, it might take several attempts to make sure the pitch and roll are zeroed. Beta should be zeroed with the transit once the model is installed.

It is important to make sure that the test information file has the correct internal balance selected. This file will tell the computer which calibration to download for the test.

After starting the SCXI program, look at the forces and moments as a sanity check. All the readings should be small (less than 20 [lbf]). If any of the readings are suspiciously large, the connections between the internal balance cable and the SCXI block must be checked.

Notes

Sting Deflections Checklist

Ver. 1.0, Instructions on Reverse Side *Updated 19 Nov. 2012*

Program Start-Up

- ◯ Visual Studio on "DAQ" ..... OPEN
- ◯ "Single Point" program ..... OPEN
- ◯ Record Data (button) ..... ON

Horizontal Deflection Installation

- ◯ "Cal-body" block on IB ..... YES
- ◯ "Cal-body" block set with pin ..... YES
- ◯ Record and photo pin location ..... YES
- ◯ Deflection stand set up ..... YES
- ◯ Stand attached to floor ..... YES
- ◯ Initial leveling of stand arm ..... DONE
- ◯ Hang trapeze ..... DONE
- ◯ Hang plumb bob ..... DONE
- ◯ Tape ruler to floor ..... DONE
- ◯ Preload appropriately ..... DONE
- ◯ Unload ..... DONE
- ◯ Set up bubble inclinometer ..... DONE

Horizontal Force Deflections

- ◯ Wire level ..... YES
- ◯ Trapeze still ..... YES
- ◯ Zero point recorded ..... YES

Repeat for each weight:

- ◯ Load trapeze ..... DONE
- ◯ Level wire ..... DONE
- ◯ Still trapeze ..... DONE
- ◯ Record data ..... DONE

At end:

- ◯ Return to zero ..... YES

Vertical Deflection Installation

- ◯ Deflection stand removed ..... YES
- ◯ Trapeze switched ..... YES
- ◯ Hang trapeze on center of block ..... YES
- ◯ Preload appropriately ..... DONE
- ◯ Unload ..... DONE
- ◯ Set up bubble inclinometer ..... DONE

Vertical Force Deflections

Repeat for each location:

- ◯ Trapeze at correct location ..... YES
- ◯ Trapeze still ..... YES
- ◯ Zero point recorded ..... YES

Repeat for each weight:

- ◯ Load trapeze ..... DONE
- ◯ Still trapeze ..... DONE
- ◯ Record data ..... DONE

At end:

- ◯ Return to zero ..... YES

Notes

Checklist Complete By: Date and Time:

Fig. 94: Version 1.0 of the Sting Deflections Checklist.

Checklist Instructions

Complete the checklist:

Verified or Completed Step: ⓥ or ◉

Skipped Step: ⊖

Use the notes block to indicate any problems, maintenance issues, and remark why steps were not completed.

The tunnel operations lead signs the checklist upon completion while noting the date and time.

Procedural Details

There are several "Cal-body" blocks to chose from. The one made at the LSWT will allow for a calibration check of all forces and moments.

The appropriate pre-loading weight is balance dependent. Use 30 [lbf] for the Mark X and 60 [lbf] for the Mark XIII. For any other balance, double check with the customer or tunnel operations manager.

For the horizontal force deflections, the angle and position of the sting must be recorded if the blade mount is in use.

Sting Deflection Data Table					
Sting Length		*[in]*			
Reference Length		*[in]*			
Weight	SF Roll	SF Yaw	NF 0	NF 1	NF 2
[lbf]	*[min]*	*[in]*	*[min]*	*[min]*	*[min]*

Tunnel Operations Checklist

Ver. 1.0, Instructions on Reverse Side *Updated 16 Nov. 2012*

Pressure System Calibration

- ◯ Calibration Prompt ..... YES
- ◯ Vacuum Pump ..... ON
- ◯ Tank Valve ..... OPEN
- ◯ Pressure Regulator to 130 $\pm$ 10 [psi] ..... DONE
- ◯ Click Calibrate ..... DONE
- ◯ Check Pressure Scanner Range ..... DONE
- ◯ Completed Calibration Prompt ..... YES
- ◯ Vacuum Pump ..... OFF
- ◯ Tank Valve ..... CLOSE
- ◯ Pressure Regulator ..... CLOSED
- ◯ Click Finish ..... DONE
- ◯ Check Response of Readings ..... DONE

Test Matrix Modification

- ◯ Configuration File ..... OPEN
- ◯ Macros ..... ENABLED
- ◯ Change Field of Interest ..... DONE
- ◯ Click Out of Changed Fields ..... DONE
- ◯ Wall-E ..... DONE
- ◯ Save ..... DONE
- ◯ Check Change on Config.txt ..... DONE

Motor Start-Up

- ◯ Check RPM Setting ..... DONE
- ◯ Test Section Door ..... CLOSED
- ◯ Test Section Door ..... LOCKED
- ◯ Oil Pump ..... ON
- ◯ Start Motor ..... DONE
- ◯ Motor to Set RPM ..... YES
- ◯ Pitch to Q ..... DONE
- ◯ $P_s >$ -8 [psf] ..... YES

Motor Shut-Down

- ◯ Decrease q slowly ..... DONE
- ◯ $P_s <$ +4 [psf] ..... YES
- ◯ Stop Motor ($Q_{act} <$ 30 [psf]) ..... DONE
- ◯ Blade Pitch ($Q_{act} <$ 8 [psf]) ..... NEUTRAL
- ◯ Dynamic Pressure ..... ZERO
- ◯ Oil Pump ($<$ 80 [RPM]) ..... OFF

Notes

Checklist Complete By: Date and Time:

Fig. 95: Version 1.0 of the Tunnel Operations Checklist.

Checklist Instructions

Complete the checklist:

Verified or Completed Step: ⓥ or ◉

Skipped Step: ⊖

Use the notes block to indicate any problems, maintenance issues, and remark why steps were not completed.

The tunnel operations lead signs the checklist upon completion while noting the date and time.

Procedural Details

Hot-wire Checklist

Ver. 1.0, Instructions on Reverse Side *Updated 6 Dec. 2012*

List of Materials

- ◯ Line Conditioner ..... YES
- ◯ Anemometer ($\geq$1CH, 5 [m]) ..... YES
- ◯ Bandpass Filter (1 [Hz] to 15 [Hz]) ..... YES
- ◯ Osilloscope ..... YES
- ◯ DANTEC Single Hotwire ($\leq$5 [μm]) ..... YES
- ◯ Single Hot-wire Shorting Probe ..... YES
- ◯ 1 RG-58 BNC Cable ($\sim$5 [m]) ..... YES
- ◯ 2 BNC Cables ($\geq$15 [m]) ..... YES
- ◯ 2 BNC Cables ($\leq$1 [m]) ..... YES
- ◯ 1 BNC T-Connector ..... YES

Hot-wire System Set-Up

- ◯ BNC Cable Connected ..... DONE
- ◯ Hot-wire to Anemometer Input CH1 ..... DONE
- ◯ Anemometer CH1 Output to DAQ CH1 ... DONE
- ◯ Anemometer CH1 Output to Filter ..... DONE
- ◯ Anemometer Output to Oscilloscope ..... DONE
- ◯ Filter Output to DAQ CH2 ..... DONE
- ◯ Power Cables into Line Conditioner ..... DONE

Hot-wire System Start-Up

- ◯ All Equipment ..... OFF
- ◯ CH Mode Selectors ..... N
- ◯ Line Conditioner ..... ON
- ◯ Anemometer ..... ON
- ◯ Signal Filter ..... ON
- ◯ Oscilloscope ..... ON
- ◯ Anemometer Test Mode ..... N/ADJ
- ◯ Thumbwheels ..... ZERO
- ◯ DC Offset Trimpot ..... ZERO

Hot-wire Set-Up

Repeat for each channel:

- ◯ Anemometer CH ..... SELECT
- ◯ CH Mode Selector ..... ADJUST
- ◯ Decade Range X10
- ◯ Shorting Probe ..... INSTALLED
- ◯ Balance with Null Trimpot ..... 0.00 [V]
- ◯ Shorting Probe ..... UNISTALLED
- ◯ Hot-wire ..... INSTALLED
- ◯ Balance with Thumbwheels ..... 0.00 [V]
- ◯ Overheat X1.8 ..... DONE
- ◯ CH Mode Selector ..... N
- ◯ Tuning Coil ..... FLUSH
- ◯ Damping Trimpot ..... -9.00 [V]

Hot-wire Tuning

Repeat for each channel:

- ◯ Oscilloscope AC ..... 1 [V]
- ◯ Oscilloscope Time Base ..... 5 [μs]
- ◯ Oscilloscope Averages 16
- ◯ Oscilloscope Screen ..... CENTERED
- ◯ Anemometer CH ..... SELECT
- ◯ CH Mode Selector ..... OPERATE
- ◯ Anemometer Test Mode ..... PULSE
- ◯ Frequency Response ..... DONE

Hot-wire Calibration

- ◯ Anemometer CH ..... SELECT
- ◯ Anemometer Test Mode ..... REFERENCE
- ◯ Adjust Gain 7.00
- ◯ Anemometer Test Mode ..... OPERATE
- ◯ Test Section ..... $\sim$10 [mph]
- ◯ DC Offset ..... +9.5 [V]
- ◯ Calibration Run ..... COMPLETE

Checklist Complete By: Date and Time:

Fig. 96: Version 1.0 of the Hot-wire Checklist.

Checklist Instructions

Complete the checklist:

Verified or Completed Step: ⓥ or ◉

Skipped Step: ⊖

Use the notes block to indicate any problems, maintenance issues, and remark why steps were not completed.

The tunnel operations lead signs the checklist upon completion while noting the date and time.

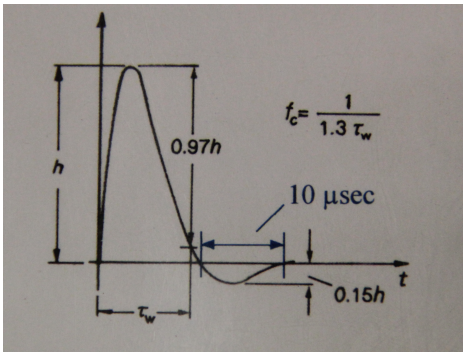

Figure 1: Result of hot-wire tuning.

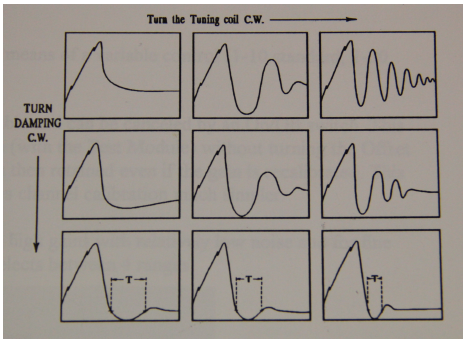

Figure 2: Effect of the tuning coil and damping trimpot.

Procedural Details

Note that the BNC cable from the hot-wire to the anemometer need to be an RG-58 type cable with a length of 5 $\pm$ 0.25 [m].

See the anemometer manual for more system start-up instructions and warnings.

Adjust the damping trimpot and tuning coil to make the anemometer output on the oscilloscope mirror the signal image in Figure 1. How the damping trimpot and tuning coil adjust the signal is shown in Figure 2.

Set the gain to 7.00 and the DC offset to $+9.5$ [V] while the tunnel is in operation at low RPM with a test section velocity of 10 $\pm$ 2 [mph]. The hot-wire voltage will go out of range when the tunnel is turned off, but will stay within range for all possible velocities above 10 [mph].

Set the DC signal range on DAQ to $\pm$ 10 [V]. For turbulence intensity measurements, sample the data at 16,384 [Hz] for 2 [s] intervals.

Calibrate the hot-wire at lower and higher speeds than the expected operating range.

Notes

APPENDIX F

DATA ANALYSIS AND UNCERTAINY

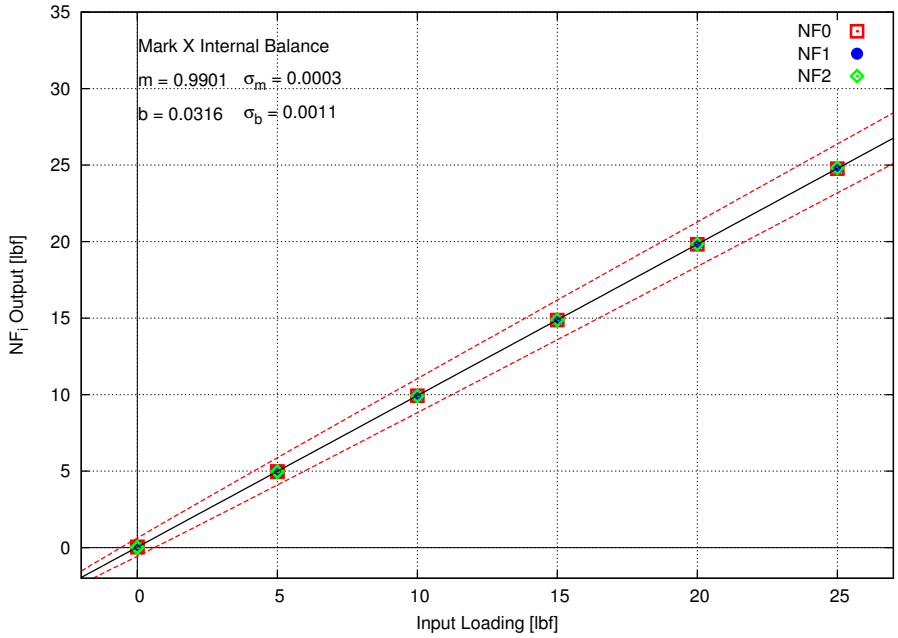

Fig. 97: Normal force calibration data for the Mark X internal balance.

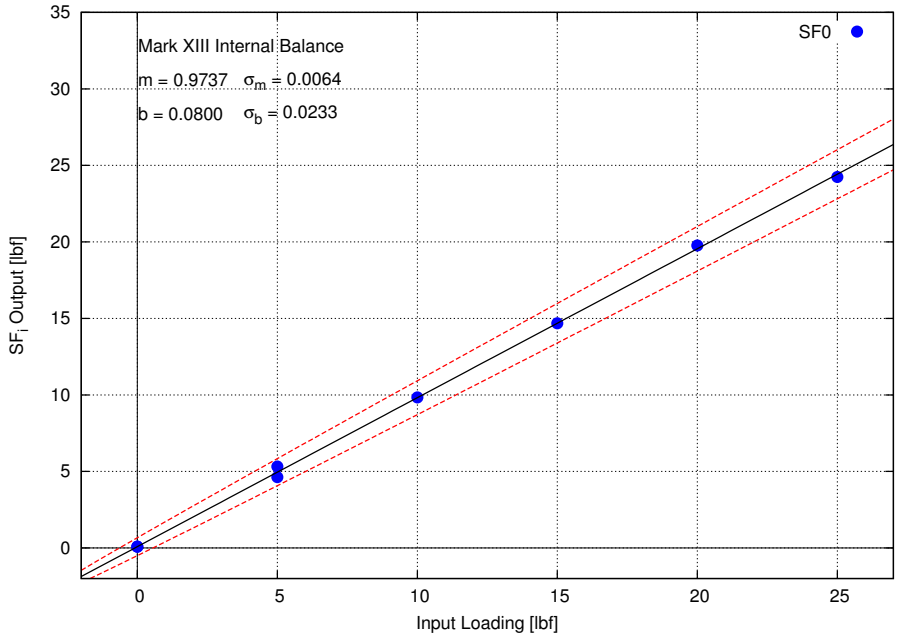

Fig. 98: Side force calibration data for the Mark X internal balance.

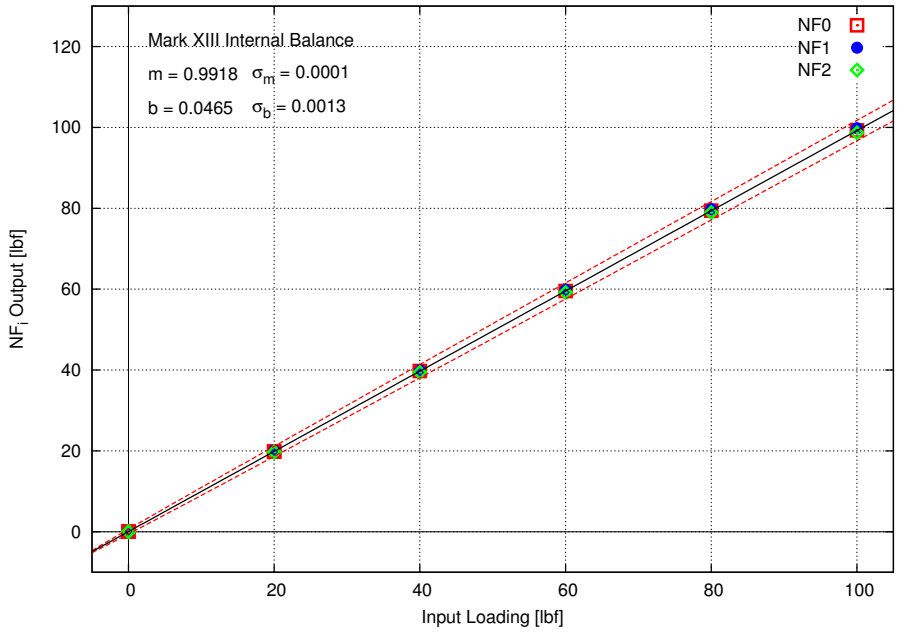

Fig. 99: Normal force calibration data for the Mark XIII internal balance.

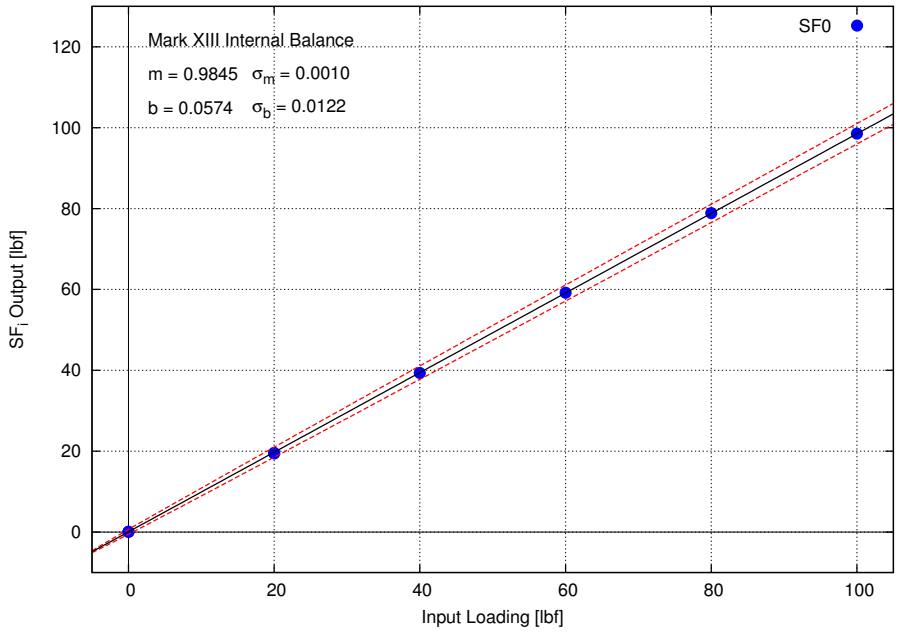

Fig. 100: Side force calibration data for the Mark XIII internal balance.

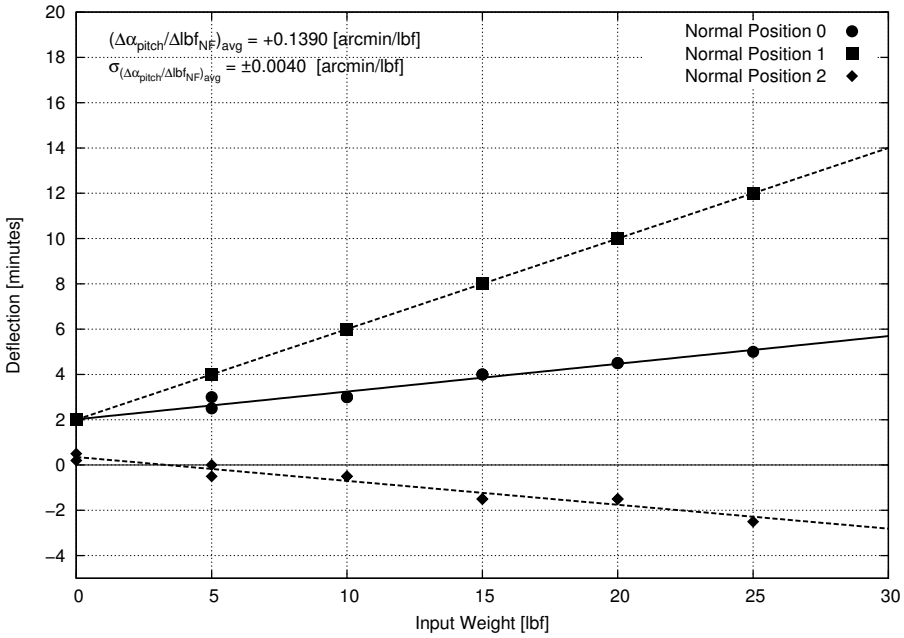

Fig. 101: Sting deflection data fit to calculate the pitch angle correction.

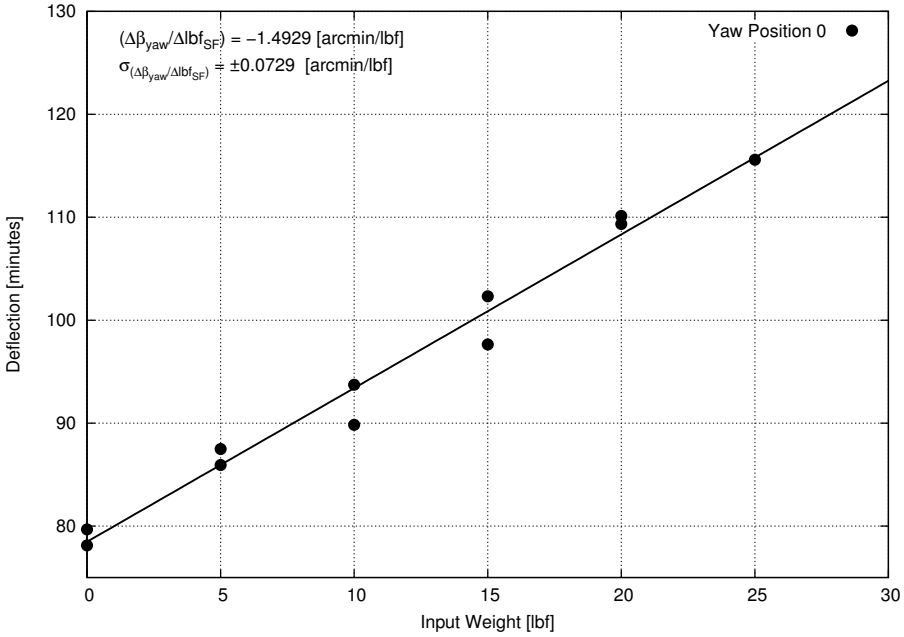

Fig. 102: Sting deflection data fit to calculate the yaw angle correction.

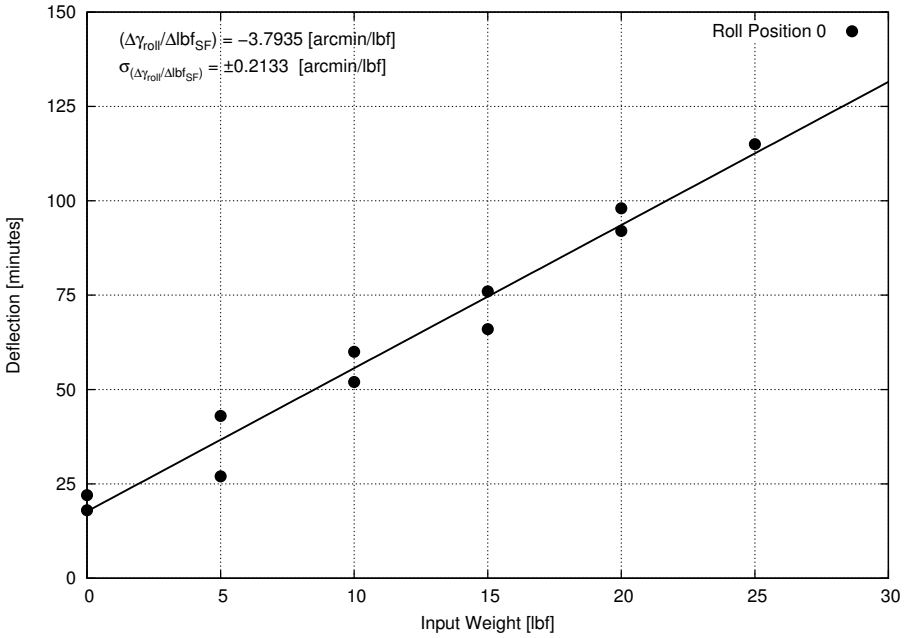

Fig. 103: Sting deflection data fit to calculate the roll angle correction.

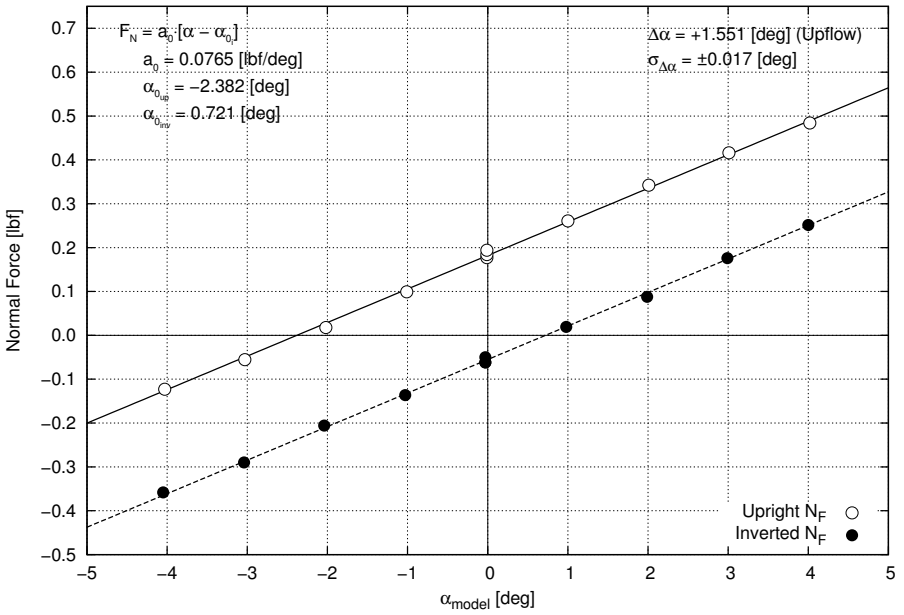

Fig. 104: Results of the flow angularity tests to correct the model angle of attack.

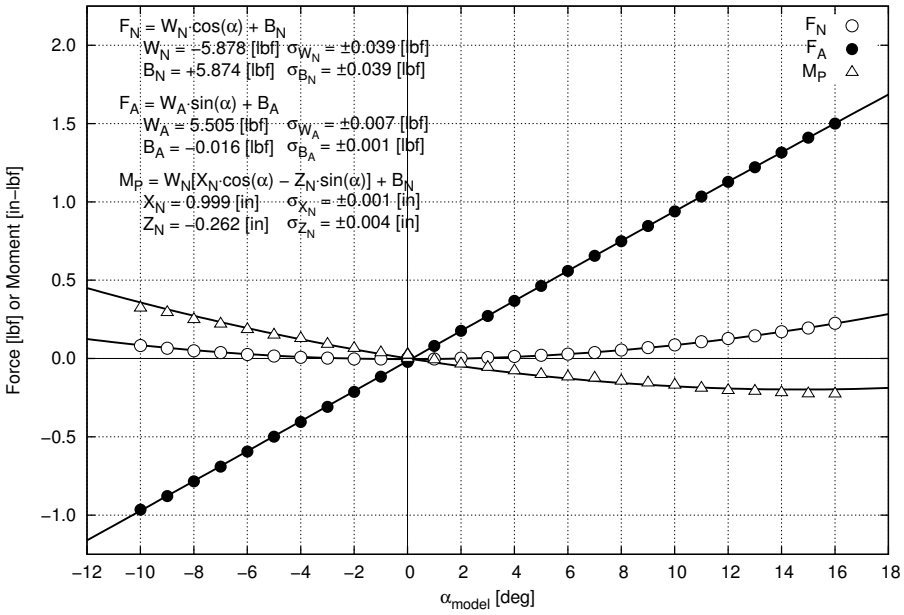

Fig. 105: Fit curves for the force and moment static tare data.

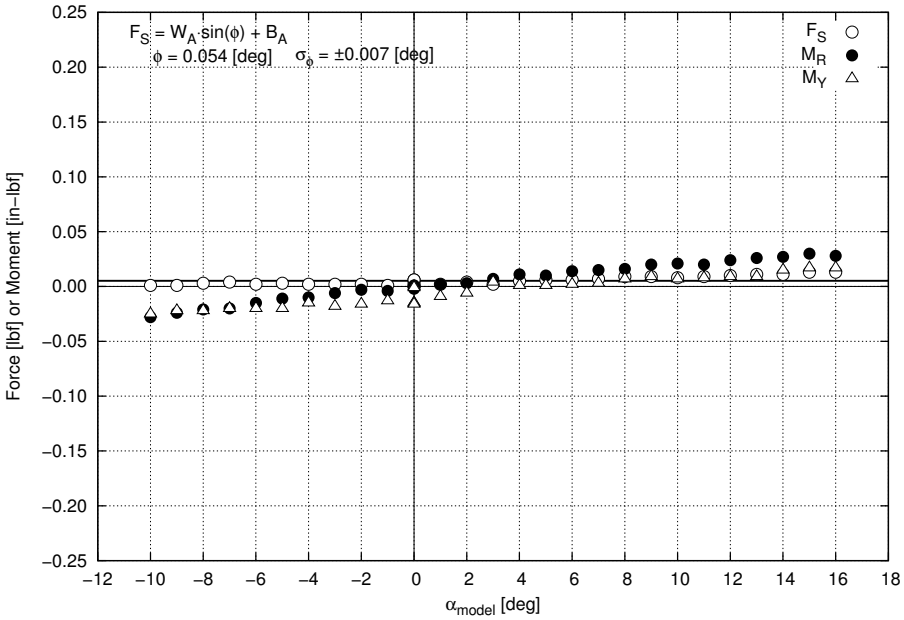

Fig. 106: Static tare force and moment data not being fit.

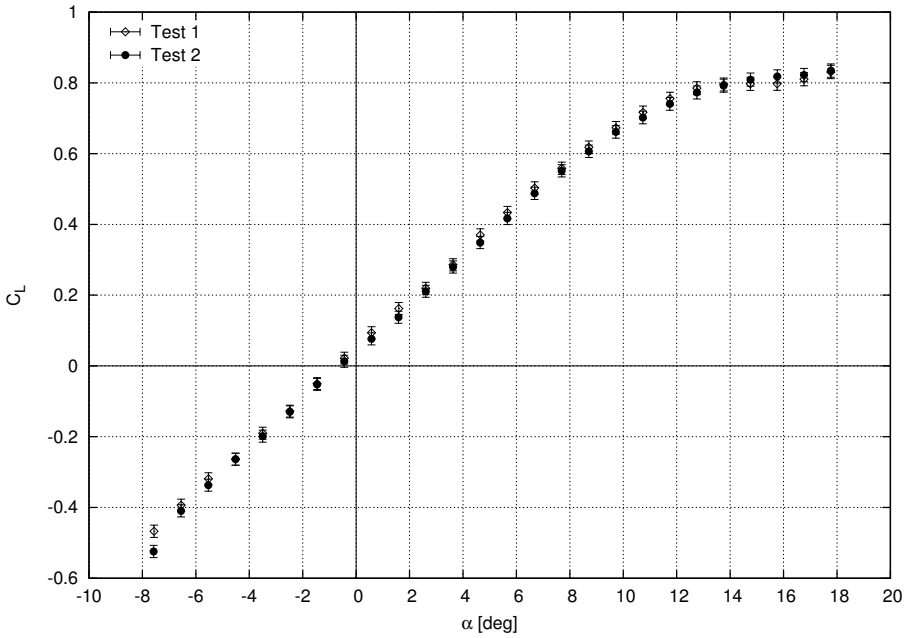

Fig. 107: Lift coefficient data from the repeatability tests.

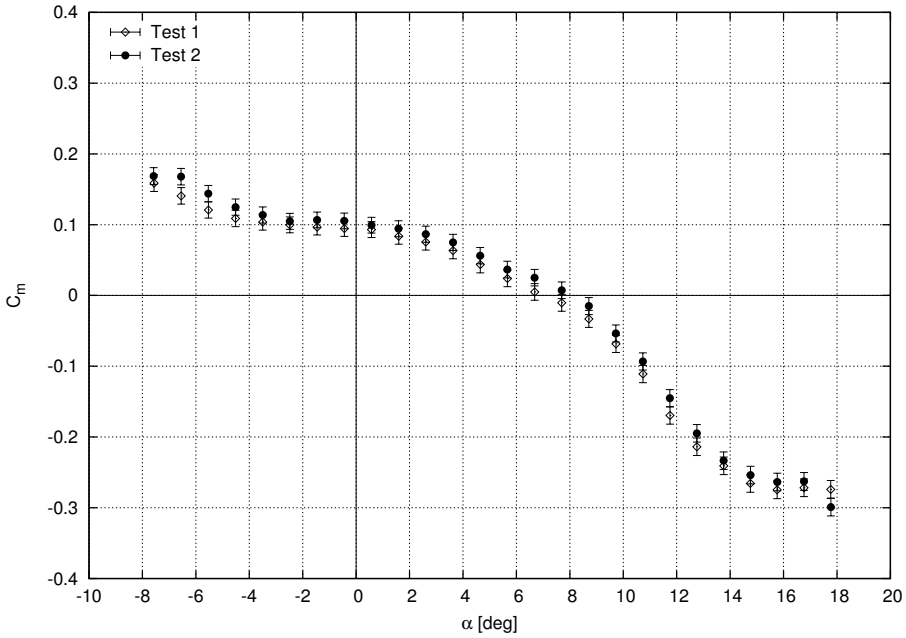

Fig. 108: Pitching moment coefficient data from the repeatability tests.

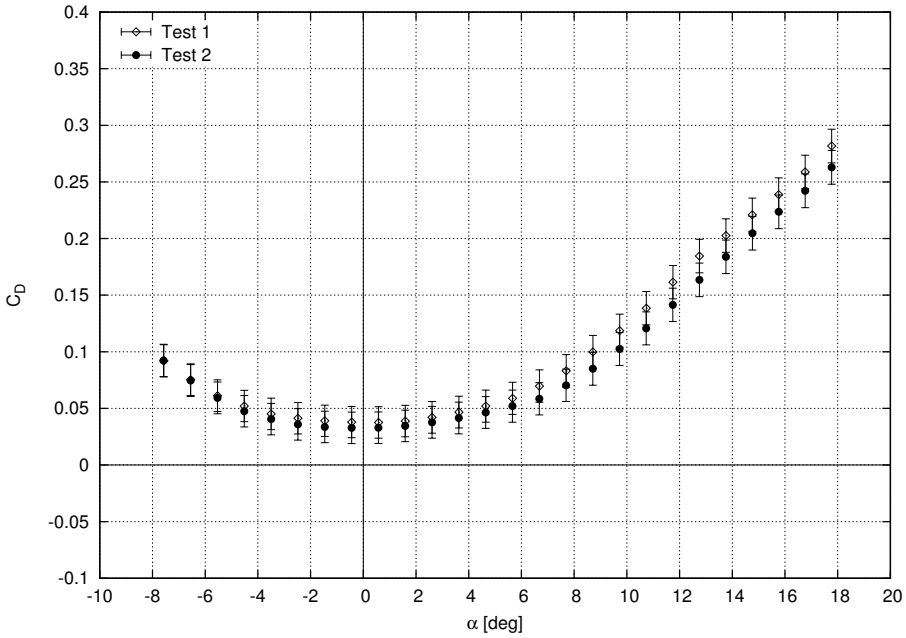

Fig. 109: Drag coefficient data from the repeatability tests.

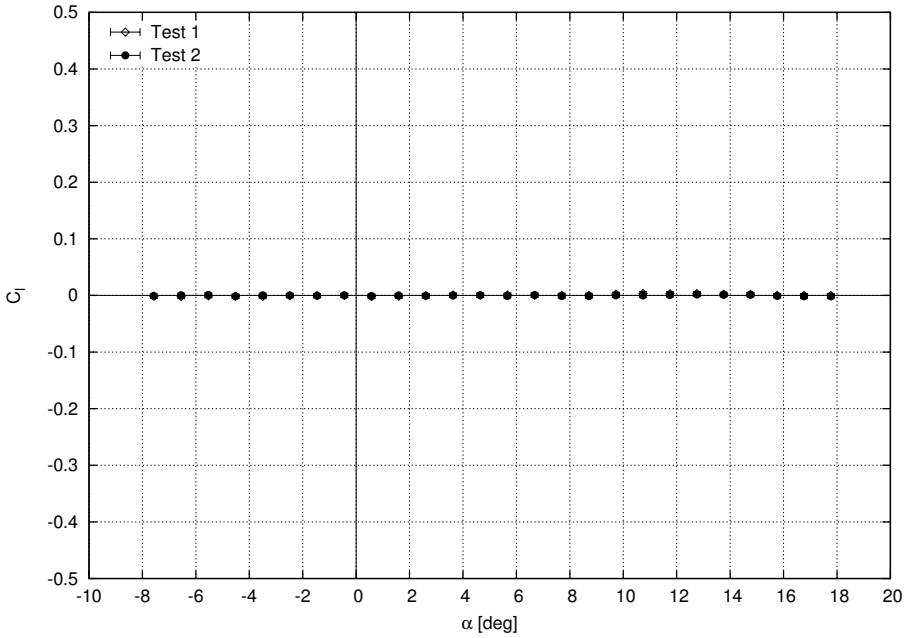

Fig. 110: Rolling moment coefficient data from the repeatability tests.

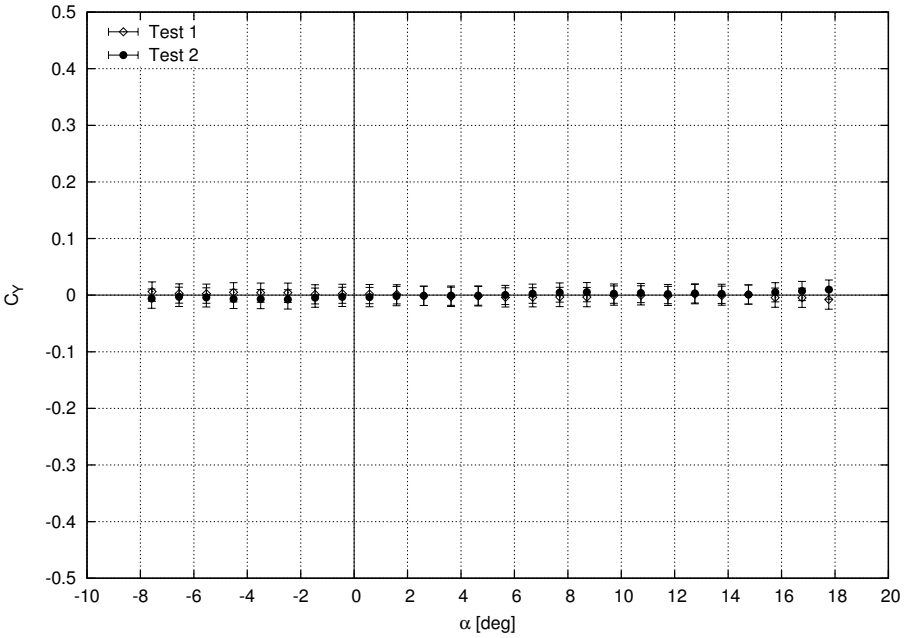

Fig. 111: Side force coefficient data from the repeatability tests.

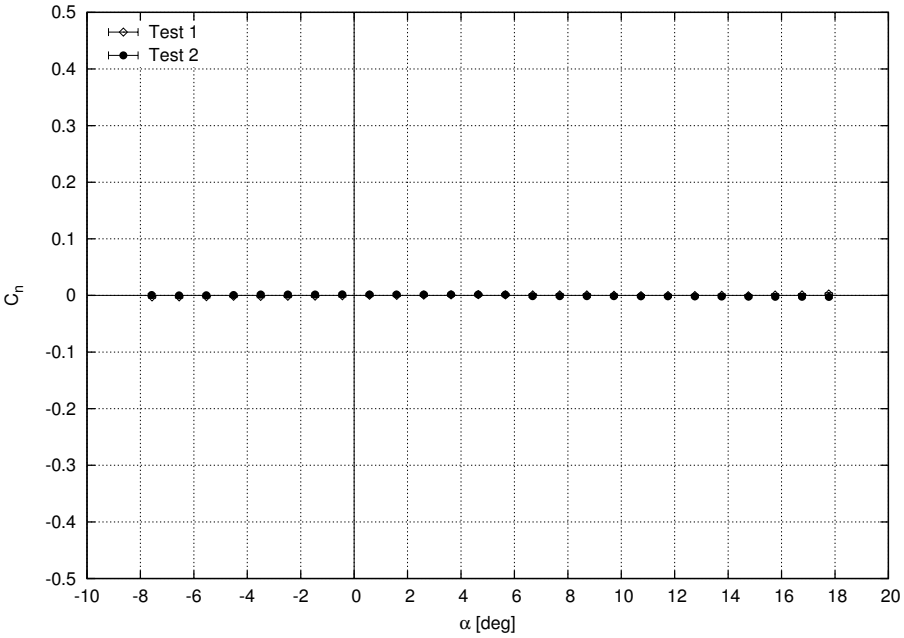

Fig. 112: Yawing moment coefficient data from the repeatability tests.